The silicon-vacancy centre in diamond for quantum information processing

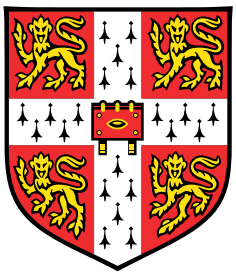

Benjamin Jean-Pierre Pingault

Supervisor: Prof. Mete Atatüre

Department of Physics
University of Cambridge

This dissertation is submitted for the degree of
Doctor of Philosophy

Pembroke College November 2017

A mes parents, à ma famille, à mes professeurs.

Declaration

This dissertation is the result of my own work and includes nothing which is the outcome of work done in collaboration with others, except where specified in the text. It is not substantially the same as any that I have submitted, or, is being concurrently submitted for a degree or diploma or other qualification at the University of Cambridge or any other University or similar institution except as specified in the text. I further state that no substantial part of my dissertation has already been submitted, or, is being concurrently submitted for any such degree, diploma or other qualification at the University of Cambridge or any other University or similar institution except as specified in the text. This dissertation does not exceed the prescribed word limit of 60,000 words.

Benjamin Jean-Pierre Pingault
November 2017

Acknowledgements

First of all, I would like to thank a lot my supervisor Prof. Mete Atatüre for giving me the opportunity to carry on this exciting research project. Scientific discussions with him have always been very insightful and stimulating. Thanks also for fostering a pleasant environment within the group, element which often helps in experiment-wise tough times.

I also want to thank Ms. Pam Smith, administrator of our group. Her efficiency has always been beyond expectations and her standards of professionalism have been an example for us all. Thank you for going out of your way to help us each time we entered your office in panic.

I am also particularly grateful to Tina Müller for having introduced me to the topic and experiment. Thank you for your enthusiasm and for having patiently answered my so numerous questions during the first months of my Ph.D.

I want to thank Christian Hepp who started as our collaborator and ended up joining our group for his postdoc. Your invariable good mood has been of great help during intense measurement periods.

Thank you to Camille Stavrakas and Mustafa Gündoğan for the nice moments and discussions in tough experimental times. I will miss our medidative walks to the vending machines when we really needed a break.

There is also a big thank you to all the current and past group members: Yuri Alaverdyan, Matteo Barbone, Joshua Barnes, Jan Beitner, Gabriel Ethier-Majcher, Dorian Gangloff, Paul Geller, Jack Hansom, Jeffrey Holzgrafe, Lukas Huthmacher, Dhiren Kara, Lina Klintberg, Helena Knowles, Claire Le Gall, Clemens Matthiesen, Carmen Palacios-Berraquero, Alejandro Rodrigues-Pardo Montblanch, Carsten Schulte, Megan Stanley Lucio Stefan, Robert Stockill and Stephen Topliss. Not only are they always prompt in helping on any aspect, they also maintain a very friendly and relaxed environment, which is of great support in the daily routine.

Thank you to Jonas N. Becker for having kept pushing in the intense months of measurement of CPT.

Thank you to Srujan Meesala and Young Ik Sohn for the great times improving SiV coherence times. Although the experiments were demanding, you made them fun, Young Ik, with your inimitable sense of humour and Srujan, with your cats and imitations of Marko.

Je souhaite enfin remercier mes parents et ma famille pour m'avoir soutenu, pour m'avoir permis de faire de longues études et pour avoir été là dans les moments difficiles.

Right, it is now 4:50 a.m., the sun is rising, and I really need some rest.

Abstract

Atomic defects in solids offer access to atom-like quantum properties without complex trapping methods while displaying a rich physics due to interactions with their solid-state environment. Such properties have made them an advantageous building block for quantum information processing, in particular to construct a quantum network, where information would be encoded in spins and transferred between nodes via photons. Among defects in solids, the negatively charged silicon-vacancy centre in diamond (SiV^-) has attracted attention for its very promising optical properties for such a network.

In this thesis, we investigate the spin properties of the silicon-vacancy centre as a potential spin-photon interface. First, we use resonant excitation of an SiV^- centre in an external magnetic field to selectively address different electronic states and analyse the resulting fluorescence. We find evidence of selection rules in the optical transitions revealing that the centre possesses an electronic spin $S = 1/2$. Making use of the dependence of such selection rules on the applied magnetic field orientation, we resonantly drive two optical transitions forming a Λ-scheme. In the double resonance condition, we achieve coherent population trapping, whereby the SiV^- is pumped into a dark state corresponding to a superposition of the two addressed ground states of opposite spin. This technique allows us to evaluate the coherence time of the dark state and hence of the spin, while demonstrating the possibility of all-optical control of the spin when a Λ-scheme is available. We then use resonant optical pulses to initialise and read out the spin state of a single SiV^-. By tuning a microwave pulse into resonance between two ground states of opposite spin, we demonstrate optically detected magnetic resonance. Subsequently, by varying the duration of a resonant microwave pulse, we achieve coherent control of a single SiV^- electronic spin. Through Ramsey interferometry, we measure a spin dephasing time of 115 ± 9 ns. We then investigate interactions of the SiV^- with its environment. We analyse the hyperfine interaction of the SiV^- spin with the nuclear spin of ^{29}Si, with a view to taking advantage of the long-lived nuclear spin in the future. We show that single-phonon-

mediated excitations between electronic states of the SiV^- are the dominant spin dephasing and population decay mechanism and evaluate how external strain alters optical selection rules and can be used to improve the coherence time of the spin.

Contents

List of Figures

Introduction: Quantum information processing and impurities in solids

Computers have revolutionised our world by enabling us to process data and improve communication abilities at an unprecedented scale. Yet, it is predicted that harnessing quantum mechanics for processing information could drastically expand today's abilities and thus unlock key computational problems such as the simulation of quantum systems, complex chemical reactions or protein misfolding involved in many diseases such as Alzheimer's and Parkinson's diseases [1]. This new vision of computing, named quantum information processing, relies on quantum versions of computer bits, called qubits, to process information. Such a qubit consists of a quantum system with two isolated states tagged 0 and 1. The improvement arises from the property of quantum systems to be in a superposition of states, property which can be extended to several qubits in a collective superposition of states resulting in those qubits being entangled. Such capacities are at the basis of theoretical proposals of quantum algorithms expected to provide an exponential speed-up in the resolution of currently complex computing tasks. The most famous of such proposals is Shor's algorithm formulated in 1994 for integer factorisation into prime numbers [2], the first experimental implementation of which has been demonstrated in 2001 using nuclear magnetic resonance on molecules [3]. The architecture of such a quantum computer is subject to intense debate. All-optical quantum computing appears promising as photons can carry information over long distances with minimum loss and can be manipulated on-chip at room temperature with well-established photonic structures [4–8]. It might however be too costly in terms of resources compared to other methods [9]. A popular approach is to combine the strengths of different systems in a hybrid architecture. In 2008, Kimble proposed the concept of a quantum network in which information is processed in nodes by stationary

qubits and transferred between nodes by flying qubits, most likely photons. However, the choice of a quantum system to be used as stationary qubits is not straightforward [10]. To guide this choice, DiVincenzo has proposed a list of criteria which include the necessity of scalability of well-defined qubits, the capacity to initialise and read out their state individually, a universal set of quantum computation gates and qubit coherence times long enough to perform a meaningful number of such gates [11].

To date, there is no consensus on which quantum system should be used as a qubit and several systems are developed in parallel. They all exhibit advantages and weaknesses [10]. Among them, trapped atoms [12–19] behave as ideal quantum systems with long coherence times but can be difficult to scale up due to the complex experimental setups they require. Superconducting qubits [20–24] and electrically defined quantum dots [25, 26] have the advantage of scalability but are difficult to interface with optical photons [27] and display more modest coherence properties, although progress has been steady over the past few years [24]. A particular attention has been drawn to quantum spin defects in solid-state matrices, such as donor impurities in silicon [28–31] and self-assembled quantum dots [32–39]. While the former hold the record for coherence time [40], they are challenging to interface with light [41], and the latter, although exhibitting excellent optical properties, suffer from short spin dephasing times [42–44]. Indeed, even though such systems behave effectively as single atoms, they interact with the solid-state matrix, which can induce decoherence through various noise sources such as baths of electronic or nuclear spins. There is thus a strong incentive to look for spin-free materials to ensure that spin impurities retain suitable coherence properties. Among such materials, silicon carbide [45–47] and diamond [48–50] have attracted the most attention owing to the variety of optically active defects they host. While silicon carbide offers the advantage of industrial grade synthesis and processing capabilities [45], diamond stands out for its unique physical properties, including its high thermal conductivity [51], wide bandgap accommodating many possible impurity levels from the ultraviolet to the far-infrared [48], its relatively high refractive index [48], important for photonic structures [52–54], its biocompatibility [55–57] and the possibility to use carbon chemistry to functionalise its surface [58, 59]. The most widely studied defect in diamond to date is the negatively charged nitrogen-vacancy (NV^-) centre, consisting of a substitutional nitrogen atom and a neighbouring carbon vacancy [48]. The reason for this popularity is the impressive range of applications which have been achieved using this defect [60–63]. Most of them rely on its optically accessible electronic spin $S = 1$ which can be operated at room temperature. For quantum

information processing, several key steps have already been demonstrated, among which the demonstration of entanglement between the NV^- spin and the polarisation of a single photon [64], later used to entangle two distant NV^- spins using their photons as vectors of the entanglement [65, 66]. The NV^- centre also offers optical access to long-lived neighbouring nuclear spins, which can be entangled with the NV^- spin [67] or other nuclear spins [68], coherently controlled [69–71, 67, 72], and be used as quantum memories [73] and ancilla qubits for computation protocols [74]. The applications of the NV^- centre even extend beyond quantum information processing into quantum sensing at the nanometric scale, for electric [75] and magnetic field sensing [76–79], and thermometry [80–82], including in biological systems [83, 84], where it can also be used for bio-labelling [55–57]. However, the optical properties of the NV^- centre are not ideal for quantum information processing as only a fraction of the emitted photons can be used as flying qubits in the absence of optical cavities. While progress has recently been reported [85], an alternative approach consists in searching for defects already offering the desired optical properties [50]. This approach has brought us to study the silicon-vacancy centre in diamond, which shows great promise owing to its remarkable optical properties but remains elusive as to its possessing a spin degree of freedom.

In this thesis, we investigate the potential of the silicon-vacancy centre in diamond for quantum information processing. In Chapter 1, we review the current knowledge about this system, focusing in particular on its structure and optical properties, the latter being characterised by a desirable low coupling to phonons. In Chapter 2, we evidence optical signatures of an electronic spin $S = 1/2$, hence paving the way for the silicon-vacancy centre to be used as a qubit. In Chapter 3, we demonstrate the feasibility of optical control of the spin through achieving coherent population trapping, and extract a first evaluation of the spin coherence time. In Chapter 4, we demonstrate optically detected magnetic resonance and coherent control of the silicon-vacancy centre spin by microwave pulses. We use this control to perform Ramsey interferometry and obtain a direct measurement of the spin coherence time. Finally, in Chapter 5, we explore the interactions of the silicon-vacancy centre with its environment. In particular, we measure the hyperfine coupling between the electronic spin and the nuclear spin of the constituent ^{29}Si. We also show that the interaction with lattice phonons is the dominant source of decoherence of the electronic spin. Finally, we investigate the influence of crystalline strain onto the silicon-vacancy centre energy levels and spin properties and discuss how strain could be used as a resource for quantum information applications.

Chapter 1

The silicon-vacancy centre in diamond

Diamond is host to many optically active defects which have been characterised to various degrees and display a wide range of optical and electronic properties [48]. Although many of them have been known since the 1960s, it is the success of the nitrogen-vacancy (NV^-) centre for various applications in quantum computing and sensing over the past two decades that has drawn attention to the potential of impurities in diamond. The investigation of other defects has mainly been motivated by the interest in finding emitters with optical properties surpassing those of the NV^- centre, for which only a fraction of the emitted photons can be used as flying qubits in the absence of photonic structures.

In this chapter, we introduce the silicon-vacancy centre in diamond. We review its composition and structure as well as its optical and spin properties, which are those of particular interest from the point of view of quantum information processing. The main motivation for pursuing the investigation of this colour centre relies on its desirable fluorescence properties, where most of the emission does not involve the incoherent generation of phonons. Most of the emitted photons could thus be suitable to encode information and transfer it between processing nodes in a quantum network [86].

1.1 Structure and creation

The silicon-vacancy centre (SiV) is an optically active defect which consists of a silicon atom and a vacancy, replacing two neighbouring carbon atoms in a diamond matrix (see Fig. 1.1). The presence of silicon has been determined through growth and ion

implantation studies where fluorescence characteristic of SiV centres is only found when silicon has been incorporated into the diamond [87, 88]. This has been confirmed by showing that a change in the isotopic ratios of silicon incorporated into the diamond structure shifts the wavelength of its emission [89–91]. The association of a contiguous vacancy is deduced from the increase of the emission intensity of the centre after annealing, this increase being concomitant with a decrease in the intensity of the GR1 band, corresponding to neutral vacancies [92, 93].

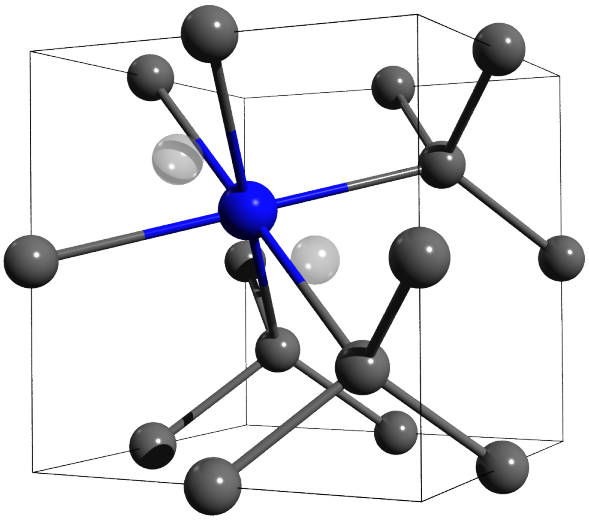

Figure 1.1 Representation of the structure of a silicon-vacancy centre in a diamond lattice (carbon atoms in dark grey, silicon atom in blue) [94]. The silicon atom is located in the middle of the two lattice sites (in light grey) along the $< 111 >$ crystallographic directions.

The ensemble composed of the silicon atom and the vacancy is theoreticlly predicted to lie along the $< 111 >$ directions of the diamond lattice [95, 96], as shown in Fig.1.1. This orientation has been confirmed experimentally by electron paramagnetic resonance (EPR) [97]. This implies that four equivalent orientations of the axis of the colour centre are possible along the crystallographic directions [111], $[1\bar{1}\bar{1}]$, $[\bar{1}\bar{1}1]$ and $[\bar{1}1\bar{1}]$. We mention that some fluorescence polarisation measurements have suggested a $< 110 >$ orientation, although the emitters investigated were likely strained, which can affect polarisation [94].

Simulations based on density functional theory (DFT) [95, 96] and restricted open-shell Hartree-Fock (ROHF) calculations [98] reach the conclusion that the silicon atom sitting at a lattice position next to a vacancy is unstable. Instead, the silicon atom relaxes towards the centre of the two lattice sites and the vacancy is split on each side

[95, 96, 99]. The silicon atom is thought to lie exactly in the middle of the vacancy sites, thus giving the SiV centre an inversion symmetry [95, 96, 99], although other theoretical predictions argue in favour of the Si atom oscillating along the $< 111 >$ axis in a double-well potential [98]. This double semi-vacancy configuration is also suggested for other defects in diamond involving a vacancy and a large atom, such as nickel, cobalt and germanium [100–104].

We focus our study on the negative charge state of the SiV, where an extra electron is captured by the colour centre. It is thus labelled SiV^-. The attribution of this charge state to the fluorescence described in the next section is based on theoretical predictions [95] as well as photoionisation experiments [105].

The diamond samples used as host of SiV centres are mainly synthetic diamonds manufactured by high-pressure-high-temperature (HPHT) processes or chemical vapour deposition (CVD). HPHT diamonds are formed by compressing carbon in an anvil cell to pressures reaching the GPa regime and heated to more than 1400 °C, thus mimicking the growth conditions of natural diamonds in the earth mantle [106]. Small diamonds are used to seed the growth and certain metals, such as iron or cobalt, act as catalysts. Such diamonds usually contain large quantities of impurities, in particular nitrogen from the air, but have the advantage of displaying relatively low crystalline strain. CVD diamonds are grown in a plasma chamber containing a mixture of hydrocarbon gas, often methane, and hydrogen [107]. The gases are ionised to form radicals which deposit and form sp^2 and sp^3-bound carbon on a heated substrate, and grow diamond layer by layer in tightly regulated pressure, temperature and gas mixture conditions.

The creation of the SiV centre is relatively easy and can be performed by ion implantation or by incorporation of silicon during chemical vapour deposition (CVD) growth. In the former, a diamond sample is exposed to a beam of Si^+ ions accelerated by strong electric fields, and directed and focused by magnetic lenses. The ions acquire a kinetic energy from a few tens to hundreds of keV, enough to allow them to penetrate into the diamond [108]. This kinetic energy is the dominant factor in determining the implatation depth of the silicon ions which can be evaluated through a stopping-range-of-ions-in-matter (SRIM) algorithm [109]. The second creation method relies on incorporation of silicon atoms during CVD growth, with silicon being provided by a silicon substrate, a neighbouring piece of silicon carbide or even by simple contamination of the growth chamber [110–112]. After silicon atoms have been implanted or incorporated during growth, an irradiation with MeV electrons or carbon ions can be used to increase the number of vacancies. Annealing at around 900°C for several hours

then allows vacancies to become mobile, thus facilitating the capture of vacancies by silicon atoms and causing partial healing of implantation damage [93, 97]. Finally, the charge state in which we are interested for its optical properties corresponds to an extra electron being trapped by the centre, which is consistent with density functional theory studies of the fluorescence [113].

1.2 Optical properties

The diamond band structure is characterised by a large indirect band gap of 5.5 eV and a direct gap energy of 7.3 eV at the Γ point at the centre of the Brillouin zone [114]. This makes diamond transparent from the utlraviolet into the far-infrared [48]. As a consequence, optically active defects with energy levels lying in this gap give diamond its colour, when such defects are in large concentrations. They are thus often referred to as colour centres [48].

The SiV^- centre is until now the brightest reported colour centre in diamond, with up to 6.2×10^6 counts per second [115] for an SiV^- in a nanodiamond. However, for bulk samples, values lower by one order of magnitude under non-resonant excitation (see Section 3.2) and by up to three orders of magnitude under resonant excitation (see Section 3.3) are more typical. The latter is partially due to an unstability of the charge state of the SiV [116], as is the case for the NV centre [117].

A first element influencing the brightness of the centre is the lifetime of the excited state. A relatively short lifetime of 1-4 ns has been determined by intensity decay [89] and autocorrelation measurements [94, 115] at cryogenic temperatures. Those values are in good agreement with a theoretical value of 3 ns obtained by spin-polarised local density functional cluster theory [95] and can be compared to the 13 ns lifetime of NV^- centres [118].

The fluorescence spectrum of colour centres is typically composed of a sharp zero-phonon line (ZPL) corresponding to direct transitions between electronic states, and broader phonon sidebands, where the photon emission is accompanied by emission or absorption of phonons, resulting in fluorescence being shifted to lower or higher wavelengths, respectively [48]. The SiV^- centre fluorescence is characterised by a zero-phonon line at 737 nm (1.68 eV) and phonon sidebands ranging approximately from 750 to 800 nm [94, 90, 95]. This ZPL has the particularity of being remarkably narrow, down to 0.7 nm at room temperature [94].

In addition, the SiV^- centre fluorescence is found to exhibit a low electron-phonon coupling, resulting in little emission occurring into the phonon sidebands. Such a coupling originates from the fact that when the centre is excited from the ground to the excited state, the electron wavefunction and thus the electronic charge distribution changes, leading to the neighbouring nuclei to shift in position. This phenomenon can be visualised by considering the interaction between two electronic levels and a vibrational mode approximated as a harmonic oscillator. Following Ref. [119], in the ground state, the vibronic harmonic potential is of the form:

$$V_g = \frac{1}{2} m\omega^2 Q^2 \tag{1.1}$$

where ω is the mode frequency, m the mass of the mode and Q the displacement from equilibrium (generalised coordinate frame). In the excited state, it is:

$$V_e = V_0 + \frac{1}{2} m\omega^2 Q^2 + aQ + bQ^2 \tag{1.2}$$

$$= V_0 + \left(\frac{1}{2} m\omega^2 + b\right)\left(Q + \frac{a}{m\omega^2 + 2b}\right)^2 - \frac{a^2}{2m\omega^2 + 4b} \tag{1.3}$$

where V_0 is the energy of the purely electronic transition, aQ is the linear phonon coupling corresponding to the new equilibrium position for the nuclei and bQ^2 is the quadratic phonon coupling, small in diamond [119], reflecting the change in the harmonic potential. The new equilibrium point is $Q_0 = -a/(m\omega^2 + 2b)$ and the new mode frequency is $\omega' = \sqrt{\omega^2 + 2b/m}$. We represent those potentials in Fig. 1.2. A non-resonant excitation of the system brings it from the ground state parabola to the excited state one, as depicted by an orange arrow. Since, according to the Franck-Condon principle, optical transitions are fast compared to the vibrations of nuclei, they occur vertically, without displacement ($\Delta Q = 0$). The system thus reaches a vibrational excited state in the harmonic potential, and can then relax to a lower vibrational state corresponding to a number n' of phonons (dashed grey arrow). The subsequent emission of a photon occurs vertically towards a vibrational state of the ground state with phonon number n (dark red arrow), the transition propability depending on the wavefunction overlap between initial and final states. The number of phonons involved in the transition corresponds to the difference between the phonon number in the initial state n' and that in the final state n. The optical emission is thus shifted in frequency when this number is different from zero, causing the presence of phonon sidebands in the fluorescence spectrum. When the difference in phonon number is zero, the emission

corresponds to the zero-phonon line. In summary, the larger the difference in charge distribution between ground and excited states, the stronger the phonon sidebands.

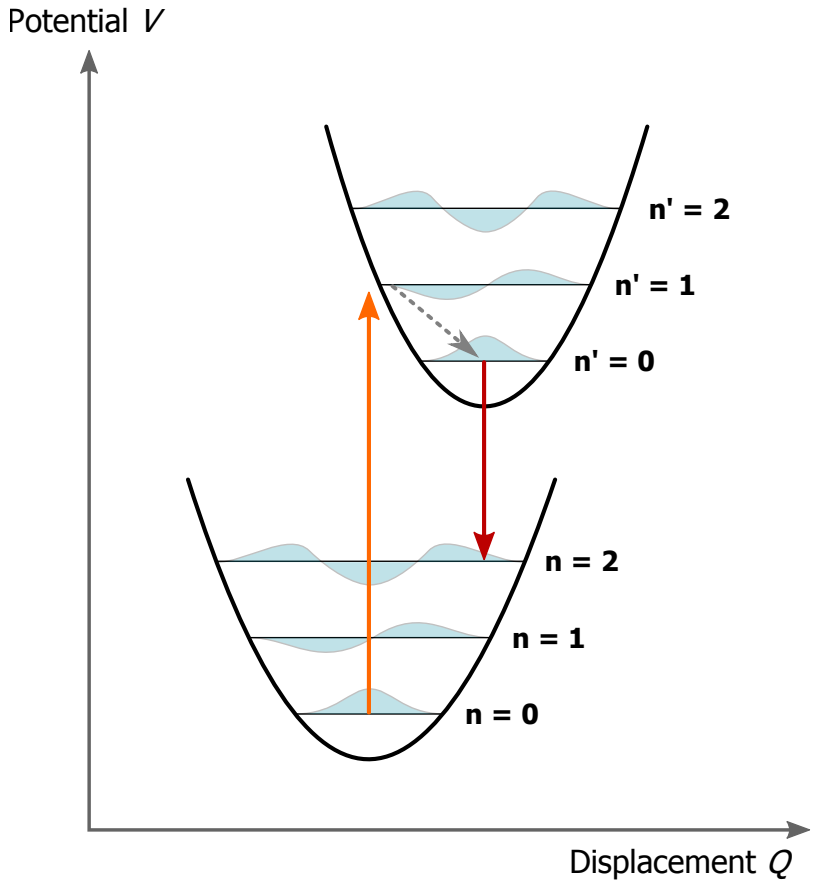

Figure 1.2 Illustration of electron-phonon coupling in fluorescence. The vibrational modes are approximated by the levels of harmonic potentials in the ground and excited electronic states (black parabolae), with the phonon numbers n or n' and the wavefunctions of the harmonic oscillator (light blue curves) represented on each vibrational level. The system is excited from the ground state to a vibrational level of the excited state (orange arrow) and then decays to a lower vibrational level in the excited state (dashed grey arrow). Fluorescence takes place towards the vibrational levels of the ground state (dark red arrow), with probabilities corresponding to the wavefunction overlaps between initial and final states.

Experimentally, this electron-phonon coupling is quantified by the Huang-Rhys factor S defined by $exp(-S) = I_{ZPL}/I_{tot}$, with I_{ZPL} and I_{tot} being respectively the integrated emission intensity of the ZPL and the total emission intensity [120]. For an SiV^- ensemble, a Huang-Rhys factor around 0.24 is generally reported [93, 48, 94], which means that about 80% of the emission is concentrated into the ZPL. Values as low as 0.05 have been reported for ensemble and single centres [94, 97, 121, 122].

Generally, defects containing heavy atoms tend to present a low electron-phonon coupling [123, 124]. In comparison, the NV^- centre is associated with a Huang-Rhys factor of 3.2 leading to only 4% of the total emission occurring in the ZPL even around 4 K. The rest of the fluorescence is taken by a 100 nm wide ensemble of phonon sidebands [48], as shown in Fig. 1.3 where we compare the fluorescence spectra of NV^- and SiV^-.

The low electron-phonon coupling in the fluorescence of the SiV^- indicates that there is little change in the charge distribution between ground and excited states. This can be linked to the inversion symmetry causing electronic wavefunctions involved to be relatively symmetric [99].

Fluorescence from the neutral charge state of the SiV centre, SiV^0, has been predicted by computational studies [95] and observed at 946 nm in optical absorption and photoluminescence [97]. However, with a Huang-Rhys factor of 1.5, the optical properties of SiV^0 do not match those of SiV^- [97].

This strong emission into the ZPL for SiV^- is one of the most important features of its optical properties, as those photons can be used as flying qubits and vectors of entanglement, unlike emission involving phonons [125, 65].

Reports about the quantum efficiency of the SiV^- centre are contradictory. The comparison between photoluminescence and calorimetric absorption spectroscopy suggests a very large radiative efficiency above 80% [126]. On the other hand, the quantum efficiency has been measured to be about 5% by comparison with a dye of known efficiency at 77 K in a diamond film [127], and values up to 9% have been reached in nanodiamonds close to a metallic surface by evaluation of the collection efficiency [115]. Recent experiments on single SiV^- centres in diamond nanobeams report values of about 10% [128]. A relatively low quantum yield can come from a quenching of colour centre luminescence in environments rich in defects, which act as non-radiative recombination centres [115, 129]. Alternatively, multi-phonon processes can make emitters in the near infrared prone to non-radiative decay, as shown by the temperature dependence of the lifetime of the SiV^- [130]. In comparison, a quantum efficiency of 70% has been inferred for NV^- centres [131, 132].

At temperatures below 50 K, a characteristic fine structure of the ZPL composed of four peaks appears [89, 90, 133], as shown in Fig. 1.4a for an SiV^- ensemble in bulk diamond. Those four peaks can be gathered into two equally spaced doublets. It is therefore assumed that the level structure of the centre is made of a ground and excited state, each split into two orbital branches, as represented in Fig. 1.4b [48, 90, 133].

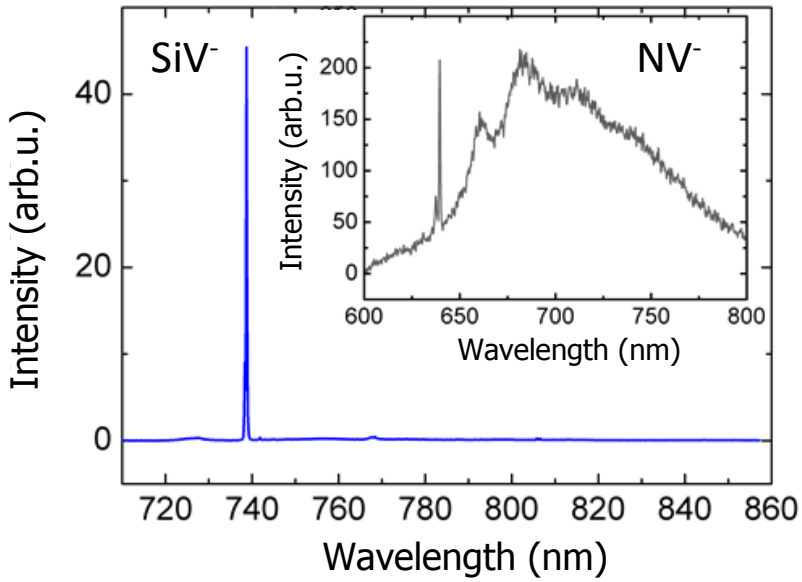

Figure 1.3 Fluorescence spectra of SiV^- (blue curve) and NV^- (grey curve in inset) at 4 K. The NV^- spectrum displays a narrow zero-phonon line at 637 nm and broad phonon sidebands at longer wavelengths accounting for 96% of the fluorescence. The SiV^- displays a narrow zero-phonon line at 737 nm which accounts for about 80% of the fluorescence. The phonon sidebands are in comparison too weak to be clearly visible with a linear intensity scale.

The splitting of the ground state corresponds to the splitting of each doublet and the splitting of the excited state, to the spectral distance between the centres of those two doublets. This attribution is deduced from the comparison between the expected Boltzmann population of the levels and the temperature dependence of absorption and photoluminescence [89, 90]. This also indicates that termalisation occurs between the orbital branches within the ground and excited states.

This level structure has several suggested origins. A proposed explanation for the splitting of the ground and excited states is a tunnel coupling of the electronic state between the two sides of the silicon atom [98]. Another possibility arises from group theory, according to which the split-vacancy configuration assumed for the centre yields a D_{3d} symmetry [97, 95, 96]. This symmetry is associated with doubly degenerate states for the ground and the excited states [95]. Then, a spin-orbit coupling or the Jahn-Teller effect, the latter corresponding to a shift of the silicon atom along the $[1\bar{1}0]$ or $[11\bar{2}]$ directions, could be responsible for a lifting of the degeneracy of those states [96]. This deformation of the centre would result in a C_2 or D_2 symmetry, which is consistent with polarisation [123, 134] and uniaxial stress measurements [135].

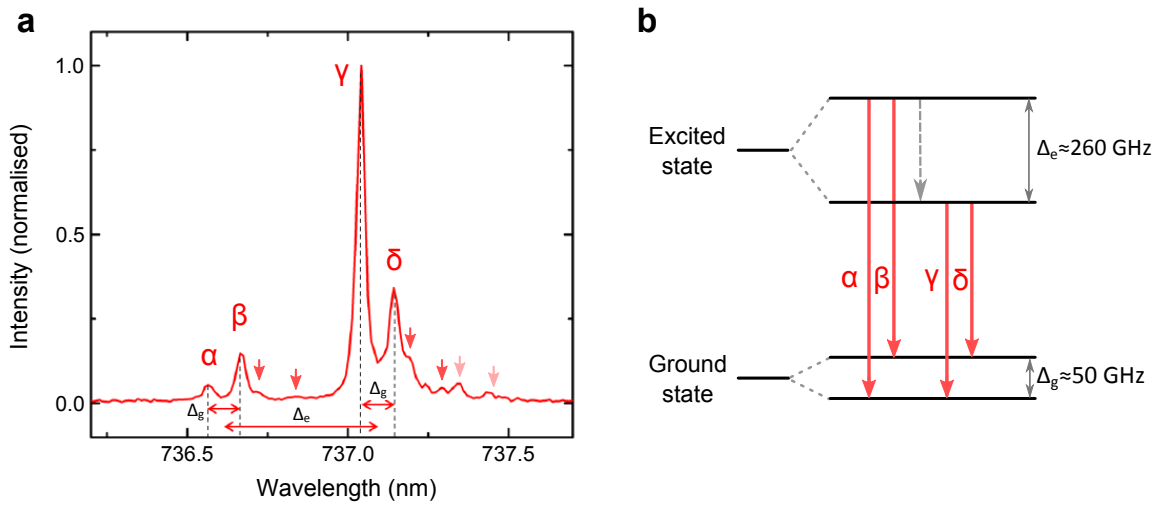

Figure 1.4 Fluorescence fine structure at low temperature. (a) Photoluminescence spectrum of an ensemble of SiV^- centres at 4 K. Δ_g and Δ_e correspond to the splittings of the ground and excited states, respectively. The four main transitions, labelled from α to δ, correspond to SiV^- centres containing ^{28}Si (92.3% natural abundance). Replicas of the four peaks shifted to larger wavelengths correspond to SiV^- with ^{29}Si (4.6%) (red arrows) and ^{30}Si (3.1%) (pink arrows, only the more intense doublet is visible) [91]. (b) Representation of the energy levels involved in the fluorescence spectrum: the ground and excited states are each split into two orbital branches separated by approximately 50 GHz and 260 GHz respectively [48]. The transitions corresponding to the peaks in (a) are indicated by red arrows.

In bulk diamond, the splitting of the ground state is typically about 50 GHz and the splitting of the excited state is about 260 GHz [48]. In nanodiamonds, those splittings and even the central wavelength are very different and vary from centre to centre. It has been reported that mechanical strain causes the central wavelength of the ZPL to shift by up to 20 nm at room temperature [89, 48, 94, 123]. Those variations are thus suggested to arise from the likely presence of strain in nanodiamonds grown on foreign substrate. The influence of strain on SiV^- properties will be further developed in Chapter 5.

Let us also mention that, in the autocorrelation measurements, a bunching of the $g^{(2)}$ function indicates a deexcitation process involving a shelving state, the exact nature of which remains unclear [94].

In more recent experiments, the SiV^- centre has been shown to be a good source of indistinguishible photons through Hong-Ou-Mandel experiments [136]. Furthermore, the low inhomogeneous broadening among several SiV^- centres [137] and the near

lifetime-limited linewidth of focused-ion-beam-implanted centres [138] make it ideal for interfacing several emitters in a quantum network. Those properties arise from the inversion symmetry of the SiV^- which makes it insensitive to first-order electric field noise [136, 116]. Finally, the remarkable optical properties of the SiV^- centre have recently been used to realise a bright fibre-coupled source of coherent photons [139] and a quantum-optical switch at the single-photon level controlled by a single SiV^- centre in a diamond nanobeam [128].

1.3 Electronic spin

Besides optical properties, another crucial aspect of a colour centre for quantum information processing is the accessibility of a spin degree of freedom used to perform quantum gates. ESR studies have determined that the ground state of the SiV^0 is characterised by a spin $S = 1$. They have also shown that a charge state of the centre different from SiV^0 possesses a spin $S = 1/2$ [140]. Although SiV^- is predicted to possess a spin $S = 1/2$ [97, 95, 96], this signal could not unambiguously be attributed to it and the spin state of the SiV^- remains elusive.

The confirmation of the spin state of the SiV^- would open a large field of potential applications, especially if this spin is optically accessible. It could be used as a qubit, a spin-photon interface in a quantum network and most of the applications which have been demonstrated for NV^- centres could potentially be implemented with SiV^-, such as the creation of a quantum register by coupling to a superconducting qubit [141, 142], entanglement of two spin qubits associated to two distant NV^- centres [65, 66] or entangling nuclear spins by using the NV^- electron spin as an ancilla [143, 68]. Showing evidence of an optically accessible spin state in the SiV^- centre therefore presents considerable interest, especially in association with its remarkable fluorescence properties.

Chapter 2

Optical signatures of spin

The optical properties of the SiV^- centre make it an advantageous source of single photons to encode and transfer information. In order that the SiV^- centre could be used as a node of a quantum network [86], in addition to those desirable photonic properties, it requires a storage qubit with which information processing could be performed. To that purpose, quantum spins are good candidates as qubits, thanks to their potential to exhibit long coherence times [10]. As we mentioned in Chapter 1, the neutrally charged SiV has been shown to possess an electronic spin $S = 1$ and an electronic spin $S = 1/2$ is expected from theory [95] for the negatively charged SiV. However, no electronic spin has yet been evidenced through electron paramagnetic resonance.

In this chapter, we report optical signatures of an electronic spin $S = 1/2$ for the negatively charged SiV centre. Applying a magnetic field to the SiV^- results in the splitting of its optical transitions in a way which is compatible with a spin degree of freedom. We use resonant excitation in order to selectively populate excited states and reveal in the subsequent fluorescence optical selection rules which confirm that the SiV^- possesses a spin $S = 1/2$. The analysis of the SiV^- fluorescence under a magnetic field allows us to design a model which deepens our understanding of this quantum system. The results presented in the chapter were obtained with Tina Müller and Christian Hepp, and have been published in Refs. [144, 145].

2.1 Experimental conditions

2.1.1 Experimental setup

The experimental setup used for this experiment is presented in Fig. 2.1. The cryogenic part of this setup consists of a helium bath cryostat. The sample is placed into an insert dipped into liquid helium. The insert contains about 15 mbar of helium gas, acting as exchange gas and thus allowing the sample to be held at a constant temperature of approximately 4 K. A confocal microscope is mounted on top of the cryostat and is used for excitation and detection of SiV^- centres. The excitation is performed using a Ti:sapphire laser (Mira 900, Coherent) tuned to a wavelength of 700 nm. The laser is coupled to a single mode fibre connected to the excitation arm of the microscope. In the excitation arm, two 10 nm band-pass filters centred around 700 nm are used to eliminate Raman scattering generated by the laser in the optical fibre. The laser is then directed down into the insert and is focused onto the sample by an aspheric lens with NA = 0.68 (Thorlabs C330TME-B). Piezoelectric stages (ANPxyz 101/LT xyz-positioners, Attocube) on which the sample is mounted allow us to position the sample with respect to the aspheric lens. The emitted fluorescence is collected through the same lens and is sent through a single mode optical fibre from the detection arm of the confocal microscope to a spectrometer (SpectraPro 2750, Princeton Instruments) with a 1800 lines/mm grating, giving a spectral resolution of 0.018 nm. The reflected laser light is used to image the sample surface with a CCD camera in the detection arm and is filtered out before the optical fibre by long-pass filters to avoid parasitic reflections in the spectrometer and potential inelastic scattering in the fibre. In the cryostat, a superconducting coil mounted around the insert where the sample lies, allows us to apply a tunable magnetic field aligned with the optical axis up to 7 T.

2.1.2 Sample

We study an SiV^- ensemble in a 80-100 nm thick diamond film grown as described in Ref.[133]. The growth was performed by Hadwig Sternschulte and Doris Steinmüller-Nethl by hot filament chemical vapour deposition (CVD) on a type Ib high pressure and high temperature (HPHT) parallelepiped diamond, from the company Sumitomo. A homo-epitaxial growth combined with optimised growth parameters (low methane fraction (0.26% methane in H_2) and slow growth) was employed to minimise strain and defects in the sample [133]. SiV centres were incorporated during the growth due

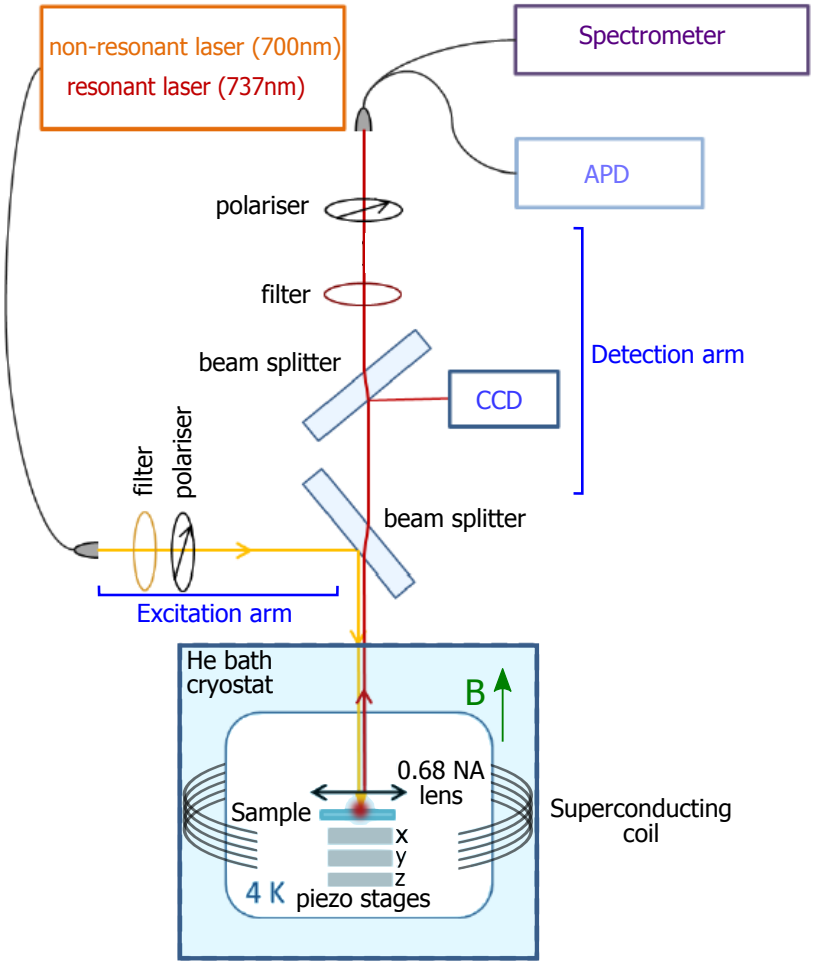

Figure 2.1 Schematic of the experimental setup used for fluorescence measurements at 4 K and under magnetic field.

to contamination of the growth chamber by silicon. The HPHT diamond substrate and the CVD-grown film are oriented along the [001] crystallographic direction. As a consequence, the four possible orientations of SiV centres all have the same angle to the magnetic field applied along [001].

2.2 Magnetic field dependence

We investigate the variation of the optical transitions of an ensemble of SiV^- centres with the magnitude of a magnetic field. We acquire non-resonant photoluminescence spectra of the zero-phonon line fine structure around 737 nm for values of the applied

magnetic field from 0 to 7 T. The excitation power from the laser at 700 nm is set below the saturation of the ensemble of emitters to minimise power broadening. Figure 2.2a displays the obtained spectra as a function of the applied magnetic field. A two-dimensional plot with the emission intensity being colour-coded on a logarithmic scale, as shown in Fig. 2.2b, allows us to follow the evolution of each transition. At zero magnetic field, we label the four optical transitions from α to δ, as introduced in Section 1.2. The lines indicated by arrows correspond to SiV^- centres comprising a ^{29}Si or a ^{30}Si atom, as mentioned in Section 1.2. As the magnetic field is increased, we can see a clear splitting of each of the four original transitions, similar to what was reported by Sternschulte *et al.* [135]. Since the four possible orientations of the SiV^- centres all make the same angle to the magnetic field, the observed splitting is the same for all of them and does not correspond to the superposition of several splittings of different individual SiV^- centres. We can count a total of 14 visible transitions with large disparities in intensity. From the brighter transitions γ and δ, it appears that each transition splits into four. It is likely to be also the case for transitions α and β with some transitions being too dim to be observed clearly.

Such a splitting of the transitions can originate from a splitting of the two branches of the excited state as well as from those of the ground state. However, intensity ratios of the four-peak structure without magnetic field indicate that ground and excited states should present the same degeneracy [90]. Consequently, the observed magnetic field response indicates that each energy level splits into two, which matches the expected behaviour for $S = 1/2$. The splitting into four transitions is the result of different effective gyromagnetic ratios between ground and excited states, as illustrated in Fig. 2.3, as similar effective gyromagnetic ratios would cause the two central transitions to overlap. Those results thus support the assumption of a spin $S = 1/2$. However, we cannot rule out at this stage that this splitting does not originate from a purely orbital Zeeman effect.

2.3 Resonant excitation

In order to confirm that the observed magnetic field splitting is caused by a spin $S = 1/2$, we need to demonstrate the presence of selection rules in the optical transitions. To do so, we implement resonant excitation so that we can populate selectively each individual excited state level and analyse the optical transitions originating from each of them.

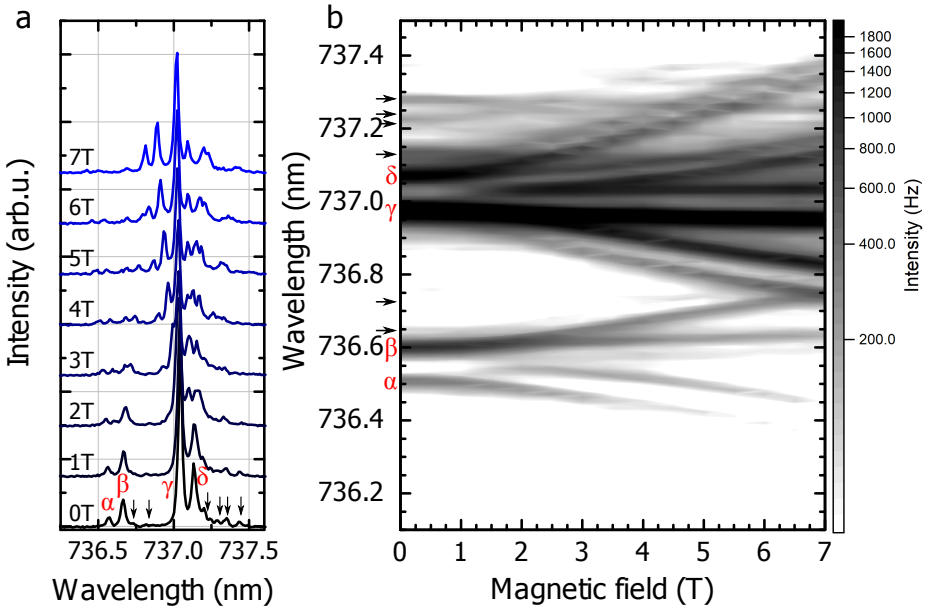

Figure 2.2 Magnetic field dependence for an SiV^- ensemble, with a magnetic field along the [001] crystallographic axis, thus making an angle of 54.7° to all possible orientations of the SiV centres. (a) Individual spectra plotted from 0 to 7 T on top of each other with a constant offset. The excitation power is well below saturation. (b) Fluorescence spectra plotted as a function of the magnetic field. The intensity is represented on a logarithmic grey scale. The four transitions at 0 T are labelled from α to δ. Black arrows indicate transitions from SiV^- with ^{29}Si and ^{30}Si, as in Fig. 1.4a.

2.3.1 Resonant excitation in the absence of magnetic field

Using the same experimental setup, we use a tunable diode laser in the region of 737 nm (DL 100 Pro Design, Toptica) for resonant excitation. The laser is coupled to the same single mode fibre as the one used for non-resonant excitation and the band-pass filters around 700 nm in the excitation branch of the microscope are removed. The reflected laser light is suppressed by a factor up to 2×10^6 by polarisation rejection [146], using two crossed polarisers, one in the excitation arm and the other in the detection arm.

We start by implementing resonant excitation of the SiV^- ensemble in the absence of external magnetic field in order to explore potential orbital selection rules. We tune the laser to excite all four transitions in turn and measure the spectra of the resulting fluorescence, as shown in Fig. 2.4. The relative intensities of the peaks when resonantly exciting the higher energy transitions (α and β), which originate from the upper branch of the excited state, are comparable to those obtained in non-resonant photoluminescence, indicating that there are no selection rules. When resonantly exciting transition γ, which originates from the lower branch of the excited state, the

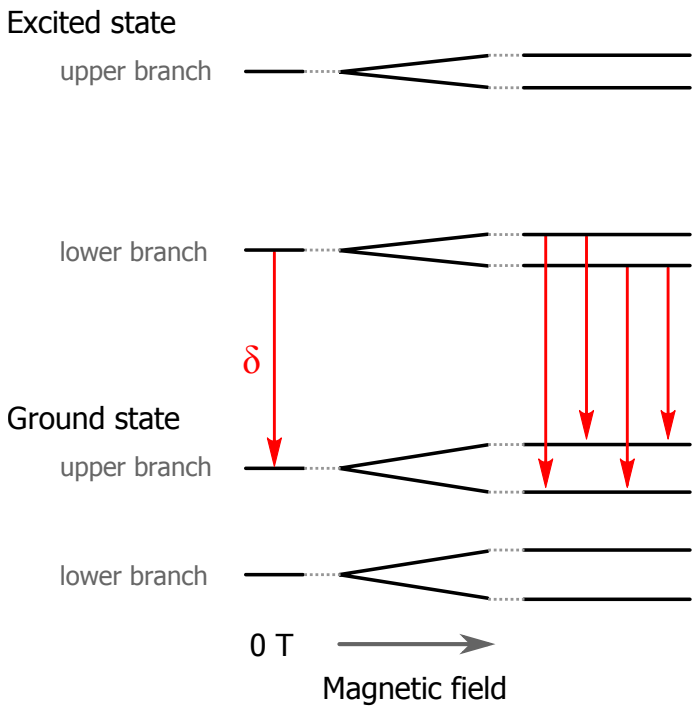

Figure 2.3 Schematic of the splitting of the SiV^- energy levels in the presence of a magnetic field. Each orbital branch in the ground and excited states splits into two. Each optical transition at 0 T, illustrated for transition δ, gives rise to four transitions at non-zero magnetic field, as depicted by red arrows.

obtained spectrum presents relatively weaker intensities for transitions α and β. This can be explained by the fact that, in order to see fluorescence from transitions α and β, the system needs to be thermally excited to the upper branch of the excited state. At 4 K, Boltzmann statistics indicates that the upper branch of the excited state is about 20 times less populated than the lower one, which is consistent with the observed relative intensities. This thermalisation in the excited state is relatively fast, as it occurs before spontaneous emission, the timescale of which is about 1-4 ns [89, 94, 115].

We note that in Fig. 2.4b, the ratio between SiV^- and laser photons is about $9:1$. This value is estimated by integrating the intensity of the peaks after fitting them with Lorentzian functions and assuming that the contribution of transition β is comparable to its relative intensity with the other peaks in non-resonant excitation. This value, although promising, is far from the $100:1$ value, achieved for single quantum dots [146], and shows that efforts are necessary to increase the collection efficiency of SiV^- photons.

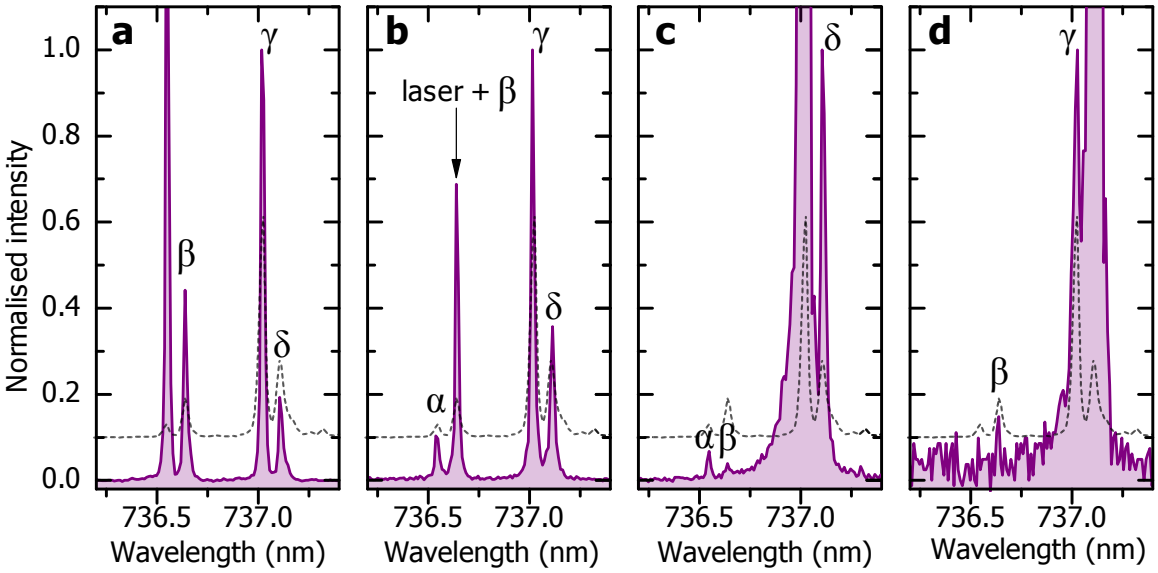

Figure 2.4 Fluorescence spectra of an SiV^- ensemble in the absence of magnetic field, upon resonant excitation of transition α (a), transition β (b), transition γ (c) and transition δ (d). The large peak on each spectrum corresponds to leakage from the resonant laser. On each spectrum, the spectrum obtained under non-resonant excitation is plotted as a grey dashed curve.

We now scan the laser frequency over transition α and integrate the intensity of transition γ, as shown in Fig. 2.5a. A Lorentzian fit gives a full width at half maximum of 9.0 ± 0.7 GHz for the absorption linewidth. This is consistent with the inhomogenous broadening of the ensemble under non-resonant excitation [147] as evidenced by the shift of transitions when the laser frequency is scanned and resonantly excites sub-ensembles with slightly shifted resonance frequencies, as shown in Fig. 2.5b.

2.3.2 Resonant excitation in the presence of magnetic field

We now proceed to resonant excitation of Zeeman sublevels in the presence of an applied magnetic field. We apply a magnetic field of 4 T along the [001] direction, a value at which most transitions are resolved. For clarity, we label the Zeeman-split energy levels from 1 to 4 in the ground state and from A to D in the excited state, as illustrated in Fig. 2.6. At that magnetic field, two of the ground state levels, 2 and 3, have anticrossed (this will be developed in Section 2.4).

We excite resonantly transition C1, from the ground state level 1 to the excited state level C. The resulting fluorescence, displayed in red in Fig. 2.7a, comprises only about half of the transitions visible in the non-resonant spectrum, plotted as a grey

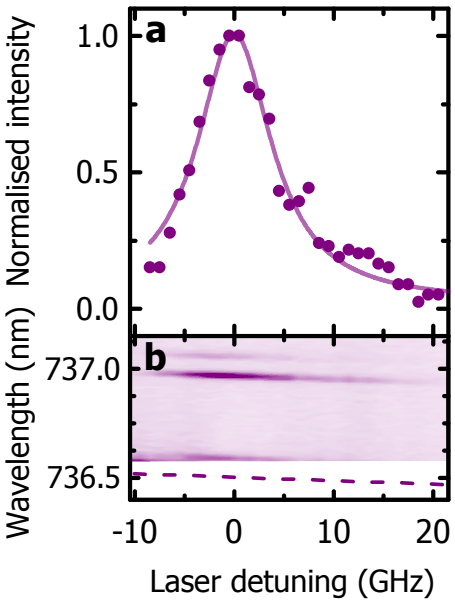

Figure 2.5 Photoluminescence excitation of an SiV^- ensemble. (a) Normalised fluorescence intensity of transition γ (purple dots) measured as the laser frequency is scanned over transition α. The laser power is set below saturation. The obtained absorption profile of transition α is fitted with a Lorentzian function with a full width at half maximum of 9.0 ± 0.7 GHz. (b) Fluorescence spectra measured while sweeping the laser frequency over transition α. The laser position is indicated by a purple dashed line. Transitions γ and δ are visible and appear to shift with the laser, indicating that SiV^- sub-ensembles with slightly different resonance wavelengths are excited successively.

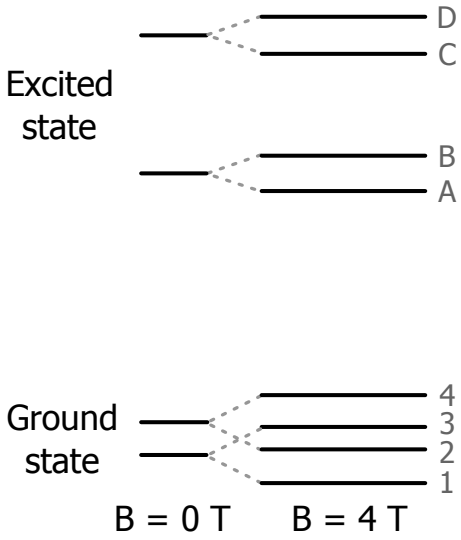

Figure 2.6 Labelling of Zeeman-split energy levels. Ground state levels are labelled from 1 to 4 and excited state levels from A to D.

dashed curve. Traced back to the energy levels (see Fig. 2.7b), the visible transitions originate exclusively from the excited state levels C and A, which both have the same Zeeman response and are expected to correspond to $m_S = -1/2$. From those levels, transitions occur towards all the ground states.

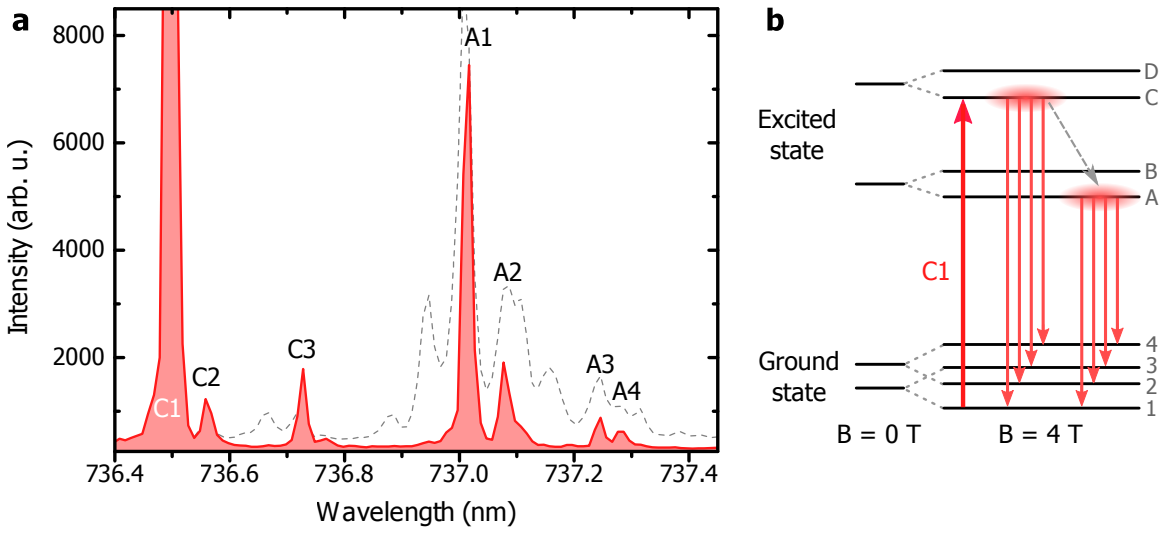

Figure 2.7 Resonant fluorescence of an SiV^- ensemble at 4 T. (a) Spectrum obtained when resonantly exciting transition C1 (red shaded curve). The corresponding spectrum obtained at 4 T under non-resonant excitation is displayed as a grey dashed curve (not to scale). Each transition from which fluorescence is observed is labelled according to its ground and excited state levels, as displayed in (b). (b) Representation of the energy level diagram at 4 T. Transition C1 is excited (large red arrow) and fluorescence is observed from a subset of transitions, as indicated by light red arrows. The grey dashed arrow indicates fast thermalisation from the upper branch of the excited state to the lower branch.

We repeat this operation and excite transition D4, populating the excited state level D, which has the opposite Zeeman response and is expected to correspond to $m_S = +1/2$. The obtained fluorescence spectrum is shown in Fig. 2.8a in blue, alongside the fluorescence from C1 in red and the non-resonant spectrum as a grey dashed curve. Once again, only about half of the transitions are visible. The transitions which are visible when resonantly exciting D4 correspond to those which are not visible when resonantly exciting C1. This leads to the two fluorescence spectra being complementary to each other and together reconstructing the non-resonant spectrum. When traced back to the energy level diagram shown in Fig. 2.8b, the visible transitions when exciting D4 occur from levels D and B towards all the ground state levels.

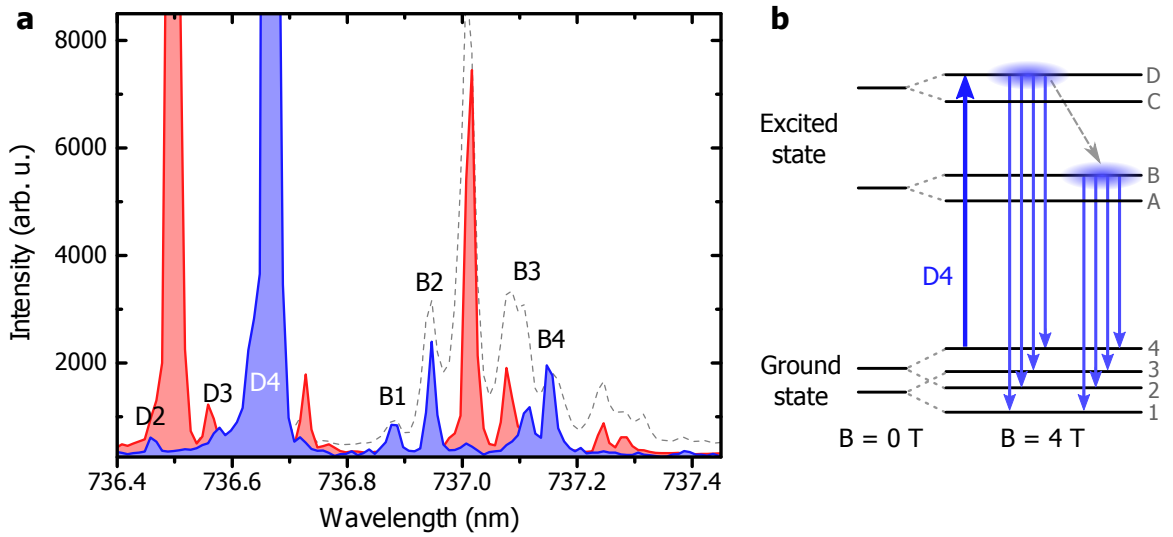

Figure 2.8 Resonant fluorescence of the SiV^- ensemble at 4 T. (a) Spectrum obtained when resonantly exciting transition D4 (blue shaded curve). The spectrum obtained at 4 T under non-resonant excitation is displayed as a grey dashed curve (not to scale) and the spectrum obtained through resonant excitation of transition C1 is plotted as a red shaded curve (to scale). Each transition from which fluorescence is observed is labelled according to its ground and excited state levels, as displayed in (b). (b) Representation of the energy level diagram at 4 T. Transition D4 is excited (large blue arrow) and fluorescence is observed from a subset of transitions, as indicated by light blue arrows. The grey dashed arrow indicates fast thermalisation from the upper branch of the excited state to the lower branch.

To quantify the complementarity of the two resonant spectra, we fit the transition peaks with Lorentzian functions and, for each transition, compare the integrated peak when either C1 (red) or D4 (blue) is excited resonantly, as seen in Fig. 2.9a. The contrast is clear for all transitions, and even exceeds 9 : 1 for some of them, such as B1, A1, B2 and B4. For others, the contrast may be reduced due to their low intensity, such as A3 and A4, or due to the overlap with another peak, such as A2 and B3. The thermalisation process among excited state levels thus displays a strong selectivity. This selectivity can only be explained by the fact that those levels have different spin orientations, which cannot be flipped by the phonons responsible for thermalisation. This is consequently a clear optical signature that the SiV^- possesses a spin $S = 1/2$.

The fact that transitions occur towards all the ground state levels is however not expected since optical transitions are dipolar electric and hence ought to be spin-preserving. We examine the ratios between the intensities of transitions which occur between ground and excited states with opposite expected spin orientations and those

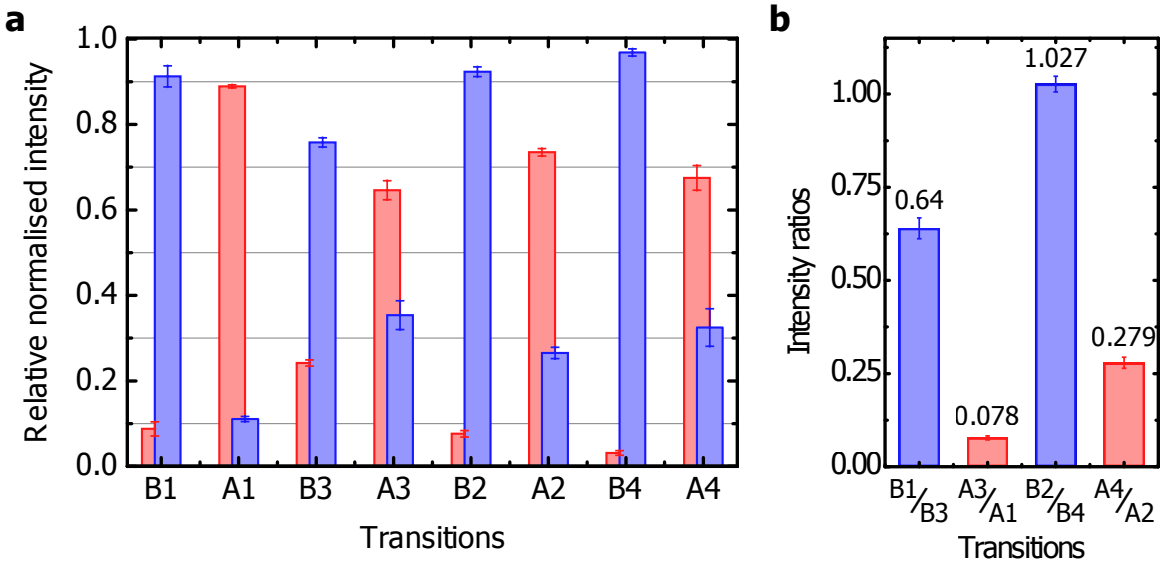

Figure 2.9 Comparison of transition intensities under resonant excitation. (a) Relative intensities of each luminescent transition (indicated along x-axis), depending on whether transition C1 (red) or transition D4 (blue) is excited resonantly. For each of the two spectra in Fig. 2.8, the intensity of each transition has been normalised by the total intensity of all the transitions of the spectrum. Then, this normalised intensity for one spectrum has been divided by the sum of the normalised intensities of the peak in both spectra. (b) Intensity ratios between transitions between states with opposite Zeeman response (supposedly spin-flipping) and transitions between states with the same Zeeman response (supposedly spin-preserving), for resonant excitation of C1 (red) and D4 (blue). In (a) and (b), the error bars correspond to the full width at half maximum of the Gaussian profile of the white noise taken far from the peaks.

between levels with the same expected spin orientations, as shown in Fig. 2.9b. While some of the ratios are low as expected, the majority of them are relatively high with even the ratio between B2 (opposite spin orientations) and B4 (same spin orientations) reaching 1. A deeper investigation into the physics of the SiV^- and the exact nature of its energy states is thus required to fully understand its optical transitions.

2.4 Group theoretical model

We introduce here a model developed by Christian Hepp, Victor Waselowski and Jeronimo Maze and described in details in Refs.[148, 149]. This model uses group theory to understand and simulate the physics at play in the SiV^- centre.

Similarly to a molecule, the electronic orbitals of the SiV^- centre arise from the interaction between the atomic orbitals of the atoms which constitute it. It was shown

that in the case of the SiV^-, these orbitals are mainly the sp^3-orbitals from the dangling bonds of the six carbon atoms around the silicon atom [99]. The symmetry of the arrangement of those constitutive atoms imposes restrictions on how their orbitals can overlap and form the SiV^- orbitals. Such restrictions can be predicted by group theory [150, 151].

The combination of the different symmetry operations under which the SiV is invariant determine that the SiV belongs to the D_{3d} symmetry group [95]. Among them, the most notable ones are an inversion symmetry with the inversion centre at the location of the silicon atom, and a rotation axis of order 3 labelled C_3, which we will refer to as the SiV axis, as represented in Fig. 2.10.

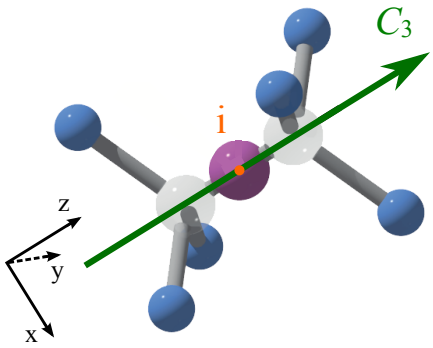

Figure 2.10 Representation of the SiV centre, with the silicon atom (purple sphere) located in the middle of two vacancies (light grey spheres) and the six nearest neighbour carbon atoms (blue spheres). The SiV has a centre of inversion in the middle of the two vacancies (orange dot) and a rotation axis of order 3 along the two vacancies (green arrow), and referred to as the SiV axis. A reference frame is attached to the SiV with orthogonal axes x, y and z, z being aligned with the SiV axis and x lying in one of the three planes of symmetry containing two carbon atoms in symmetric positions with regards to the centre of inversion.

The D_{3d} symmetry group is associated with a set of irreducible representations corresponding to the possible linear combinations of atomic orbitals that can form the SiV^- orbitals. Among them, density functional theory simulations show that the ground and excited states of the SiV^- involved in optical transitions correspond to orbitals of symmetry E_g and E_u respectively [96, 99]. They are referred to as e_g and e_u orbitals and have each a twofold orbital and a twofold spin degeneracy.

By combining those results with the analysis of the spectral characteristics of the SiV^- fluorescence, a Hamiltonian can be constructed for the ground state and for the excited state. In both cases, this Hamiltonian comprises the following components: a

spin-orbit coupling, the Jahn-Teller effect and the Zeeman effect, for each of which group theory allows one to determine their vanishing matrix elements. For the spin-orbit coupling $\lambda\vec{L}\cdot\vec{S}$, where λ is the coupling constant, $\vec{L}$ is the orbital momentum and $\vec{S}$ is the spin, a group theoretical analysis shows that the L_x and L_y terms can only affect states of symmetry A_{1g} or A_{2u}, while only the L_z term acts on the E-symmetric orbitals [148] (the z-component being taken along the SiV axis and the x- and y-components are orthogonal to it, as shown in Fig. 2.10). This leads to a spin-orbit coupling of the form $\lambda L_z S_z$. The spin-orbit coupling thus acts in the SiV^- as an inherent quantisation axis for the spin along the SiV centre axis. This results in the following spin-orbit Hamiltonian, when expressed in the basis $\{|e_x\uparrow\rangle, |e_x\downarrow\rangle, |e_y\uparrow\rangle, |e_y\downarrow\rangle\}$ (where e_x and e_y constitute the orbital basis, with e standing for e_g in the ground state and e_u in the excited state, and $|\uparrow\rangle$ and $|\downarrow\rangle$ form the spin basis, with the spin aligned along z):

$$\mathcal{H}_{SO} = \begin{pmatrix} 0 & 0 & -i\lambda_{g/u}/2 & 0 \\ 0 & 0 & 0 & i\lambda_{g/u}/2 \\ i\lambda_{g/u}/2 & 0 & 0 & 0 \\ 0 & -i\lambda_{g/u}/2 & 0 & 0 \end{pmatrix} \tag{2.1}$$

where $\lambda_{g/u}$ are the spin-orbit coupling constants in the ground (g) and excited states (u).

Its eigenvalues $\pm\lambda/2$ and corresponding eigenstates can be deduced:

$$+\frac{\lambda}{2}\begin{cases} |e_+\uparrow\rangle &= -\frac{1}{\sqrt{2}}\left(|e_x\uparrow\rangle + i\,|e_y\uparrow\rangle\right) \\ |e_-\downarrow\rangle &= \frac{1}{\sqrt{2}}\left(|e_x\downarrow\rangle - i\,|e_y\downarrow\rangle\right) \end{cases} \tag{2.2}$$

$$-\frac{\lambda}{2}\begin{cases} |e_+\downarrow\rangle &= -\frac{1}{\sqrt{2}}\left(|e_x\downarrow\rangle + i\,|e_y\downarrow\rangle\right) \\ |e_-\uparrow\rangle &= \frac{1}{\sqrt{2}}\left(|e_x\uparrow\rangle - i\,|e_y\uparrow\rangle\right) \end{cases} \tag{2.3}$$

It is important to notice that the spin-orbit interaction, despite acting on the spin and the orbitals, does not lift the spin degeneracy, as shown in Fig. 2.11.

Another contribution to the Hamiltonian is the dynamic Jahn-Teller effect. It consists in the coupling of electronic orbitals with the vibrational modes of the nuclei (the six carbon atoms and the silicon atom forming the SiV), resulting in a coupling between the different electronic orbitals. Following a group theoretical analysis, it can

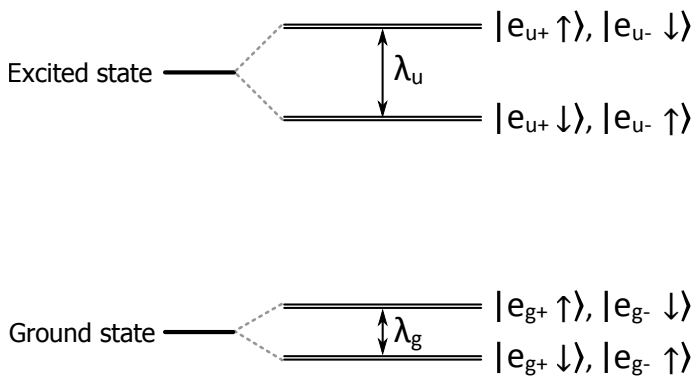

Figure 2.11 Energy levels and eigenstates of the spin-orbit Hamiltonian. The spin-orbit Hamiltonian partially lifts the fourfold degeneracy of the initial ground and excited states (orbital twofold degeneracy and spin twofold degeneracy) without lifting the spin degeneracy as eigenstates of different spin projections have the same energy.

be expressed in the $\{|e_x\uparrow\rangle, |e_x\downarrow\rangle, |e_y\uparrow\rangle, |e_y\downarrow\rangle\}$ basis as:

$$\mathcal{H}_{JT} = \begin{pmatrix} \xi_x & 0 & \xi_y & 0 \\ 0 & \xi_x & 0 & \xi_y \\ \xi_y & 0 & -\xi_x & 0 \\ 0 & \xi_y & 0 & -\xi_x \end{pmatrix} \tag{2.4}$$

where $\xi_{x/y}$ are the Jahn-Teller coupling strengths for the x and y components and their values can differ between the ground and excited states.

Both the spin-orbit coupling and the Jahn-Teller effects are responsible for lifting the twofold orbital degeneracy of the e_g ground state and the e_u excited state, each with a splitting $\sqrt{\lambda_{g/u}^2 + 4\xi_{g/u}^2}$, with $\xi_{g/u} = \sqrt{\xi_x^2 + \xi_y^2}$ the strengths of the Jahn-Teller coupling in the ground and excited states. This leads to the four energy levels in the absence of magnetic field.

It is worth noting that the Hamiltonian of the Jahn-Teller effect is very similar to that of uniaxial strain (see Section 5.3). The model thus does not allow us to distinguish between a dynamic Jahn-Teller effect and a possible internal strain of SiV centres, possibly linked to the large size of the silicon atom. A previous experiment on the evolution of the optical transitions of SiV^- upon application of uniaxial strain along the [001]-direction had extrapolated a negative stress value of -60 MPa [135]. However, this value was extracted without consideration for the spin-orbit interaction and was thus attributing the zero-field splitting entirely to strain. A study of the

optical transitions of SiV^- at lower temperatures at which a dynamic Jahn-Teller effect might be quenched could contribute to distinguish which effect is at play.

Finally, the Zeeman effect $\mathcal{H}_{Zee}$ is introduced. Its orbital part only includes the L_z term (for the same reason as for the spin-orbit coupling) and is largely quenched by the Jahn-Teller interaction, as is commonly observed in solid-state defects [148, 152, 153]. It is of the form:

$$\mathcal{H}_{Zee,L} = f\gamma_L \begin{pmatrix} 0 & 0 & iB_z & 0 \\ 0 & 0 & 0 & iB_z \\ -iB_z & 0 & 0 & 0 \\ 0 & -iB_z & 0 & 0 \end{pmatrix} \tag{2.5}$$

where $f = 0.1$ is the quenching factor of the orbital gyromagnetic ratio $\gamma_L = \mu_B/\hbar$ (deduced from comparison to experimental spectra, as explained below), and B_z is the component of the external magnetic field along z.

The spin part of the Hamiltonian is:

$$\mathcal{H}_{Zee,S} = \gamma_S \begin{pmatrix} B_z & B_x - iB_y & 0 & 0 \\ B_x + iB_y & -B_z & 0 & 0 \\ 0 & 0 & B_z & B_x - iB_y \\ 0 & 0 & B_x + iB_y & -B_z \end{pmatrix} \tag{2.6}$$

where $\gamma_S = 2\mu_B/\hbar$ is the electron gyromagnetic ratio, and B_x and B_y are the components of the external magnetic field along x and y respectively. We can see that the external magnetic field has components in B_x and B_y coupling different spin projections as defined by the spin-orbit interaction. The magnetic field thus introduces some mixing of the spin. It can be practical to think of the external magnetic field and of the spin-orbit coupling as two competing quantisation axes for the SiV^- spin, along $\vec{B}$ for the magnetic field and along the SiV symmetry axis for the spin-orbit coupling.

The model then consists in determining the eigenvalues and eignestates of the total Hamiltonian $\mathcal{H}_{tot} = \mathcal{H}_{SO} + \mathcal{H}_{JT} + \mathcal{H}_{Zee}$. The respective contributions of the three physical effects and their parameters are extracted by fitting the energy differences of the simulated levels in the excited and ground states and the experimentally measured optical transitions, as shown in Fig. 2.12a for the SiV^- ensemble with the magnetic field at an angle of 57.4° to the SiV axes. While the parameters of the Zeeman effect are trivial to extract especially at high magnetic fields, the relative contributions of the spin-orbit and Jahn-Teller interactions are determined by the evolution of the transition frequencies with the magnetic field as the position and energy of the

level anticrossing depends on the relative strengths of the spin-orbit coupling and the transverse component of the magnetic field: for a larger spin-orbit interaction, the anticrossing occurs at higher values of the magnetic field and its energy is also higher. From this, it appears that the spin-orbit coupling, with coupling constants $\lambda_g \approx 45\,\text{GHz}$ and $\lambda_u \approx 255\,\text{GHz}$ is a very strong component in the Hamiltonian and is dominant over the Jahn-Teller effect ($\xi_g \approx 11\,\text{GHz}$ and $\xi_u \approx 20\,\text{GHz}$) in determining the zero-field orbital splitting. The intensity of the transitions can also be simulated. Considering that these transitions are dipolar electric (the SiV is much smaller than the wavelengths of the fluorescence), their intensity is proportional to the optical dipole matrix elements $\langle j|D_{x,y,z}|i\rangle$, where $D_{x,y,z}$ are the matrices of the electric dipole $\vec{D} = -e\vec{r}$ (e is the elementary charge and $\vec{r} = (x, y, z)$) and $|i\rangle$ and $|j\rangle$ are the initial and final simulated eigenstates respectively. These matrix elements are multiplied by the Boltzmann populations of the energy levels involved. Such a reconstructed fluorescence is shown in Fig. 2.12b. The intensities of the transitions depend on the orbital and spin components of the eigenstates, in particular, dipolar electric transitions between states with opposite spin orientations are forbidden.

This fitting procedure allows us to deduce the energy levels of the SiV^-, as shown in Fig. 2.13, where excited states are labelled from A to D and ground states from 1 to 4. We can see that the avoided crossings in the fluorescence spectra arise from the ground states labelled $|2\rangle$ and $|3\rangle$ undergoing an avoided crossing at around 1.5 T.

It is also possible to simulate the tomography of the different eigenstates by plotting the norms of the components of their density matrices, as exemplified in Fig. 2.14, at a magnetic field of 4 T at an angle of 57.4°. Due to the dominance of the spin-orbit coupling, the SiV^- states are expressed in the basis of the spin-orbit eigenstates $\{|e_+\uparrow\rangle, |e_+\downarrow\rangle, |e_-\uparrow\rangle, |e_-\downarrow\rangle\}$. We can see that while the excited state levels are strongly tagged by one of the two spin orientations along the SiV axis z, the ground state levels display spin orientations which correspond to superpositions of the original spin-orbit-dictated spin orientations. This arises due to the competition between external magnetic field and spin-orbit coupling to fix an effective quantisation axis for the spin. As the spin-orbit coupling is approximately five times stronger in the excited state than in the ground state (about 250 GHz vs 50 GHz respectively), the spin remains mainly dictated by the spin-orbit interaction in the excited state, while the relative importance of the external field is much stronger in the ground state. As a consequence, the effective quantisation axes differ between the ground and excited states resulting in all optical transitions being allowed in this configuration.

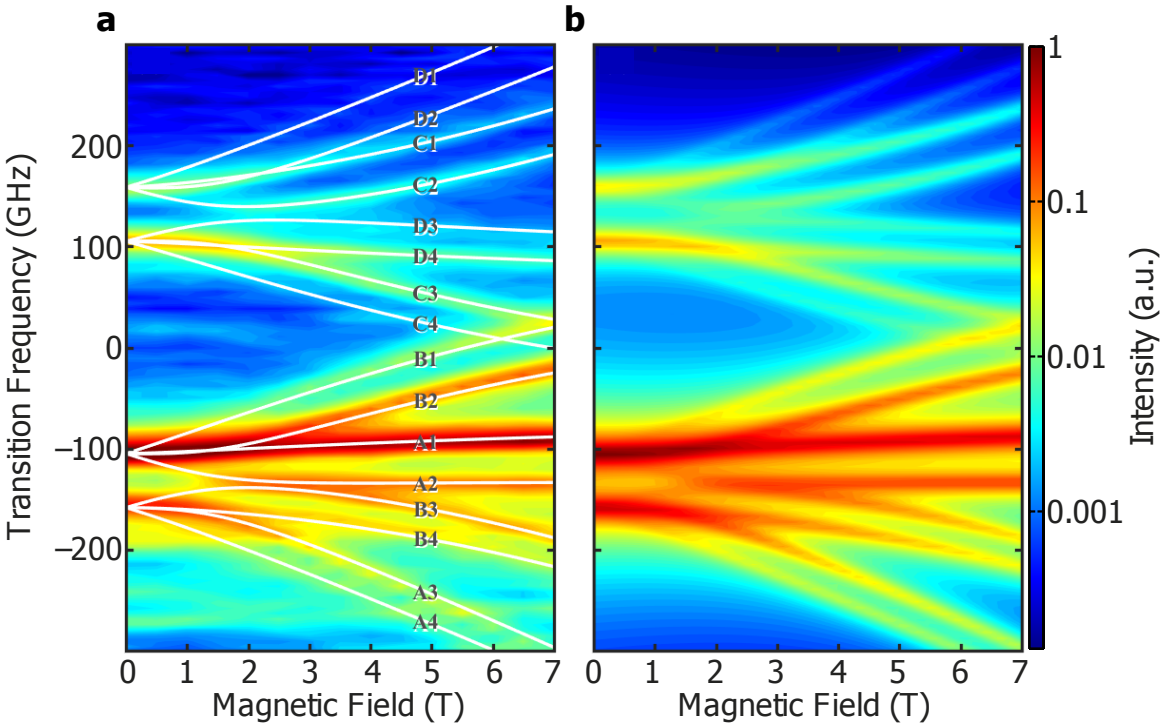

Figure 2.12 Simulation of SiV^- fluorescence spectra for a magnetic field at an angle of 54.7° to the SiV axis. (a) Experimental magnetic field dependence of the fluorescence spectra of the SiV^- ensemble (as shown in Fig. 2.2) with simulated transition energies superimposed as white curves. Simulated transitions are labelled according to their excited and ground state levels, as seen in Fig. 2.13. (b) Fully simulated fluorescence spectra as a function of the applied magnetic field.

2.5 Influence of the magnetic field orientation

The competition between spin-orbit coupling and external magnetic field for determining the effective quantisation axis of the spin has a considerable impact on the optical spectrum of the SiV^- as well as on how optical photons and spin can be interfaced. In order to gain experimental confirmation of this phenomenon, we investigate the influence of the orientation of the magnetic field on the fluorescence spectrum of the SiV^-, in particular when aligned with different crystallographic axes, as labelled in Fig. 2.15. The following experiment has been performed with assistance from Tillman Godde in the laboratory of Prof. Alexander Tartakovskii (University of Sheffield).

We study a single SiV^- centre in a high-purity ($[N]_s^0 < 5\,\text{ppb}$, $[B] < 1\,\text{ppb}$) diamond produced by chemical vapour deposition (electronic grade from Element Six) with a [001] surface orientation. The sample is at a temperature of 4 K in a helium bath cryostat equipped with two orthogonal superconducting coils allowing to apply a

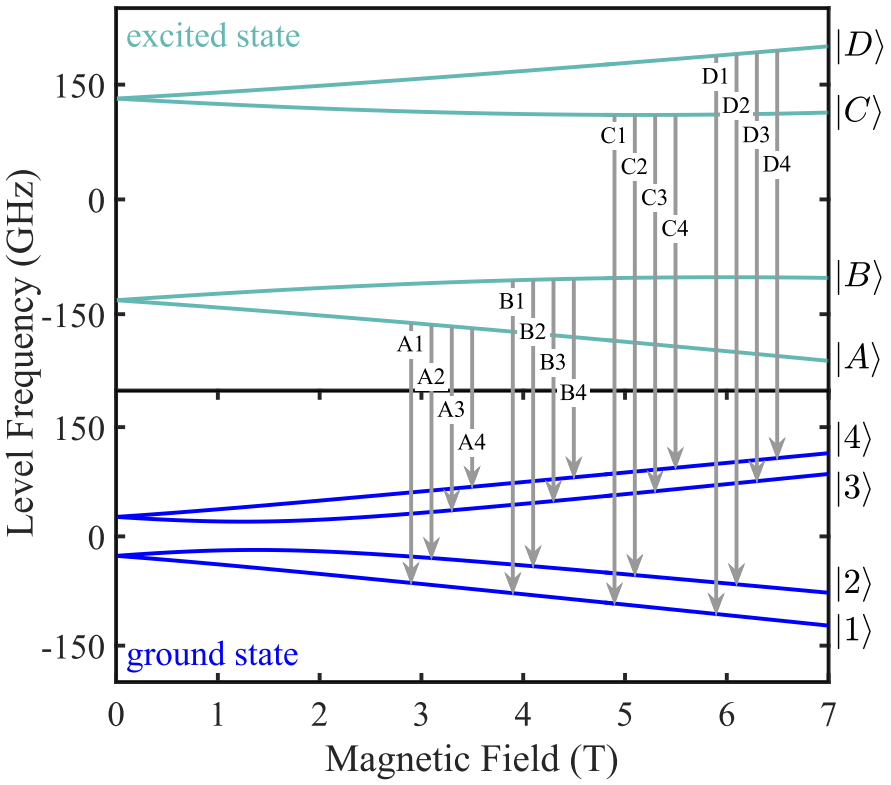

Figure 2.13 Simulation of the magnetic field dependence of SiV^- energy levels for a magnetic field at an angle of 54.7° to the SiV axis, as extracted from the fit to the experimental spectra.

magnetic field of up to 4.5 T at any angle within a vertical plane. The optical part of the setup is similar to that described in Section 2.1.

We first measure the magnetic field dependence of the fluorescence spectrum for a magnetic field aligned along the [001] crystallographic direction and thus making an angle of 54.7° to the SiV axis, as was the case for the SiV^- ensemble in Section 2.2. Figure 2.16 diplays the experimentally obtained variation of the optical transitions with magnetic field strength (Fig. 2.16a), alongside the simulated transitions superimposed to the experimental spectra (Fig. 2.16b) and the fully simulated spectra (Fig. 2.16c) using the group theoretical model described above. From the fit of the model to the experimental spectra, we determine the parameters of the Hamiltonians as well as the magnetic field dependence of the eigenstates and energy levels of the SiV^-, as diplayed in Fig. 2.17. We notice that the response to the applied magnetic field is very similar to the one measured with the ensemble, although not all transitions are visible, most likely due to the overall low counts from the single SiV^- compared to the ensemble.

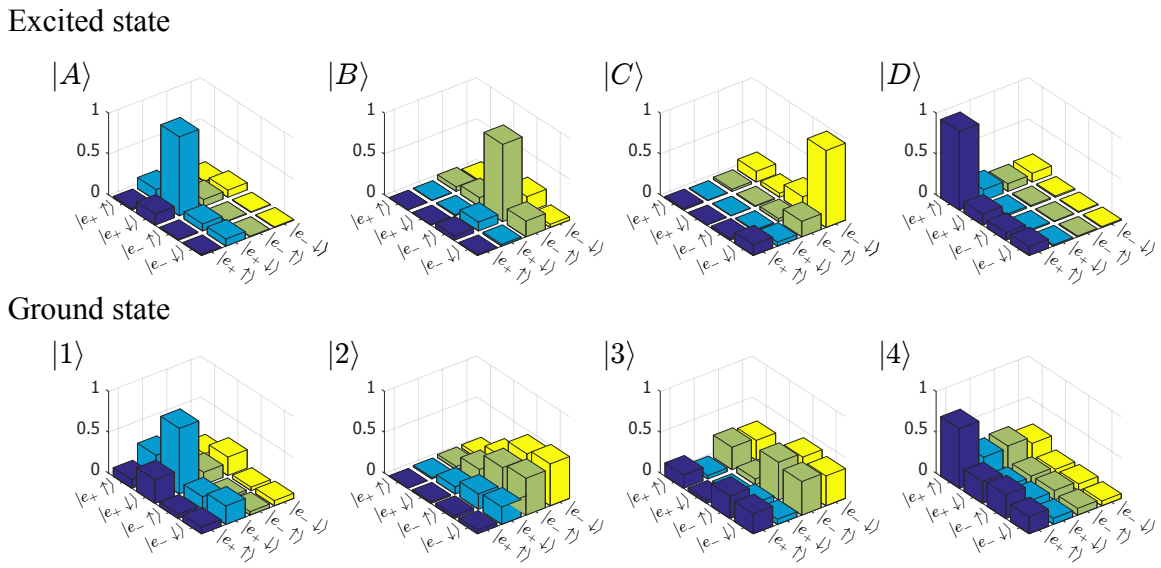

Figure 2.14 Simulated tomography of the SiV^- eigenstates at 4 T for an angle of 54.7° between the magnetic field and the SiV axis. For each state, labelled as in Fig. 2.13, the histograms represent the norms of the components of its density matrix expressed in the eigenbasis of the spin-orbit coupling $\{|e_+\uparrow\rangle, |e_+\downarrow\rangle, |e_-\uparrow\rangle, |e_-\downarrow\rangle\}$.

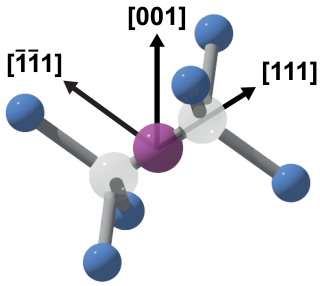

Figure 2.15 Schematic of the SiV and the main crystallographic axes.

In order to investigate the correlation between spin state and optical selection rules, we extract from the simulated eigenstates their spin projection in the following way. The eigenstates of the SiV^- determined through the group theoretical model, are of the form $\left|\Psi_{g/u}\right\rangle = \alpha\left|e_{g/u,+}\uparrow\right\rangle + \beta\left|e_{g/u,+}\downarrow\right\rangle + \gamma\left|e_{g/u,-}\uparrow\right\rangle + \delta\left|e_{g/u,-}\downarrow\right\rangle$, where α, β, γ and δ are complex numbers, $e_\pm$ refer to orbital components of the spin-orbit basis states and $\uparrow$,$\downarrow$ to their spin S_z component with the quantisation axis taken along the axis of the SiV centre. The subscripts g and u correspond to ground and excited states respectively. We extract the spin S_z component of the eigenstates of the SiV^- by using

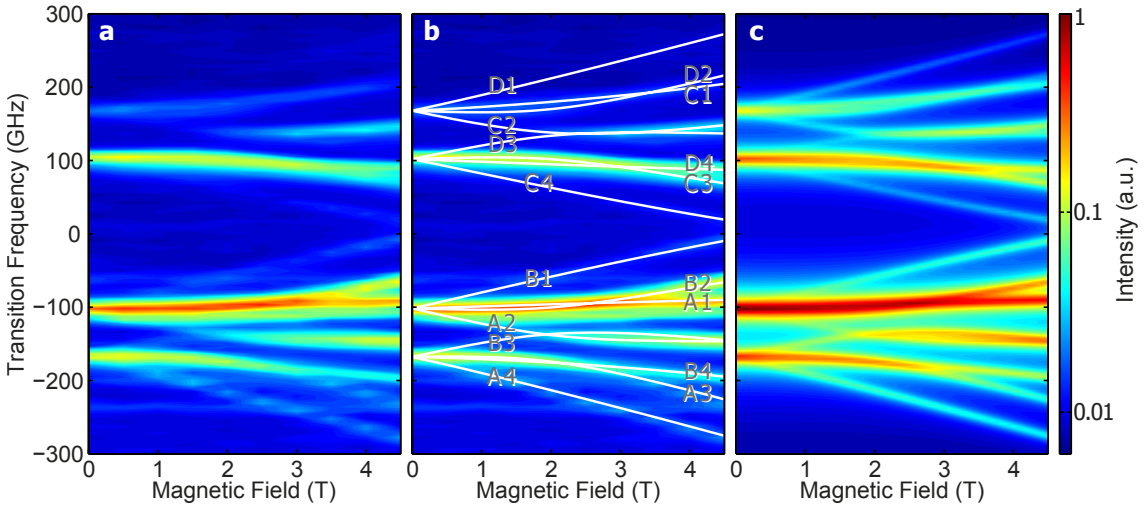

Figure 2.16 Magnetic field dependence of the fluorescence spectra of a single SiV^- centre for a magnetic field along the [001] crystallographic axis, corresponding to an angle of 54.7° to the SiV axis. (a) Experimental spectra alone, (b) overlapped with simulated transitions (white lines). (c) Fully simulated spectra as a function of magnetic field.

the projector $\mathcal{P} = |\uparrow\rangle\langle\uparrow| + |\downarrow\rangle\langle\downarrow|$, which projects the eigenstate onto the spin subspace:

$$\mathcal{P}\left|\Psi_{g/e}\right\rangle = (\alpha+\gamma)\,|\uparrow\rangle + (\beta+\delta)\,|\downarrow\rangle = c_\uparrow\,|\uparrow\rangle + c_\downarrow\,|\downarrow\rangle \tag{2.7}$$

We can rewrite it as $\mathcal{P}\left|\Psi_{g/e}\right\rangle = \cos(\theta/2)\,|\uparrow\rangle + e^{i\phi}\sin(\theta/2)\,|\downarrow\rangle$ to represent this spin as a vector on a Bloch sphere [1, 154], where the North pole is $|\uparrow\rangle$, the South pole is $|\downarrow\rangle$, and θ with $0 \leq \theta \leq \pi$ and ϕ with $0 \leq \phi < 2\pi$ are the colatitude (angle from the North pole) and the longitude respectively. For convenience, we represent the spin projection of each eigenstate using only the colatitude, i.e. the angle between the spin and the z-axis (SiV axis), as illustrated in Fig. 2.17. We can see that the spin in the excited states remains roughly aligned with the SiV axis, whereas in the ground states, it is much more tilted away from it. This, as mentioned earlier, is the result of the competition between the spin-orbit along the SiV axis and the magnetic field to determine an effective quantisation axis for the spin. The spin-orbit coupling being about five times stronger in the excited state remains dominant, while the impact of the B_x and B_y components of the external magnetic field is in comparison stronger in the ground state and "tilts" the spin away from the SiV axis. Consequently, the effective spin quantisation axes are different between ground and excited states. In the basis of the ground state spin, the exited state levels are characterised by superpositions of

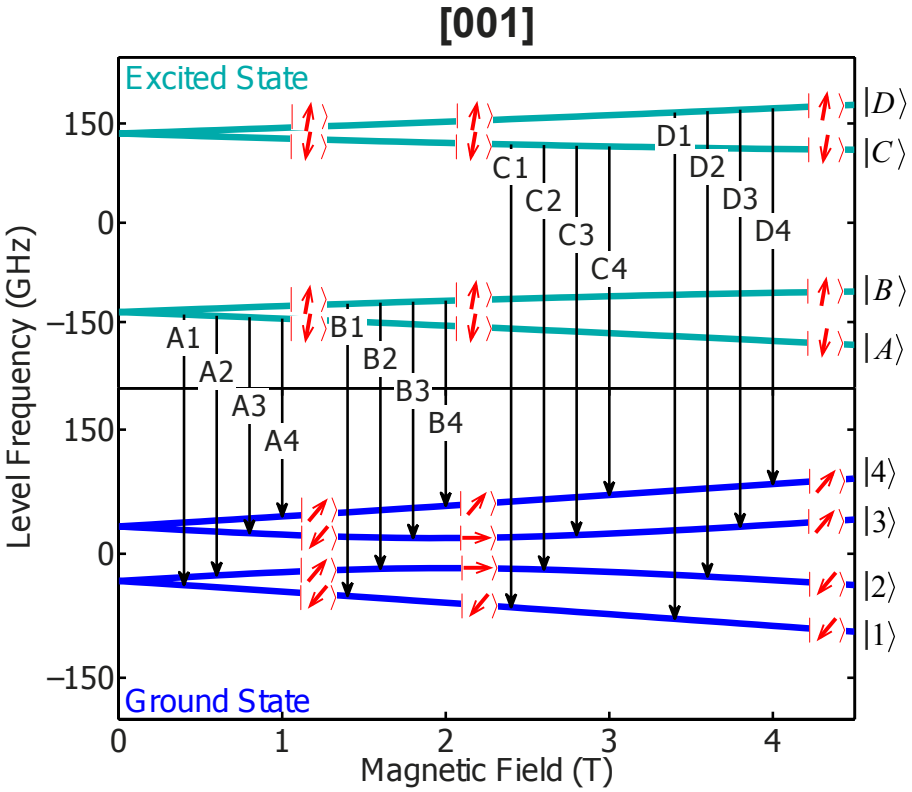

Figure 2.17 Magnetic field dependence of the energy levels for a magnetic field along the [001] crystallographic axis (54.7° with the SiV axis), corresponding to the spectra in Fig. 2.16. Optical transitions are represented as vertical black arrows. The spin projections of each level is illustrated as red arrows, as described in the text. For clarity, we do not tilt the spin arrows proportionnally to the applied magnetic field.

spin, and inversely in the basis of the excited state spin. There can thus be dipolar electric transitions between all the levels. It is worth noting that the avoided crossing between levels $|2\rangle$ and $|3\rangle$ is caused by the components of the magnetic field which are not aligned with the SiV axis, namely B_x and B_y.

We now repeat the same experiment for a magnetic field along the [111] crystallographic direction and thus aligned with the SiV axis. The experimental and simulated spectra are displayed in Fig. 2.18. We highlight the fact that in the simulation, only the angle of the magnetic field was modified, while all the other parameters were left unchanged. The experimental spectrum (Fig. 2.18a) shows only few transitions with little dependence on magnetic field. From the simulated transitions (Fig. 2.18b), it appears that several transitions, such as A4 or B1, are not visible experimentally. When traced back to the energy levels, as depicted in Fig. 2.19, we notice that those transitions

occur between states of opposite spin projections. Indeed, due to the alignment of the magnetic field with the SiV axis, the spin quantisation axis is the same in the ground and excited states, along the SiV axis. Dipolar electric transitions are thus only allowed between states with the same spin orientations, the others being forbidden. In this experiment, above 2 T, some normally forbidden transitions, such as B2 and C3, are visible, due to a slight misalignment of the magnetic field by approximately 10°.

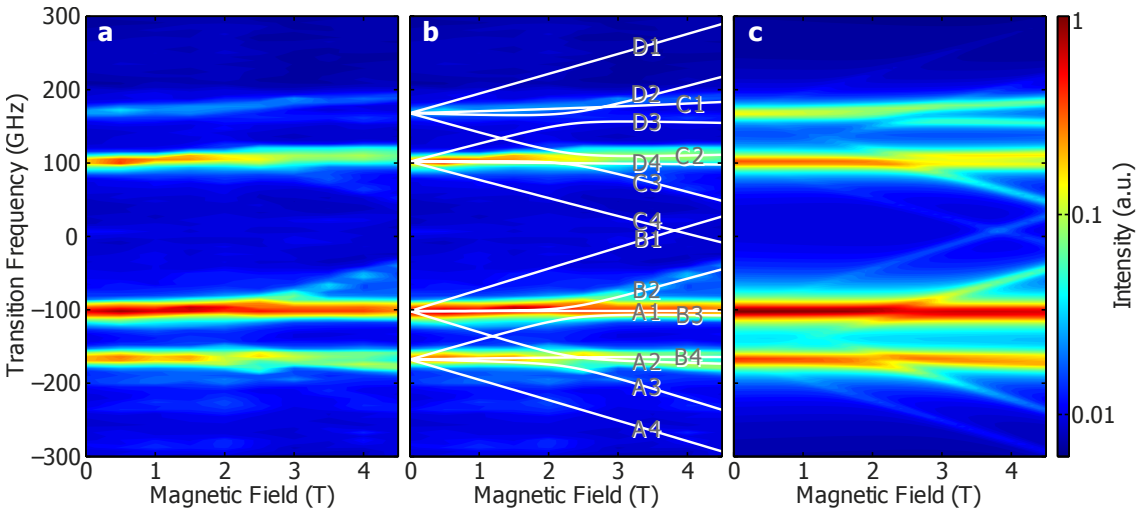

Figure 2.18 Magnetic field dependence of the fluorescence spectra of a single SiV^- centre for a magnetic field close to alignment with the SiV axis ([111] crystallographic axis). (a) Experimental spectra alone, (b) overlapped with simulated transitions (white lines). (c) Fully simulated spectra as a function of magnetic field. An angle of 10° between magnetic field and SiV^- axes fits best the experimental data.

Finally, we apply the magnetic field along the $[\bar{1}\bar{1}1]$ axis, thus making an angle of 109.5° to the SiV axis. Figure 2.20 displays the experimental and simulated spectra and Fig. 2.21 the corresponding energy levels. In this configuration, the magnetic field has a large transverse component with respect to the SiV axis. Hence the spin projections of the SiV^- states are even more tilted than for a [001]-orientation and the difference in quantisation axes between ground and excited states is increased. The result of this is that the state selectivity of dipolar electric transitions is further reduced and transitions have more similar intensities, as can be seen by comparing Fig. 2.16c and Fig. 2.20c.

In conclusion, we verify experimentally the validity of the group theoretical model. In particular, we confirm the role of the spin-orbit coupling as an inherent quantisation axis for the spin and its competition with the external magnetic field to fix effective

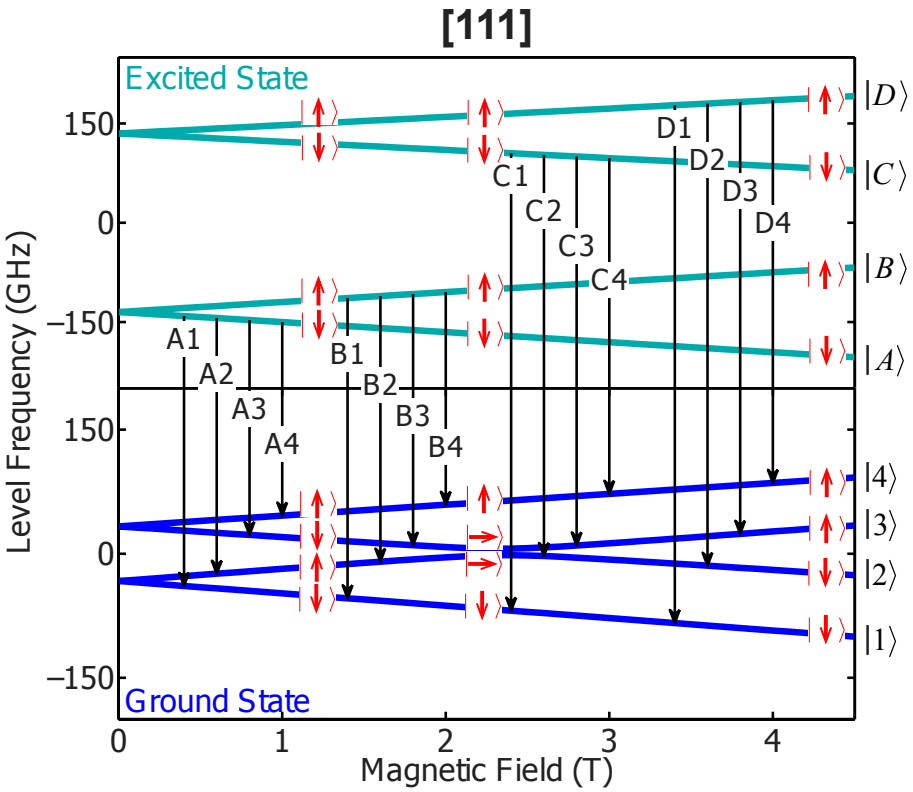

Figure 2.19 Magnetic field dependence of the energy levels for a magnetic field at an angle of 10° to the [111] crystallographic axis, corresponding to the spectra in Fig. 2.18. Optical transitions are represented as vertical black arrows. The spin projections of each level is illustrated as red arrows, as described in the text.

spin quantisation axes in the ground and excited states. The consequences for the optical transitions is their relative intensity dependence upon magnetic field orientation. To summarise this point, we simulate the evolution of optical transitions as a function of the magnetic field angle in Fig. 2.22 for two values of the magnetic field. The most striking feature is the disappearance of several optical transitions as the angle goes to zero. These transitions would occur between states of different spin orientations along the same quantisation axis and are therefore forbidden.

2.6 Conclusion

We have shown that, in the presence of an external magnetic field, the four transitions forming the SiV^- zero-phonon line further split, leading to a total of 16 transitions. This splitting, although compatible with an electronic spin $S = 1/2$, is not a sufficient proof.

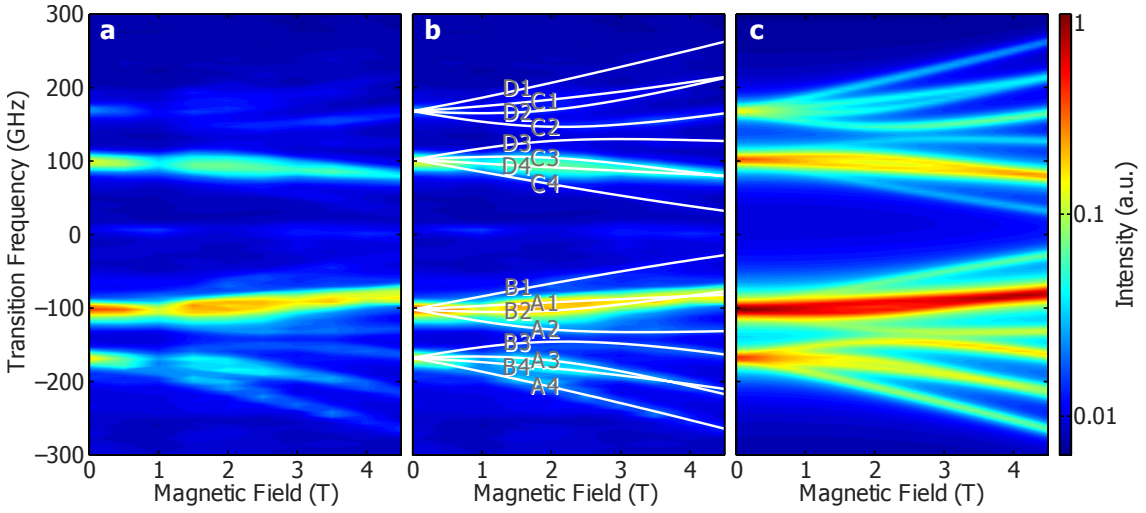

Figure 2.20 Magnetic field dependence of the fluorescence spectra of a single SiV^- centre for a magnetic field along the $[\bar{1}\bar{1}1]$ crystallographic axis, corresponding to an angle of 109.5° to the SiV axis. (a) Experimental spectra alone, (b) overlapped with simulated transitions (white lines). (c) Fully simulated spectra as a function of magnetic field.

Through the implementation of resonant excitation, we have selectively populated excited state levels. The subsequent fluorescence displays clear optical selection rules, evidencing a spin-selective thermalisation among the excited state levels and thus confirming that the SiV^- centre possesses a spin $S = 1/2$. However, the presence of optical transitions between levels of *a priori* opposite spin orientations has led to the necessity to develop a model of the system. A model based on group theory not only allows one to reproduce the magnetic field dependence of the optical spectra measured experimentally, but also suggests a peculiar form of the spin-orbit coupling. Indeed, in the case of the SiV^-, the spin-orbit coupling provides an inherent quantisation axis for the spin along the SiV axis. This results in spin mixing when a magnetic field is applied. This mixing can be thought of as different effective spin quantisation axes between ground and excited states, due to different strengths of spin-orbit coupling. Exploring the dependence of the fluorescence spectra on the angle of the applied magnetic field, we have confirmed this phenomenon and shown that when the magnetic field is aligned with the SiV axis, only half of the transitions are optically allowed and correspond to cycling transitions, whereas a large angle between magnetic field and SiV axis leads to all possible transitions being allowed.

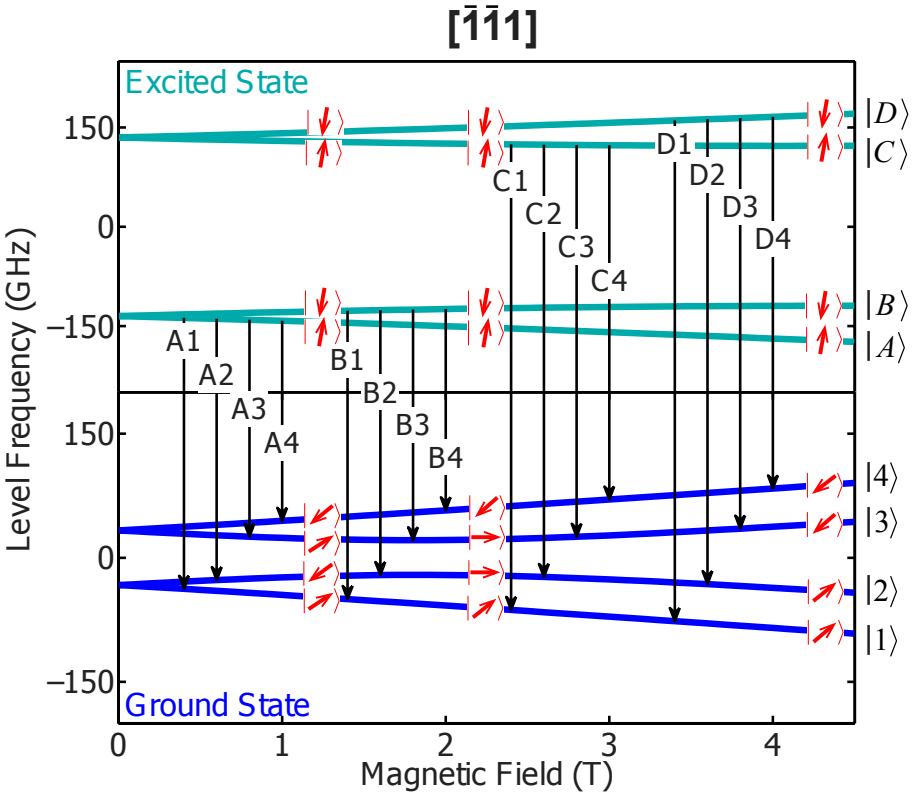

Figure 2.21 Magnetic field dependence of the energy levels for a magnetic field along the [$\bar{1}\bar{1}$1] crystallographic axis (109.5° with the SiV axis), corresponding to the spectra in Fig. 2.20. Optical transitions are represented as vertical black arrows. The spin projections of each level is illustrated as red arrows, as described in the text. For clarity, we do not tilt the spin arrows proportionnally to the applied magnetic field.

Those results shed light on the physics of the SiV^- centre, which is essential for understanding and taking advantage of its properties. From the point of view of quantum information processing, the presence of an optically accessible spin which can be used as a quantum bit makes the SiV^- centre a promising building block for a quantum network. This optical accessibility is indeed crucial for transfer of quantum information between stationary qubits (spins) processing and storing this information and flying qubits (photons) transporting it with minimum losses between processing nodes. Next steps are then to evaluate whether this spin is not only accessible but also controllable by light and evaluate for how long it could store and process information.

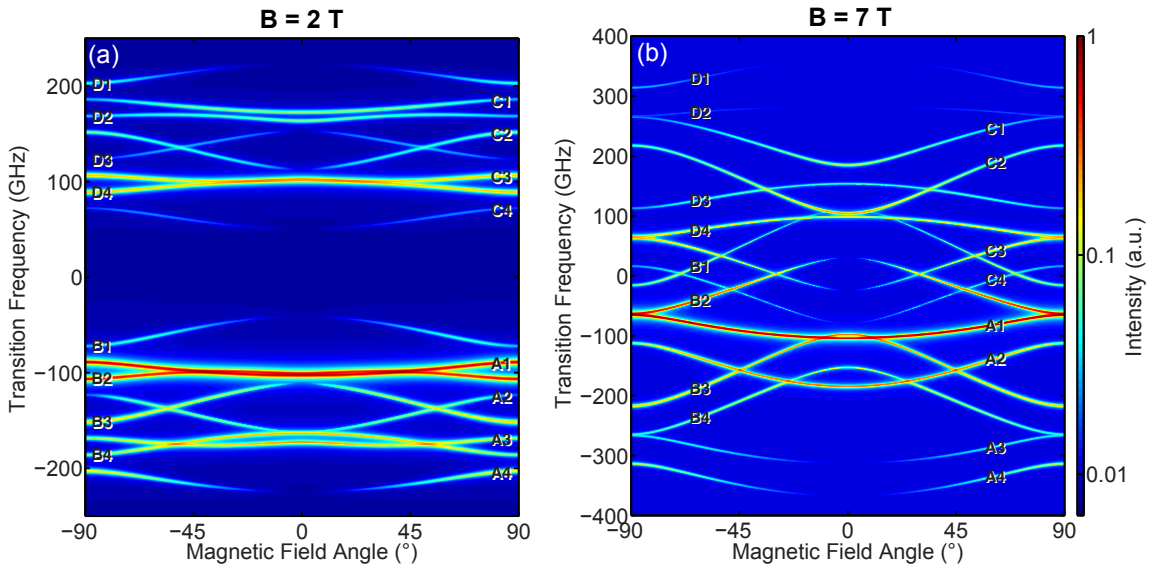

Figure 2.22 Simulated fluorescence spectra of the SiV^- as a function of the angle between the magnetic field and the symmetry axis of the SiV at (a) 2 T and (b) 7 T. When the magnetic field is not aligned with the SiV axis, "spin-forbidden" transitions A2, A4, B1, B3, C2, C4, D1 and D3 become visible. In D_{3d} symmetry the Zeeman perturbation of the SiV^- energy levels is cylindrically symmetric and therefore only depends on the azimuthal angle of the magnetic field with respect to the high symmetry axis of the emitter.

Chapter 3

Coherent population trapping of a single SiV^- centre

The evidence that the SiV^- possesses a spin makes this colour centre a candidate for quantum information processing as this spin can be used as a quantum bit. The next question is then that of the coherence properties of this spin, as this will shape its usability for quantum information processing. Furthermore, the direct optical access to the spin degree of freedom is also promising for combining spin and desirable optical properties. This aspect thus needs further investigation as the ultimate goal is to be able to transfer information from photon to spin and inversely with a view to using the SiV^- as a spin-photon interface in a quantum network.

In this chapter, we build upon resonant excitation of the SiV^- centre to achieve coherent population trapping. This technique not only addresses the potential for all-optical control of the spin, but also provides a measurement of the spin coherence. Those results were obtained with Jonas N. Becker, with assistance from Carsten Schulte, Carsten Arend and Christian Hepp, and have been published in Ref. [145].

3.1 Theoretical background

Coherent population trapping (CPT) is a phenomenon based on the coherent interaction between light and the energy levels of a quantum system [155]. We introduce here the fundamental concepts of this phenomenon as well as how to use CPT to extract some coherence properties of the quantum system.

3.1.1 Coherent interaction of a two-level atom and an electromagnetic field

Let us consider an atom with ground and excited states $|g\rangle$ and $|e\rangle$ (of energies E_{gr} and E_{ex} respectively) and a monochromatic electromagnetic field. In the dipole approximation, the interaction Hamiltonian between the driving field and the atom is that of an electric dipole $\vec{d} = -e\vec{r}$ ($-e$ is the electron charge and $\vec{r}$ is the position of the electron with respect to the centre of mass of the atom) in the electric field $\vec{\mathcal{E}} = \vec{\mathcal{E}}_0 \cos(\omega t)$ oscillating at the frequency ω. This interaction is of the form $\mathcal{H}_{int} = -\vec{d} \cdot \vec{\mathcal{E}}$ [156, 154]. The original states $|g\rangle$ and $|e\rangle$ are no longer stationary and the system evolves in time as:

$$\Psi(t) = c_g(t)\,|g\rangle + c_e(t)\,|e\rangle\, e^{-i\omega_0 t} \tag{3.1}$$

where $\omega_0 = (E_{ex} - E_{gr})/\hbar$, and the coefficients c_g and c_e vary in time and are such that $|c_g|^2 + |c_e|^2 = 1$. In the rotating-wave approximation, the time-dependent Schrödinger equation yields [156, 154]:

$$i\frac{\mathrm{d}c_g}{\mathrm{d}t} = c_e \exp\{i(\omega - \omega_0)t\}\,\frac{\Omega}{2} \tag{3.2}$$

$$i\frac{\mathrm{d}c_e}{\mathrm{d}t} = c_g \exp\{-i(\omega - \omega_0)t\}\,\frac{\Omega^*}{2} \tag{3.3}$$

where $\Omega = \langle g|e\vec{r} \cdot \vec{E}_0|e\rangle\,/\hbar$ is the Rabi frequency quantifying how strongly the transition dipole of the atom and the electric field couple. By solving the time-dependent Schrödinger equation with the initial condition $c_g(0) = 1$ and $c_e(0) = 0$, we obtain that the probability of being in the excited state is:

$$|c_e|^2 = \frac{\Omega^2}{\Omega^2 + \delta^2} \sin^2\left(\frac{\sqrt{\Omega^2 + \delta^2}\,t}{2}\right) \tag{3.4}$$

with $\delta = \omega - \omega_0$ is the frequency detuning between the electromagnetic wave and the atomic transition. When in resonance ($\delta = 0$), we obtain:

$$|c_e|^2 = \sin^2\left(\frac{\Omega t}{2}\right) \tag{3.5}$$

The population oscillates between the ground and the excited state. Starting from the ground state, the population is fully transferred to the excited state for an electromagnetic wave of duration Δt such that $\Omega \Delta t = \pi$. Such an electromagnetic pulse is thus

called a π-pulse and inverts the population from one state to the other. Similarly, a $\pi/2$-pulse such that $\Omega\Delta t = \pi/2$ creates an equal superposition between $|g\rangle$ and $|e\rangle$.

3.1.2 Theory of coherent population trapping

Let us now consider an atom-like system with three energy levels: two ground states $|1\rangle$, $|2\rangle$ and one excited state $|3\rangle$ (at the energies E_1, E_2 and E_3 respectively) forming a Λ-type scheme and two electromagnetic fields of frequencies ω_1 and ω_2 driving transitions between $|1\rangle$ and $|3\rangle$ and between $|2\rangle$ and $|3\rangle$ respectively, as illustrated in Fig. 3.1.

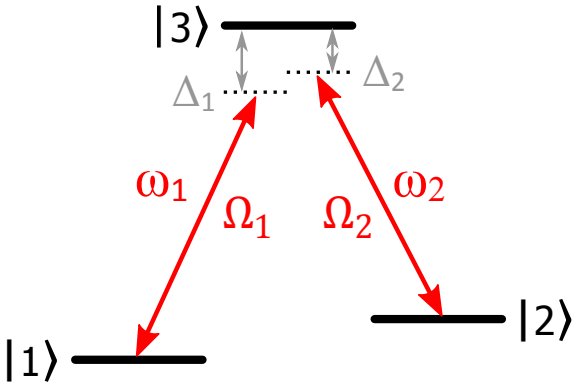

Figure 3.1 Representation of a Λ-scheme for CPT. Two electromagnetic fields of frequencies ω_1 and ω_2 drive the transition between $|1\rangle$ and $|3\rangle$ with a Rabi frequency Ω_1 and between $|2\rangle$ and $|3\rangle$ with a Rabi frequency Ω_2 respectively. Δ_1 and Δ_2 correspond to the detunings of the respective electromagnetic fields.

Using the same approach as for the two-level atom, the driving field ω_1 generates oscillations between states $|1\rangle$ and $|3\rangle$ with a Rabi frequency Ω_1 and the driving field ω_2 generates oscillations between states $|2\rangle$ and $|3\rangle$ with a Rabi frequency Ω_2. In the basis $\{|1\rangle, |2\rangle, |3\rangle\}$, the matrix of the Hamiltonian for the whole system in the rotating frame (at frequency $(E_1/\hbar) + \omega_1$) can be written as [155]:

$$\mathcal{H}_{\text{int}} = \hbar \begin{pmatrix} 0 & 0 & \Omega_1/2 \\ 0 & -(\Delta_1 - \Delta_2) & \Omega_2/2 \\ \Omega_1/2 & \Omega_2/2 & -\Delta_1 \end{pmatrix} \tag{3.6}$$

where Δ_1 and Δ_2 are the driving field frequency detunings as indicated in Fig. 3.1.

The eigenstates of this Hamiltonian at the two-photon resonance $\Delta_1 = \Delta_2 = \Delta$ are [155]:

$$|B_+\rangle = \sin(\Theta)\sin(\Phi)\,|1\rangle + \cos(\Phi)\,|3\rangle + \cos(\Theta)\sin(\Phi)\,|2\rangle \tag{3.7}$$

$$|B_-\rangle = \sin(\Theta)\cos(\Phi)\,|1\rangle - \sin(\Phi)\,|3\rangle + \cos(\Theta)\cos(\Phi)\,|2\rangle \tag{3.8}$$

$$|D\rangle = \cos(\Theta)\,|1\rangle - \sin(\Theta)\,|2\rangle \tag{3.9}$$

with:

$$\tan(\Theta) = \frac{\Omega_1}{\Omega_2} \tag{3.10}$$

$$\tan(2\Phi) = \frac{\sqrt{\Omega_1^2 + \Omega_2^2}}{\Delta} \tag{3.11}$$

We can see that state $|D\rangle$ corresponds to a superposition of the two ground states only and does not include the excited state. In resonance $\Delta = 0$, it becomes:

$$|D\rangle = \frac{|\Omega_2|}{\sqrt{\Omega_1^2 + \Omega_2^2}}\,|1\rangle - \frac{|\Omega_1|e^{i\phi}}{\sqrt{\Omega_1^2 + \Omega_2^2}}\,|2\rangle \tag{3.12}$$

where ϕ is the relative phase between the two driving fields. In contrast, the two other eigenstates $|B_+\rangle$ and $|B_-\rangle$ have a component with the excited state. As a consequence, $|B_+\rangle$ and $|B_-\rangle$ can be destroyed by spontaneous emission from their excited state component, whereas $|D\rangle$ cannot lead to fluorescence and can thus be called a "dark state", as opposed to the other two "bright states". This system can thus be thought of as a radiative cascade down eigenstates. The cascade gets interrupted when the system falls into state $|D\rangle$ and remains "trapped", a phenomenon analogous to optical pumping and responsible for the term "coherent population trapping". An important point is that the dark state can be destroyed by dephasing between the two ground states, which leads to the restart of the radiative cascade.

This process is most easily observed in the frequency domain. Having the frequency of one of the driving fields fixed, the frequency of the other is scanned. At the two-photon resonance, i.e. when both optical fields have the same detuning from the excited state, the system is pumped into the dark state and the fluorescence intensity displays a dip. The width of the CPT dip is directly proportional to the decay rate out of the dark state, and thus inversely proportional to the dephasing time T_2^* between the two ground states. One can make an analogy between leaving the dark state and

spontaneous emission, whereby the lifetime of the dark state determines the width of the transition in the frequency domain, with the "full width at half maximum" of the CPT dip corresponding to $1/(2\pi T_2^*)$, in the absence of external dephasing mechanisms (which includes being in the limit of zero optical power).

3.2 Experimental conditions

3.2.1 Experimental setup

All the measurements are performed at a temperature of 4 K. The cryogenic setup is the same as that described in Section 2.1 and consists of a helium bath cryostat into which the diamond sample is mounted. A stack of three piezoelectric stages allows us to move the sample with respect to an aspheric lens with NA=0.68 positioned in the cryostat above the sample. A superconducting coil surrounding the sample space allows us to apply a tunable magnetic field from 0 to 7 T. Resonant excitation is performed using two tunable diode lasers (Toptica DL 100 pro design and Toptica DL pro). They are both independently stabilised in frequency through feedback from a wavelength meter (High Finesse WS-U). The optical setup consists of a confocal microscope positioned on top of the cryostat. In detection, fluorescence from the SiV^- is separated from the resonant laser light using a home-built monochromator with a grating of 1600 grooves/mm in "4f" configuration, and sent to an avalanche photodiode (APD). This detection method separates light in frequency instead of polarisation as in Chapter 2. It is more adapted to the simultaneous suppression of two laser fields and is much more resilient to changes of the optical parameters such as laser frequencies and polarisations, but does not allow for detection of photons from resonantly excited transitions. As the dark state depends on the complex Rabi frequencies from both driving fields, the laser intensities are stabilised with acousto-optic modulators (AOM). The relative phase of the two lasers is not stabilised. The two lasers have a mutual coherence of about 5 MHz for integration times between 0.5 s and 8 s typically used during our CPT measurements. The impact of this mutual coherence will be discussed in Section 3.4.

3.2.2 Sample

The sample used for those measurements is a (111)-oriented type IIa high-pressure-high-temperature (HPHT) diamond provided by Dr. Matthew Markham (Element 6).

The sample has been implanted with ^{28}Si by ion implantation at an energy of 900 keV, resulting in an average implantation depth of 500 ± 50 nm as evaluated through a SRIM algorithm [109] (ion implantation performed by Dr. Detlef Rogalla at RUBION, Bochum, Germany). Implantation doses have been varied from 10^9 to 10^{12} ions·cm^{-2}. The sample was subsequently annealed at 1000 °C in vacuum for 3 hours to allow vacancies, both naturally present and implantation-induced, to become mobile and thus form SiV centres or reach the sample surface and be eliminated. This annealing step creates a light graphitisation of the sample surface and thus requires a subsequent oxidation step in air for 1 hour at 460 °C to eliminate the graphite layer. Single SiV^- centres can be found in the 10^9 ions·cm^{-2} region.

Since diamond has a high refractive index of $n = 2.4$, the large index mismatch at the interface with air results in most of the photons emitted in the diamond by an SiV^- centre to undergo total internal reflection. We circumvent this effect by etching hemispherical solid immersion lenses (SIL) into the sample surface. Such structures have previously been reported to increase collection efficiency by a factor 10 [157, 158]. The photons emitted by an SiV^- located at the centre of a SIL reach the SIL surface with an angle of incidence of zero which maximises the probability of transmission. These SILs have been created through focused ion beam milling (FIB) (see Fig. 3.2), where a beam of gallium ions is focused onto the diamond surface to etch it (FIB milling performed by C. Pauly). After the milling step, graphite and gallium residues incorporated into the diamond surface are removed by acid cleaning in a piranha solution of 2/3 sulfuric acid and 1/3 30 % hydrogen peroxide. Each SIL is carved with a radius of 500 nm to match the implantation depth of silicon atoms, as shown in Fig. 3.2b. SILs are arranged in arrays randomly located in the implantation area where single centres could be isolated. SiV^- centres are thus randomly located within the SILs.

3.2.3 Characterisation of the SiV^- centre studied

As the surface of the sample is orthogonal to the <111> crystallographic axis, the optical axis is aligned with the [111] direction. As the optical dipole of the SiV^- is mainly along its symmetry axis, the fluorescence from centres aligned with the external field is not efficiently collected and, as a consequence, those centres are not visible. All the visible emitters thus make an angle of $109.5 \pm 1.0°$ (angle between $[\bar{1}\bar{1}1]$ and [111] directions) to the optical axis and hence to the applied magnetic field. At such an angle, all optical transitions are allowed, as shown in Section 2.5.

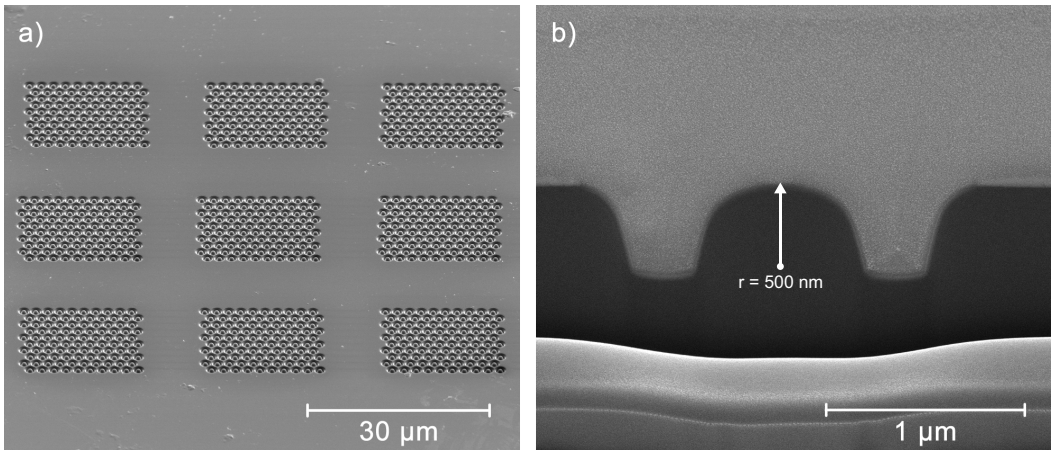

Figure 3.2 Scanning electron microscope (SEM) images of solid immersion lenses (SILs) etched into the diamond surface. (a) Nine arrays of 10×10 SILs have been created using focused ion beam (FIB) milling. (b) The 500 nm radius of the hemispherical SILs matches the implantation depth of the SiV^- centres, each SIL is surrounded by a 300 nm wide trench to avoid light scattering at the edges of the FIB cut.

The SIL arrays are scanned under non-resonant excitation in order to identify bright emitters. The SiV^- centre chosen for this experiment is located at the centre of a SIL (as shown in Fig. 3.3) which makes it almost an order of magnitude brighter than neighbouring centres (up to $3 \cdot 10^5$ counts/s close to saturation under non-resonant excitation).

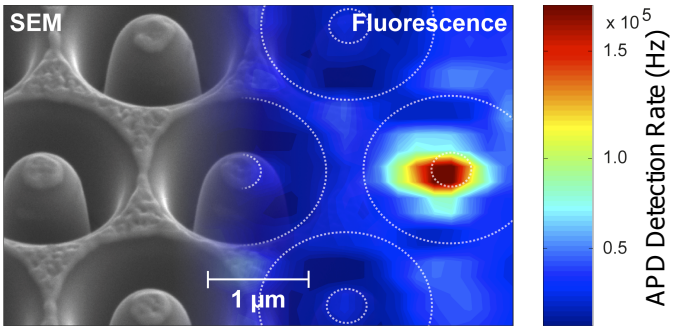

Figure 3.3 SEM image of the solid immersion lens array superimposed with a corresponding fluorescence intensity image (excitation 690 nm, detection 730-750 nm).

We measure the lifetime of the excited state of the centre through a time-correlated single photon counting experiment, as shown in Fig. 3.4. A fit with a single exponential decay gives a value of 1.66 ns. This lifetime is used to determine the transition rates in the master equation model described below in Section 3.4.

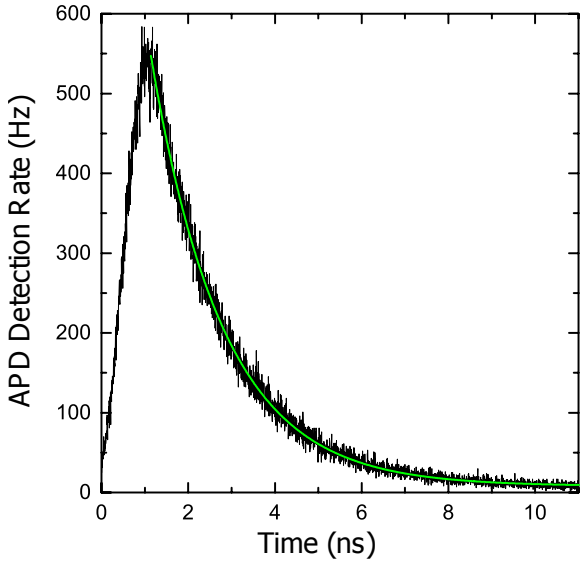

Figure 3.4 Excited state lifetime measured by time-correlated single photon counting on the SiV$^-$ centre studied. The relaxation is fitted using a single exponential giving a decay time of 1.662 ± 0.006 ns.

We characterise the SiV$^-$ centre chosen for this experiment under non-resonant excitation at 660 nm. The evolution of the fluorescence spectra as a function of the applied magnetic field is shown in Fig. 3.5a. Using, the group theoretical model described in Chapter 2 Section 2.4, we fit the evolution of the transitions (see Fig. 3.5b and c) and deduce that of the energy levels, as seen in Fig. 3.6. From the spectrum at 0 T, we can extract that the ground state orbital splitting is about 100 GHz instead of the usual 50 GHz. As will be investigated in Chapter 5 Section 5.3, this is the result of crystal strain, which is most likely induced by the FIB milling.

Sweeping the frequency of a resonant laser over the transition labelled D1 in Fig. 3.5 under a magnetic field of 3 T shows that a second SiV$^-$ centre, dimmer than the other one, is also excited within the lens focal spot, as shown in Fig. 3.7. This second emitter is responsible for the extra faint transitions in Fig.3.5a. The ability to resolve those two emitters is the result of their slightly different strain (approximately 2 % ground state splitting difference).

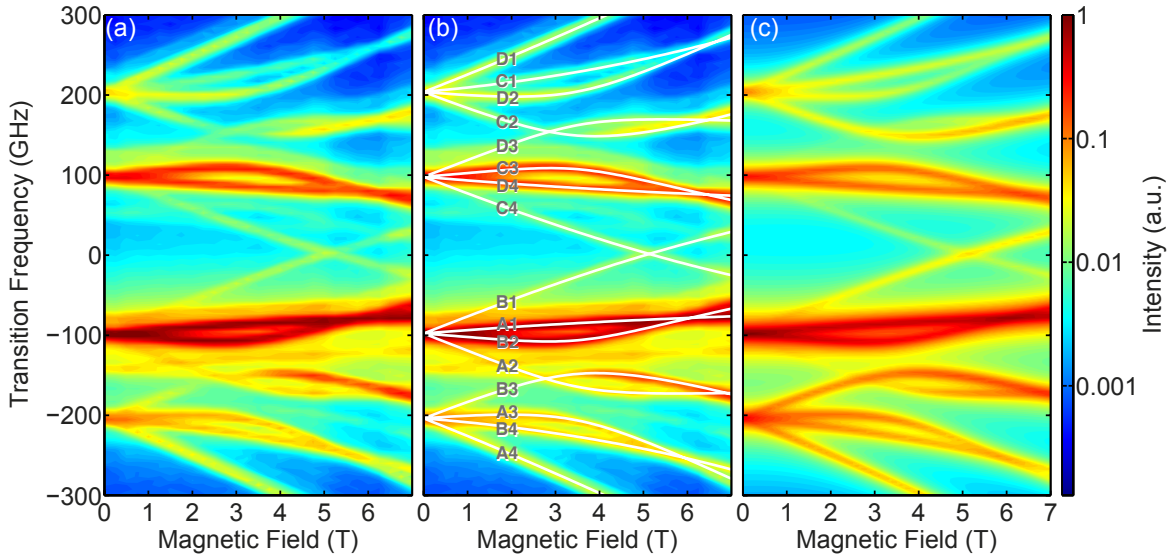

Figure 3.5 Magnetic field dependence of optical transitions. (a) Experimental fluorescence spectra as a function of the applied magnetic field for the SiV^- centre studied. The magnetic field has a relative angle of 109.5° to the SiV^- axis. The colour scale indicates the relative fluorescence intensity in logarithmic scale. (b) Simulated transition wavelengths (white lines) based on the group theoretical model (Section 2.4), superimposed with experimental data. Transition labels correspond to the energy levels displayed in Fig. 3.6. (c) Fully simulated spectra as a function of magnetic field for an angle of 109.5° between magnetic field and SiV^- axes.

3.3 Measurement of coherent population trapping

In order to lift the spin degeneracy, we apply a magnetic field of 0.7 T to the SiV^-. The orientation of the SiV^- studied, which is almost orthogonal to the applied magnetic field (109.5°), results in the spin quantisation axes to be different enough between ground and excited states to make all optical transitions allowed and hence allow for the optical excitation of a Λ-scheme. As we aim to evaluate the spin dephasing time, the generated dark state has to correspond to a superposition of the two possible spin orientations of the SiV^-. We thus resonantly drive the optical transitions labelled D1 and D2 between ground states $|1\rangle$ and $|2\rangle$, which have opposite spin orientations at this magnetic field, and the common excited state $|D\rangle$, as shown in Fig. 3.8. Fluorescence from the SiV^- is then collected from the remaining transitions of the zero-phonon line, as indicated by light grey arrows.

Figure 3.9a displays a CPT scan obtained with one laser being held resonant with transition D1 and the laser resonant with D2 is scanned in frequency. When

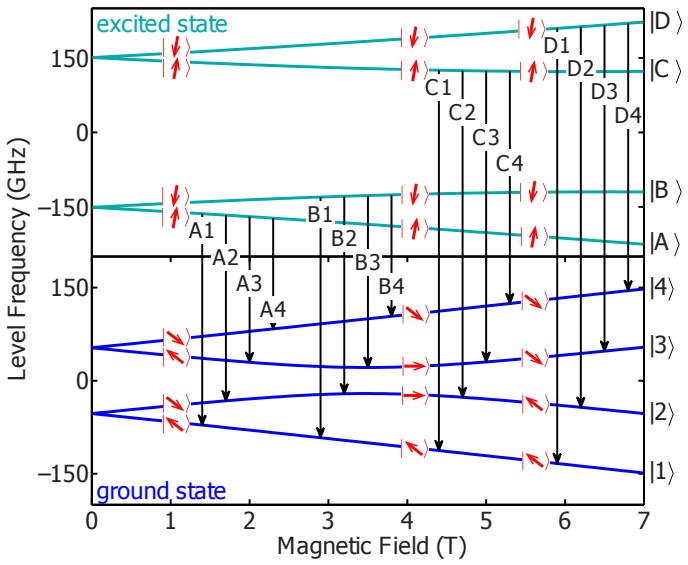

Figure 3.6 Simulated magnetic field dependence of the energy levels of the SiV$^-$ centre for a magnetic field at an angle of 109.5° to the SiV axis. The red arrows indicate the spin states of the levels, black arrows mark the optical transitions corresponding to Fig. 3.5.

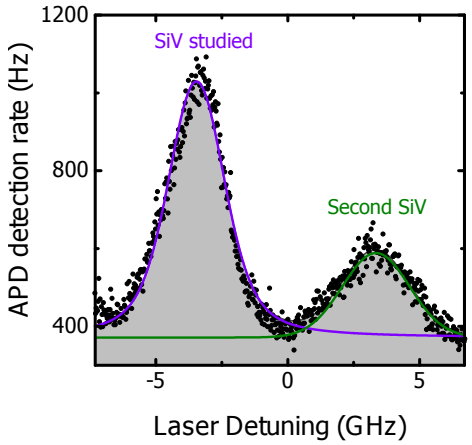

Figure 3.7 Photoluminescence excitation on transition D1 of the SiV$^-$ at 3 T (black dots) reveals the presence of a second emitter (the purple and green curves are Lorentzian fits).

the second laser is brought closer to resonance with D2, the fluorescence from the SiV$^-$ increases until the double resonance is achieved, at which point the fluorescence drops, indicating pumping into the dark state. However, the double resonance is not

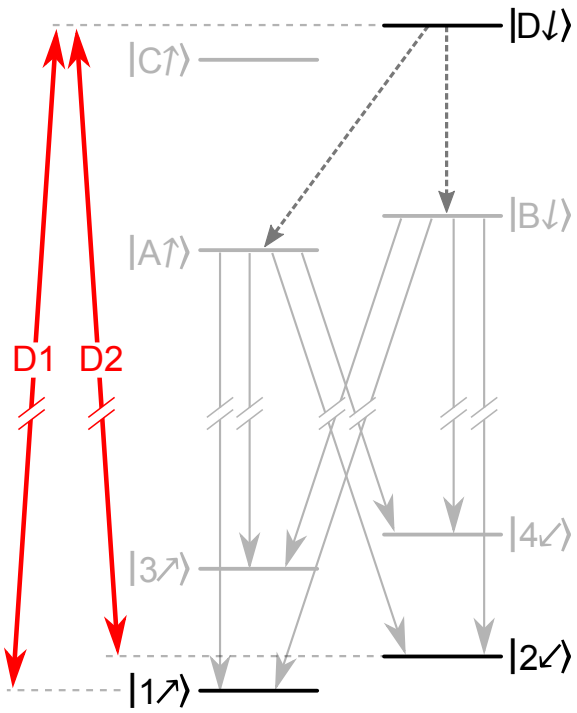

Figure 3.8 Representation of the SiV^- energy levels at non-zero magnetic field with transitions D1 and D2 driven resonantly (red double arrows). The fluorescence is measured on the transitions indicated by grey arrows, following thermalisation among excited state levels (dashed grey arrows). The spin orientations of the levels are illustrated with respect to the spin-orbit quantisation axis which is along the SiV axis, as introduced in Section 2.5.

a necessary condition and CPT is achieved for any two-photon resonance, i.e. when both lasers have the same detuning from the excited state. This can be evidenced in Fig. 3.9b, which is a 2D CPT scan where both laser frequencies are tuned. There, a CPT dip is visible whenever both lasers have the same detuning, resulting in the CPT dips forming a diagonal line.

It is worth noting that, as the relative phase of the two lasers is not fixed, the exact nature of this dark state cannot be known (see equation 3.12). However, this does not impact the coherence time which we will extract from those measurements.

As explained in Section 3.1, the width of the CPT dip is directly correlated with the dephasing time between the two states forming the dark state. However, it also includes the finite mutual coherence of the two lasers and the power broadening described by the Rabi frequencies for the two driven transitions. In order to minimise the impact of power broadening onto the CPT dip width, a CPT scan is measured with both lasers

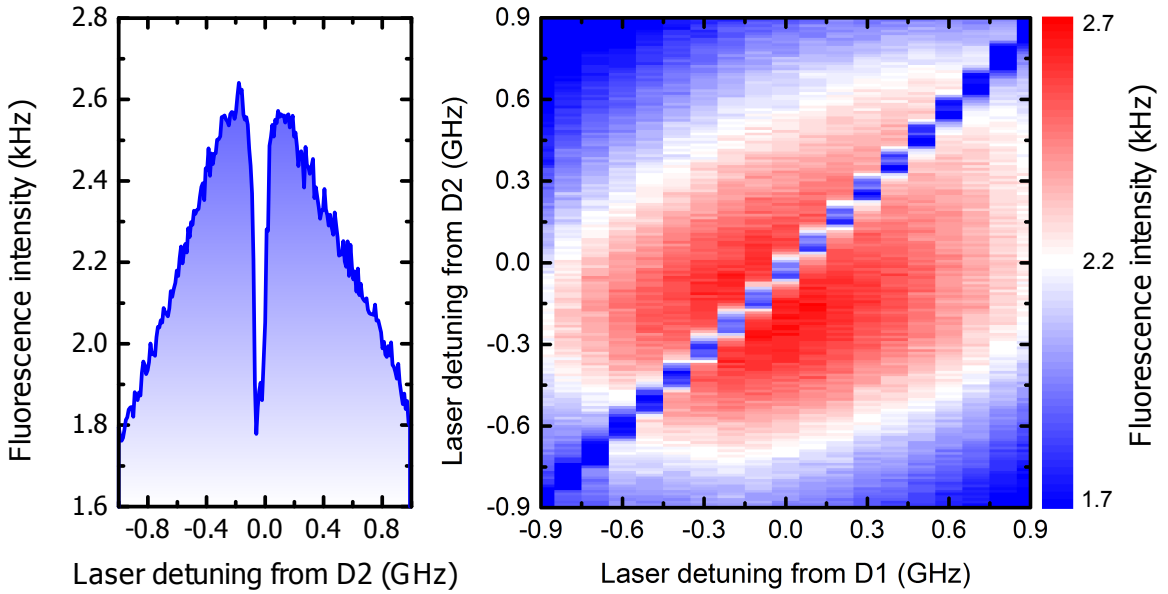

Figure 3.9 CPT scans at 0.7 T. (a) SiV$^-$ fluorescence intensity recorded as the frequency of one laser is scanned over transition D2 and the other laser is resonant with transition D1. (b) Same for different detunings from transition D1 (fluorescence intensity is colour-coded as indicated on the scale bar). Laser powers are equal to approximately four times and seven times the saturation powers for transitions D2 and D1 respectively. The CPT dip from the second SiV$^-$ is too close to the main CPT dip to be resolved at those laser powers.

kept at as low excitation powers as possible (equal to saturation power for the D1 transition and half the saturation power for D2) and is diplayed in Fig. 3.10. Using a Lorentzian fit, the full width at half maximum of the CPT dip under these conditions is 11 ± 1 MHz. A modelling of the CPT signal is necessary to separate the different contributions to the dip width and extract the spin dephasing time.

3.4 Estimation of the electron spin dephasing time

In order to fit the CPT curve and determine the spin dephasing time, we simulate the dynamics of the SiV$^-$ centre through a theoretical model based on optical Bloch equations. The energy levels of the SiV$^-$ are reduced to an open Λ-system including two ground states labelled 1 and 3, an excited state 2 and an auxiliary state 4, as shown in Fig. 3.11. This labelling is not to be confused with that of the full level diagram of the SiV$^-$. Level 1 corresponds to state $|2\rangle$ of the SiV$^-$ energy level scheme, level 3 to $|1\rangle$, and level 2 to $|D\rangle$. The auxiliary level 4 is used to model additional

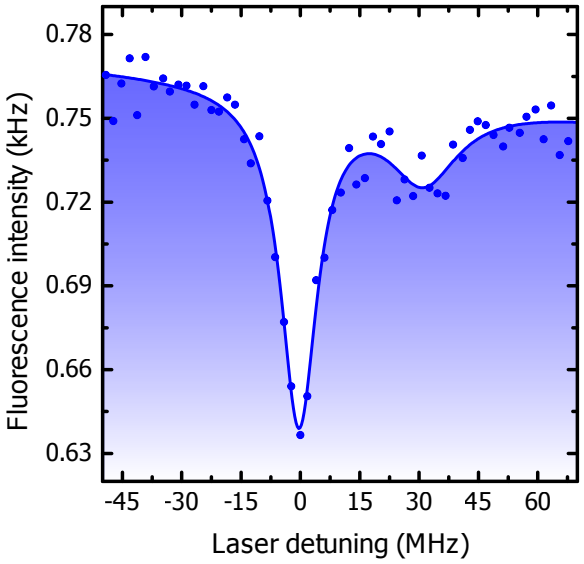

Figure 3.10 CPT scan at 0.7 T at low driving powers (0.33 µW each, corresponding to the saturation power for the D1 transition and half the saturation power for D2) yielding a dip full width at half maximum of 11 ± 1 MHz . The smaller CPT dip corresponds to the second SiV^- centre.

decay channels involving excited and ground states of the SiV^- which are not part of the Λ-system.

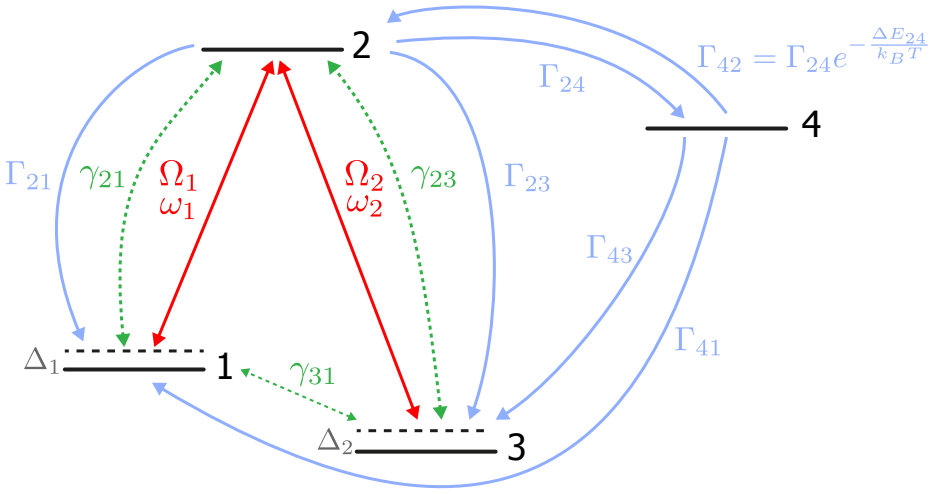

Figure 3.11 Level scheme and corresponding transition rates employed for the master equation model. Red double arrows indicate driving fields at frequencies ω_i and detunings Δ_i, leading to Rabi frequencies Ω_i. Decay (Γ_{ij}) and dephasing (γ_{ij}) processes are represented by blue and green double arrows, respectively.

The Λ-system is driven between the two ground states 1 and 3 and their common excited state 2. The driving field between levels 3 and 2, corresponding to transitions D1, is held in resonance and labelled the pump field. The second driving field between levels 1 and 2, corresponding to transition D2, is scanned in frequency and termed the probe field. The Hamiltonian $\mathcal{H}_{\text{int}}$ of this effective four-level system in the rotating frame, where we apply the rotating-wave approximation, can be written as [159, 160]:

$$\mathcal{H}_{\text{int}} = \hbar \begin{pmatrix} 0 & \frac{\Omega_1}{2} & 0 & 0 \\ \frac{\Omega_1}{2} & \Delta_1 & \frac{\Omega_2}{2} & 0 \\ 0 & \frac{\Omega_2}{2} & \Delta_1 - \Delta_2 & 0 \\ 0 & 0 & 0 & 0 \end{pmatrix} \tag{3.13}$$

with Ω_2 and Ω_1 being respectively the pump and probe laser Rabi frequencies (transitions D1 and D2 respectively) and the corresponding laser detunings:

$$\Delta_1 = \omega_{D2} - \omega_1 \tag{3.14a}$$

$$\Delta_2 = \omega_{D1} - \omega_2 \tag{3.14b}$$

for the probe and pump transitions respectively. The dynamics of the system are governed by the following master equation in Lindblad form [161]:

$$\frac{\mathrm{d}\rho}{\mathrm{d}t} = \frac{i}{\hbar}[\rho, \mathcal{H}_{\text{int}}] + \mathcal{L}(\rho) + \mathcal{D}(\rho) + \mathcal{W}(\rho). \tag{3.15}$$

with the density matrix ρ and the Lindblad superoperator $\mathcal{L}(\rho)$ describing spontaneous emission processes. The matrix $\mathcal{D}(\rho)$ is used to describe additional dephasing processes and $\mathcal{W}(\rho)$ describes the coherence properties of the lasers. Spontaneous emission processes are taken into account by coupling the SiV^- to a reservoir into which photons can be emitted, leading to a relaxation of the system. This is modelled using the Lindblad superoperator:

$$\mathcal{L}(\rho) = \sum \mathcal{L}_{ij}(\rho) = -\frac{1}{2}\sum (C_{ij}^\dagger C_{ij}\rho + \rho C_{ij}^\dagger C_{ij}) + \sum C_{ij}\rho C_{ij}^\dagger \tag{3.16}$$

with the collapse operators:

$$C_{ij} = \sqrt{\Gamma_{ij}}\,|j\rangle\langle i| \tag{3.17}$$

defining a relaxation from state $|i\rangle$ to state $|j\rangle$. The obtained matrices for the Lindblad operators $\mathcal{L}_{ij}$ of the individual decays from $|i\rangle$ to $|i\rangle$ are:

$$\mathcal{L}_{21}(\rho) = \begin{pmatrix} \Gamma_{21}\rho_{22} & -\frac{\Gamma_{21}}{2}\rho_{12} & 0 & 0 \\ -\frac{\Gamma_{21}}{2}\rho_{21} & -\Gamma_{21}\rho_{22} & -\frac{\Gamma_{21}}{2}\rho_{23} & -\frac{\Gamma_{21}}{2}\rho_{24} \\ 0 & -\frac{\Gamma_{21}}{2}\rho_{32} & 0 & 0 \\ 0 & -\frac{\Gamma_{21}}{2}\rho_{42} & 0 & 0 \end{pmatrix} \tag{3.18}$$

$$\mathcal{L}_{23}(\rho) = \begin{pmatrix} 0 & -\frac{\Gamma_{23}}{2}\rho_{12} & 0 & 0 \\ -\frac{\Gamma_{23}}{2}\rho_{21} & -\Gamma_{23}\rho_{22} & -\frac{\Gamma_{23}}{2}\rho_{23} & -\frac{\Gamma_{23}}{2}\rho_{24} \\ 0 & -\frac{\Gamma_{23}}{2}\rho_{32} & \Gamma_{23}\rho_{22} & 0 \\ 0 & -\frac{\Gamma_{23}}{2}\rho_{42} & 0 & 0 \end{pmatrix} \tag{3.19}$$

$$\mathcal{L}_{24}(\rho) = \begin{pmatrix} 0 & -\frac{\Gamma_{24}}{2}\rho_{12} & 0 & 0 \\ -\frac{\Gamma_{24}}{2}\rho_{21} & -\Gamma_{24}\rho_{22} & -\frac{\Gamma_{24}}{2}\rho_{23} & -\frac{\Gamma_{24}}{2}\rho_{24} \\ 0 & -\frac{\Gamma_{24}}{2}\rho_{32} & 0 & 0 \\ 0 & -\frac{\Gamma_{24}}{2}\rho_{42} & 0 & \Gamma_{24}\rho_{22} \end{pmatrix} \tag{3.20}$$

$$\mathcal{L}_{42}(\rho) = \begin{pmatrix} 0 & 0 & 0 & -\frac{\Gamma_{42}}{2}\rho_{14} \\ 0 & \Gamma_{42}\rho_{44} & 0 & -\frac{\Gamma_{42}}{2}\rho_{24} \\ 0 & 0 & 0 & -\frac{\Gamma_{42}}{2}\rho_{34} \\ -\frac{\Gamma_{42}}{2}\rho_{41} & -\frac{\Gamma_{42}}{2}\rho_{42} & -\frac{\Gamma_{42}}{2}\rho_{43} & -\Gamma_{42}\rho_{44} \end{pmatrix} \tag{3.21}$$

$$\mathcal{L}_{43}(\rho) = \begin{pmatrix} 0 & 0 & 0 & -\frac{\Gamma_{43}}{2}\rho_{14} \\ 0 & 0 & 0 & -\frac{\Gamma_{43}}{2}\rho_{24} \\ 0 & 0 & \Gamma_{43}\rho_{44} & -\frac{\Gamma_{43}}{2}\rho_{34} \\ -\frac{\Gamma_{43}}{2}\rho_{41} & -\frac{\Gamma_{43}}{2}\rho_{42} & -\frac{\Gamma_{43}}{2}\rho_{43} & -\Gamma_{43}\rho_{44} \end{pmatrix} \tag{3.22}$$

$$\mathcal{L}_{41}(\rho) = \begin{pmatrix} \Gamma_{41}\rho_{44} & 0 & 0 & -\frac{\Gamma_{41}}{2}\rho_{14} \\ 0 & 0 & 0 & -\frac{\Gamma_{41}}{2}\rho_{24} \\ 0 & 0 & 0 & -\frac{\Gamma_{41}}{2}\rho_{34} \\ -\frac{\Gamma_{41}}{2}\rho_{41} & -\frac{\Gamma_{41}}{2}\rho_{42} & -\frac{\Gamma_{41}}{2}\rho_{43} & -\Gamma_{41}\rho_{44} \end{pmatrix} \tag{3.23}$$

with the transition rates Γ_{ij} and the density matrix elements ρ_{ij}. To account for additional pure dephasing processes (without transfer of population) between the two ground states as well as between the ground and excited states of the Λ-system, we

introduce the matrix:

$$\mathcal{D}(\rho) = \begin{pmatrix} 0 & -\gamma_{21}\rho_{12} & -\gamma_{31}\rho_{13} & 0 \\ -\gamma_{21}\rho_{21} & 0 & -\gamma_{23}\rho_{23} & 0 \\ -\gamma_{31}\rho_{31} & -\gamma_{23}\rho_{32} & 0 & 0 \\ 0 & 0 & 0 & 0 \end{pmatrix} \tag{3.24}$$

with γ_{ij} the individual dephasing rates acting on the off-diagonal density matrix elements. Finally, the finite laser linewidths additionally increase the dephasing rates of the states coupled to the laser fields and thus have to be taken into account. This effect is introduced into the model by the matrix

$$\mathcal{W}(\rho) = \begin{pmatrix} 0 & -\xi_1\rho_{12} & -\xi_{mut}\rho_{13} & 0 \\ -\xi_1\rho_{21} & 0 & -\xi_2\rho_{23} & 0 \\ -\xi_{mut}\rho_{31} & -\xi_2\rho_{32} & 0 & 0 \\ 0 & 0 & 0 & 0 \end{pmatrix} \tag{3.25}$$

with $\xi_{1,2}$ the linewidths of the individual lasers and ξ_{mut} the mutual coherence of the lasers.

The number of free parameters in the model can be reduced by using certain constraints. First, the Rabi frequencies of both transitions can be linked through:

$$\Omega_2 = \Omega_1 \cdot \sqrt{\frac{P_2}{P_1}} \cdot \frac{\mu_2}{\mu_1} \tag{3.26}$$

with the laser powers $P_{1,2}$ proportional to the square of the laser electric field amplitudes $E^2_{1,2}$ and the transition dipole moments μ_2 and μ_1 of the transitions involved. The group theoretical model used to simulate the optical spectra in Subsection 3.2.3 allows us to determine the relative transition dipole moments $\mu_{ij}^{x,y,z}$ of the individual optical transitions. With the resulting relative transition dipole moments, the individual transition rates Γ_{ij} can be linked to the total spontaneous decay rate Γ by the equation:

$$\Gamma_{ij} = \frac{(\mu_{ij}^x + \mu_{ij}^y + \mu_{ij}^z)}{\sum(\mu_{ij}^x + \mu_{ij}^y + \mu_{ij}^z)}\Gamma \tag{3.27}$$

with the total spontaneous decay rate $\Gamma = \tau^{-1}$ where $\tau = 1.66\,\text{ns}$ is the spontaneous emission lifetime of the SiV^-. We furthermore assume thermalisation between states 2

and 4 with $\Gamma_{42} = \Gamma_{24} e^{-\frac{\Delta E_{24}}{k_B T}}$, where ΔE_{24} is the average energy between the state $|D\rangle$ and the other excited states $|C\rangle$, $|B\rangle$ and $|A\rangle$. Finally, the two dephasing rates γ_{21} and γ_{23} are chosen such that they reproduce the total linewidth of the optical transition and are kept constant at these values (these parameters do not affect the width of the CPT dip).

This approach allows us to reduce the free parameters in the model to the Rabi frequency Ω_1 and the ground state dephasing rate γ_{31}. A single set of these parameters can be identified to model the CPT dip observed experimentally. The system of differential equations defined by Eq. 3.15 is solved numerically over the experimental integration time of 0.5 s, with a steady-state being reached within this time interval. This resolution is performed for a range of values of the probe frequency detuning. Experimentally, we measure the fluorescence from the transitions from the lower orbital branch of the excited state (levels $|A\rangle$ and $|B\rangle$ as shown in Fig. 3.8). We thus plot the normalised population of state $|4\rangle$ as a function of the two-photon detuning of the lasers. By fitting the CPT curve of Fig. 3.10, we extract from the model the following set of transition rates:

$$\begin{aligned} \Gamma_{21} &= 2\pi \cdot 3.0\,\text{MHz} \quad & \Gamma_{23} &= 2\pi \cdot 4.7\,\text{MHz} \\ \Gamma_{24} &= 2\pi \cdot 88.1\,\text{MHz} \quad & \Gamma_{42} &= 2\pi \cdot 40.5\,\text{MHz} \\ \Gamma_{41} &= 2\pi \cdot 19.3\,\text{MHz} \quad & \Gamma_{43} &= 2\pi \cdot 20.9\,\text{MHz} \end{aligned} \tag{3.28}$$

and dephasing rates:

$$\gamma_{21} = 2\pi \cdot \gamma_{23} = 3250\,\text{MHz} \tag{3.29}$$

$$\gamma_{31} = 2\pi \cdot 3.5\,\text{MHz} \tag{3.30}$$

Among them, the ground state dephasing rate $\gamma_{31}/2\pi = 3.5 \pm 0.2\,\text{MHz}$ leads to a dephasing time $T_2^* = 45 \pm 2\,\text{ns}$ for the spin of the SiV^-.

3.5 Magnetic field dependence

From a general point of view, the coherence time measured by CPT is strictly speaking the coherence time between the two addressed ground states whether they be characterised by a spin state or not. It would thus be conceivable that the coherence time we have measured corresponds to an inherent coherence time of two ground state

levels of the SiV^- and is actually not correlated with their spin projections. In order to evaluate the influence of the spin state on the measured coherence time, we take advantage of the presence of an avoided crossing between states $|2\rangle$ and $|3\rangle$ around 3.5 T, as seen in Fig. 3.12a. As the magnetic field brings the states closer to their avoided crossing, their respective spin projections are altered, as depicted by tilted arrows. We thus want to use CPT to measure how the coherence time between the ground states is affected by this change of their spin projections. Before the avoided crossing, from 0 to 3.5 T, the dark state is created between states $|1\rangle$ and $|2\rangle$, and beyond the avoided crossing, above 3.5 T, between $|1\rangle$ and $|3\rangle$, as illustrated by the orange and green ribbons respectively. Figure 3.12b displays the evolution of the width of the CPT dip as a function of the applied magnetic field (between states $|1\rangle$ and $|2\rangle$ as orange dots and between states $|1\rangle$ and $|3\rangle$ as green dots). Those measurements are performed at the same laser powers with respect to saturation so that the power broadening is held constant. We can see that the CPT dip width is minimum away from the avoided crossing and increases rapidly when getting closer to it. This implies that the coherence between the ground states is drastically reduced by the avoided crossing, when the spin projections of the addressed levels cease to be opposite.

In order to confirm the correlation between alteration of the spin orientation and reduction of coherence, we make use of the group theoretical model of the SiV^- states to calculate the spin overlap between the two addressed ground states as a function of the magnetic field. We proceed to extract the spin orientation along the SiV axis for the three addressed ground states through the projection method described in Section 2.5. Applying the projector $\mathcal{P} = |\uparrow\rangle\langle\uparrow| + |\downarrow\rangle\langle\downarrow|$ to an eigenstate $|\Psi\rangle$, we can express the obtained projection onto the spin subspace as $\mathcal{P}|\Psi\rangle = \cos(\theta/2)|\uparrow\rangle + e^{i\phi}\sin(\theta/2)|\downarrow\rangle$ to represent this spin as a vector on a Bloch sphere, as shown in Fig. 3.13 for the three ground state levels $|1\rangle$, $|2\rangle$ and $|3\rangle$.

We can see that the Bloch vectors of states $|1\rangle$ and $|2\rangle$ are antiparallel until state $|2\rangle$ undergoes an avoided crossing with state $|3\rangle$. Above this avoided crossing, states $|1\rangle$ and $|2\rangle$ have similar S_z components, and the Bloch vectors are not antiparallel any more, while states $|1\rangle$ and $|3\rangle$ now have opposite Bloch vectors. From this, we evaluate the spin overlap between states by calculating the squared scalar product of the spin projections of the two states, such as $\left|\langle 1|P^\dagger P|2\rangle\right|^2$. We then multiply this value by a Boltzmann factor $e^{-\Delta E/k_B T}$, where ΔE is the energy difference between the two states considered, $T = 4\,\mathrm{K}$ is the temperature and k_B is the Boltzmann constant. This

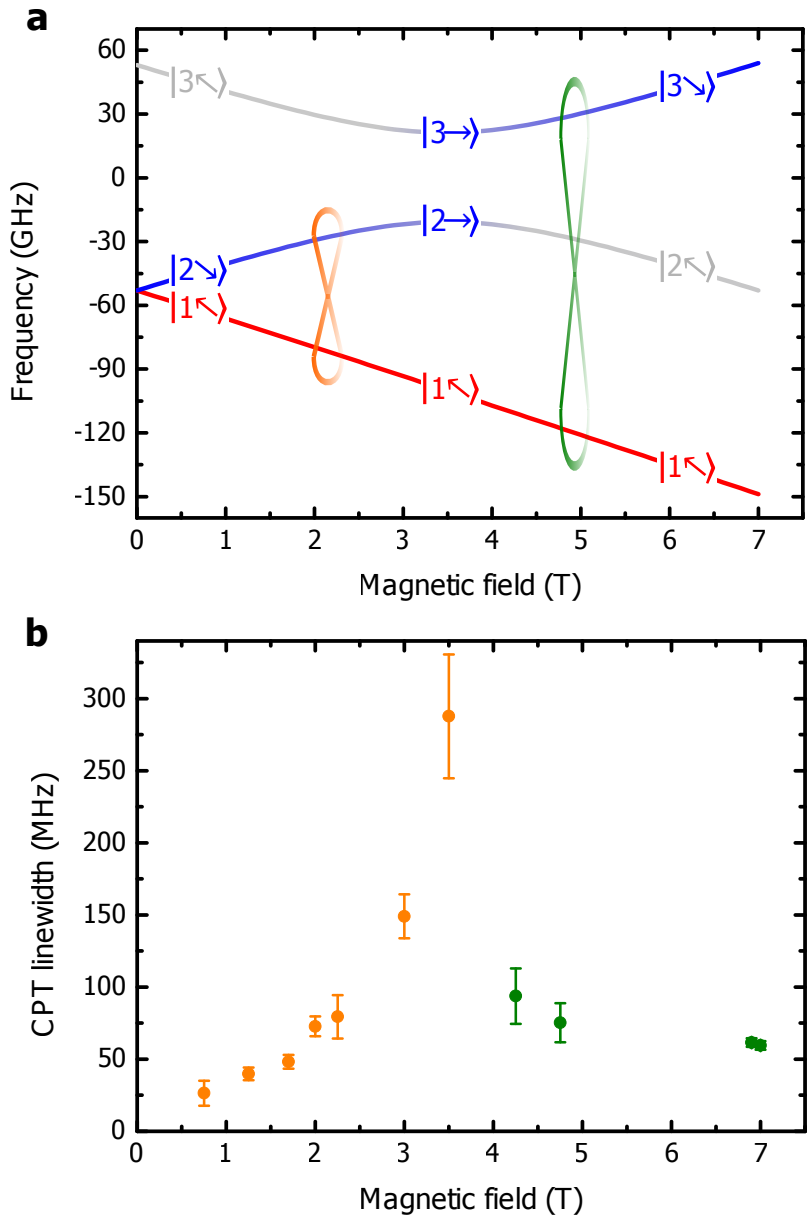

Figure 3.12 Evolution of the ground state coherence across a level avoided crossing. (a) Simulated ground state energy levels for the SiV^- studied (same as those in Fig. 3.6), illustrating the spin state for magnetic field values below, above and at the avoided crossing. (b) Full width at half maximum of the CPT dip as a function of the magnetic field, extracted using a Lorentzian fit. Dots denote measured widths (for each transition, laser powers are equal to four times the saturation power), with the error bars being the standard deviation of multiple measurements. In panels (a) and (b), the colours orange and green indicate CPT realised between states $|1\rangle$ and $|2\rangle$, and between $|1\rangle$ and $|3\rangle$, respectively.

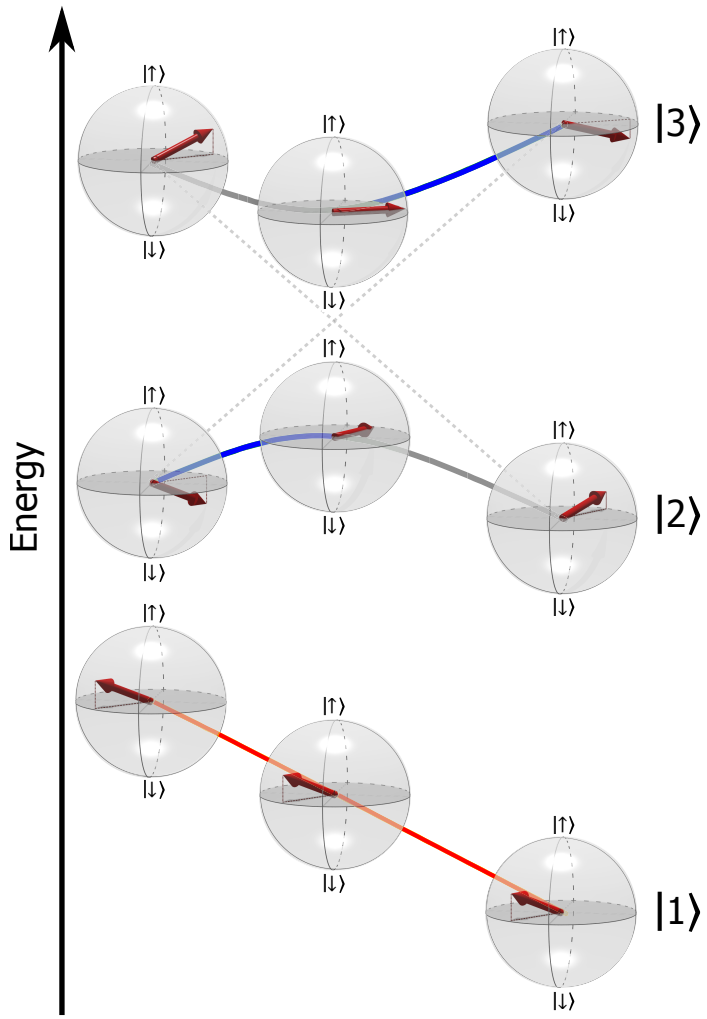

Figure 3.13 Representation of the spin vector of states $|1\rangle$, $|2\rangle$ and $|3\rangle$ on Bloch spheres at 1 T, 4 T and 7 T. The basis states are those of the spin-orbit coupling, along the SiV axis (*see* Sction 2.4).

factor aims to account crudely for the influence of thermal phonons which are vectors of orbital relaxation (this will be investigated in more details in Chapter 5 Section 5.2).

The product of the spin overlap and Boltzmann factor as a function of the magnetic field is finally compared to the experimental CPT dip widths, as shown in Fig. 3.12b where the orange curve corresponds to $|1\rangle$-$|2\rangle$ and the green curve to $|1\rangle$-$|3\rangle$. We use a function of the form $a + b \cdot \left| \langle 1|P^\dagger P|2/3\rangle \right|^2 e^{-\Delta E/k_B T}$, where a and b are free parameters common to both curves and $|2/3\rangle$ corresponds to $|2\rangle$ before the avoided crossing and to $|3\rangle$ after it. The offset a corresponds to the contributions to the CPT dip width of the power broadening, the mutual coherence of the two lasers (5 MHz here), as well as

further decoherence mechanisms. Those mechanisms likely include magnetic noise from neighbouring spins such as those of NV^- centres, paramagnetic N atoms or ^{13}C nuclear spins. The same functions comprising only the spin overlap without the Boltzmann factor are plotted as grey dashed curves.

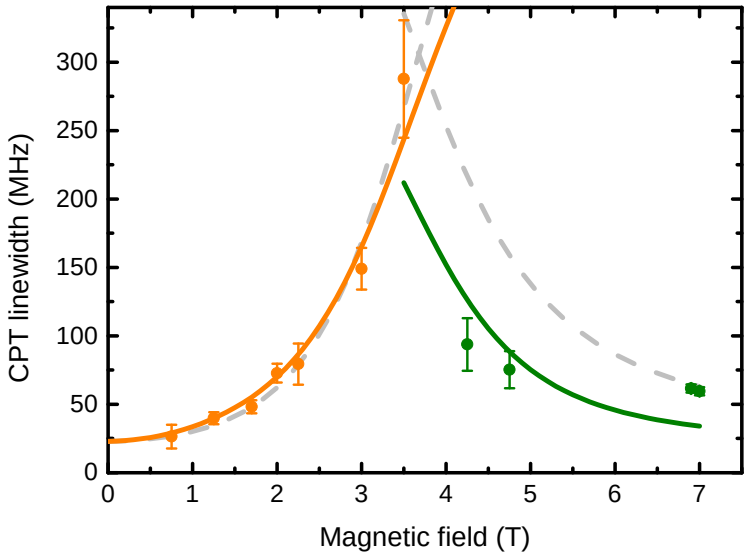

Figure 3.14 CPT dip width compared to the overlap of the spin projections. Experimental values of the CPT dip width presented in Fig. 3.12b, superimposed with the fitted curves corresponding to the spin overlap between the levels addressed in CPT (grey dashed curves). The solid curves correspond to the spin overlap between the states, multiplied by a Boltzmann factor. The colours orange and green indicate CPT realised between states $|1\rangle$ and $|2\rangle$, and between $|1\rangle$ and $|3\rangle$, respectively.

The good agreement between the evolution of the spin overlap and the CPT dip width confirms that the measured coherence times correspond to those of the spin state. We can interpret the observed variation of the spin coherence time as follows: away from the avoided crossing, the opposite spin projections of the two addressed states prevent direct decoherence by phonons resonant with their Zeeman splitting, as phonons do not carry a spin. In contrast, at the avoided crossing, where the spin projections of $|2\rangle$ and $|3\rangle$ have a significant overlap with all the other ground state levels, such phonon-induced transitions are possible, thus opening extra decoherence channels. The mechanisms for spin decoherence will be examined in Chapter 5 Section 5.2.

3.6 Conclusion

By utilising coherent population trapping on a single SiV^- centre, we have obtained a first evaluation of 45 ± 2 ns for the dephasing time between two ground state levels with opposite spin orientations. This value has been shown to be considerably reduced when the addressed levels do not have opposite spin projections, thus confirming that this dephasing time is that of the SiV^- spin. The mechanisms for spin decoherence will be examined in Chapter 5 Section 5.2, but this result already hints at a central role played by lattice phonons.

The realisation of coherent population trapping opens the way to all-optical control of the SiV^- spin [162, 163]. Indeed, in this experiment, the superposition of spin corresponding to the generated dark state was not controlled. However, by implementing amplitude and phase control of the driving lasers (as seen in equation 3.12), it becomes possible to prepare an arbitrary dark state and hence superposition of spin [164]. Manipulation of the spin can then be achieved through stimulated Raman adiabatic passage (STIRAP) or optically driven Rabi oscillations [165], which both rely on the CPT configuration. Furthermore, all-optical control can be performed with picosecond pulses thus leading to ultra-fast spin manipulation [163, 44]. Finally, this constitutes a first step towards using the SiV^- centre to interface spin and photons, which is a key element of a quantum network.

Chapter 4

Coherent control of a single SiV^- centre electronic spin

The electronic spin of the SiV^- centre shows promise as a quantum bit, all the more so since it can be used in combination with coherent photons emitted by the SiV^-. In a quantum network, while photons would act as information and entanglement vectors between nodes, the spin would be used to process information and thus be at the core of the processing speed-up expected from quantum computing. In this context, achieving coherent control of the SiV^- spin constitutes a fundamental step towards the implementation of spin-based quantum computing.

In this chapter, we present the realisation of optically detected magnetic resonance and microwave-based coherent control of the spin of a single SiV^- centre. This control is then used for basic quantum sequences in order to extract a direct measurement of the spin coherence. Those results were obtained with the technical assistance of David-Dominik Jarausch, Christian Hepp, Lina Klintberg and Jonas N. Becker, and have been published in Ref. [166].

4.1 Experimental conditions

4.1.1 Sample

The sample used for this experiment is a high-pressure-high-temperature (HPHT) type IIa bulk diamond (provided by Dr. Mathew Markham from Element Six) with surface oriented orthogonally to the <111> crystallographic axis. The sample was implanted with isotopically purified $^{29}Si^+$ ions, which possess a nuclear spin $I = 1/2$

(implantation performed by Dr. Detlef Rogalla at RUBION, Bochum, Germany). The implantation energy of 900 keV leads to an average implantation depth of 500 ± 50 nm below the diamond surface. This value is determined through simulations using the stopping-range-of-ions-in-matter algorithm (SRIM) described in [109]. From one implantation site to the other, the implantation doses were tuned from 10^9 ions/cm^2 to 10^{12} ions/cm^2 to guarantee that at least one implantation site has a low enough SiV^- concentration to measure single centres without them being too sparse. The sample has been subsequently annealed for 3 hours at 1000 °C in vacuum, to allow vacancies to become mobile and form SiV centres, and oxidised in air for 1 hour at 460 °C to remove surface graphitisation. Single SiV^- centres have been found in the 10^{10} ions/cm^2 area. In order to circumvent total internal reflection and increase the fluorescence collection efficiency, arrays of solid immersion lenses (SILs) with 500 nm radius have been etched using focused ion beam milling (FIB) in the 10^{10} ions/cm^2 area, as described in Section 3.2.2 (FIB milling performed by C. Pauly). SiV^- centres are randomly located in the SILs.

4.1.2 Experimental setup

The experimental setup is similar to the one used in Chapter 2. The sample is mounted in a closed cycle liquid helium cryostat (Attodry 1000) reaching a base temperature of 3.5 K. The temperature of the sample can be tuned via a resistive heater and evaluated using a thermocouple, both located under the sample mount. The temperature is also increased by heating due to the microwave pulses. Due to the limited thermal conductivity of the sample mount, the temperature is likely to be underestimated when heating is due to the microwave and overestimated when it is provided by the heater. A magnetic field ranging from 0 to 9 T can be applied to the sample thanks to a superconducting coil around the sample space. The magnetic field is applied along the optical axis.

Resonant excitation of the SiV^- is performed as in Chapter 2 using a frequency-tunable diode laser (Toptica DL pro design), the frequency of which is maintained in resonance through continuous feedback from a wavelength meter (High Finesse WSU). Resonant optical pulses are generated with an acousto-optic modulator (AOM, AAOptoelectronic MT350-A0.12-800), which is triggered by a delay generator (Stanford Research Systems DG645). The optical pulses are sent to the sample using a home-built confocal microscope mounted on top of the cryostat. The laser is focused onto the sample through a microscope objective with $NA = 0.82$ inside the sample

chamber. Piezoelectric stages (Attocube ANPx101 and ANPz101) on top of which the sample is mounted, allow the sample to be moved with respect to the objective. The fluorescence from the SiV^- is collected through the same objective. The laser light, and consequently the SiV^- fluorescence from the excited transition, are filtered out using a home-built monochromator and the fluorescence from the remaining transitions is sent to an avalanche photodiode (PicoQuant Tau-Spad). The signal from the avalanche photodiode is sent to a time-to-digital converter (qutools quTAU) triggered by the delay generator. An alternating current at a set frequency in the microwave regime is generated by a frequency generator (Stanford Research Systems SG384) and sent to a switch to produce microwave pulses. The switch is controlled by the delay generator used for optical pulses in order to synchronise the optical and microwave parts of the experiment. The microwave pulses are then amplified by a microwave amplifier (Mini-Circuits ZHL-16W-43-S+). The microwave pulses travel through semi-rigid cables installed inside the cryostat. A single copper wire (20 µm diameter) positioned on top of the sample, as seen Fig. 4.1, allows the microwave to be radiated less than 20 µm away from the studied SiV^-, marked by a red dot.

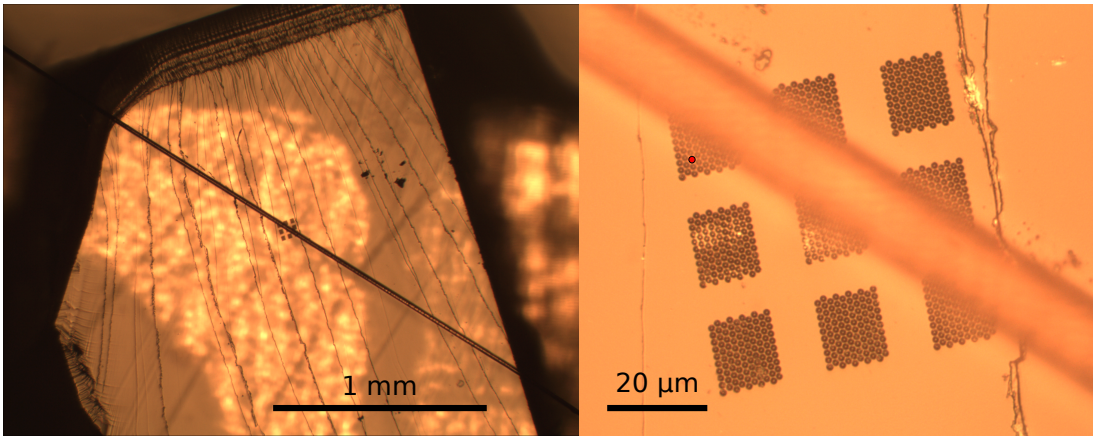

Figure 4.1 Optical microscope pictures of the surface of the diamond sample. At the centre, a 3x3 array of solid immersion lenses (SILs) etched into the diamond surface are crossed by a 20 µm-diameter copper wire. On the right picture, the location of the SiV^- studied is indicated by a red dot.

4.1.3 Characterisation of the SiV$^-$ centre studied

As the surface of the sample is orthogonal to the <111> crystallographic axis, approximately one quarter of SiV$^-$ centres are aligned with the optical axis and three quarters make an angle of 109.5° to it. Only the latter are in practice visible, the optical dipole of the SiV$^-$ being oriented along its symmetry axis.

The SIL arrays are scanned to find suitable emitters. The emitter chosen for this experiment is first characterised under non-resonant excitation at 660 nm. The obtained spectra as a function of the magnetic field are displayed in Fig. 4.2. The group theoretical model described in Chapter 2 Section 2.4 is used to fit the spectra and hence deduce the energy levels of this emitter, as shown in Fig. 4.3. With a ground state orbital splitting of nearly 50 GHz, this emitter appears relatively unstrained.

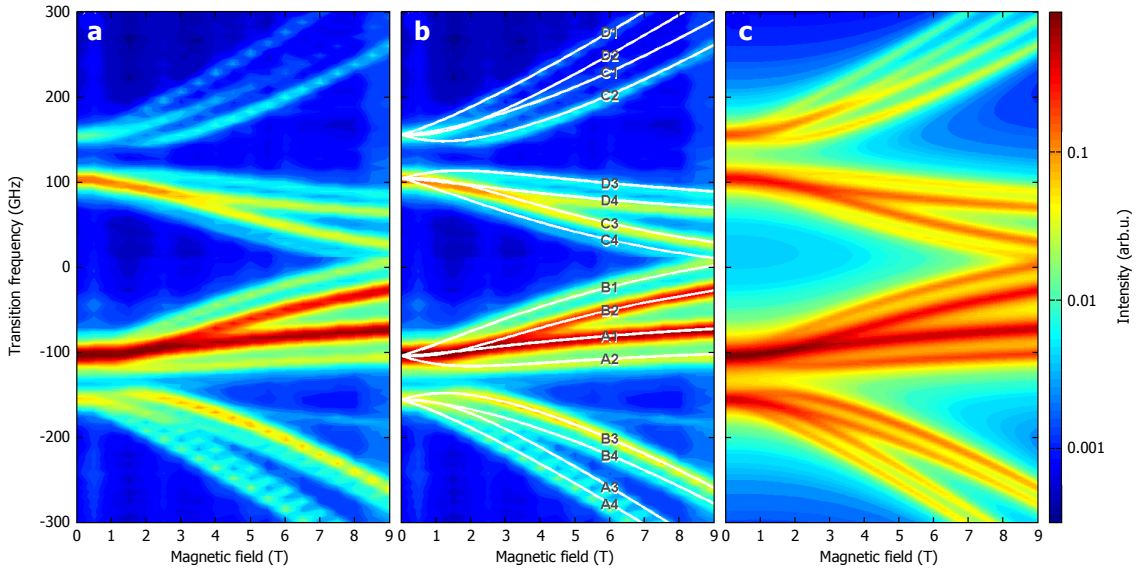

Figure 4.2 Magnetic field dependence of optical transitions. (a) Experimental spectra of the SiV$^-$ centre studied under non-resonant excitation as a function of the applied magnetic field at an angle of $109.5 \pm 1.0°$. The colour scale indicates the relative fluorescence intensity in logarithmic scale. (b) Experimental spectra superimposed with the transition frequencies (white curves) simulated using the group theoretical model described in Section 2.4. Each transition is labelled according to its associated excited (A to D) and ground states (1 to 4). (c) Simulated spectra using the group theoretical model.

Subsequently, photoluminescence excitation (PLE) is measured on transition D1 and gives an optical linewidth of 600 MHz. This transition is thus optically resolvable

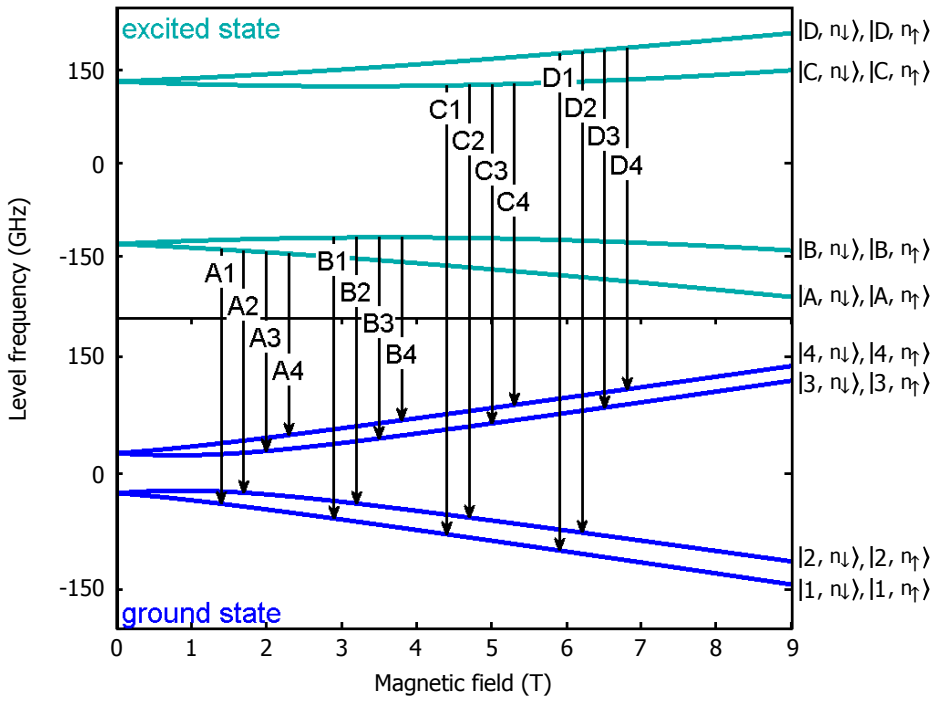

Figure 4.3 Simulated magnetic field dependence of the energy levels of the SiV^- centre corresponding the the transitions in Fig. 4.2. The labelling of the levels includes the nuclear spin state $I = 1/2$ of the ^{29}Si, indicated by $n_\uparrow$ and $n_\downarrow$, although its influence is not visible at those frequency scales.

at a magnetic field as low as 0.2 T. At this magnetic field, the Zeeman splitting is almost 3 GHz, making it easily addressable by microwave pulses.

4.2 Spin initialisation, readout and population relaxation

A magnetic field of approximately 0.2 T is applied to the sample to lift the spin degeneracy of the SiV^- centre, as illustrated in Fig. 4.4. The diode laser is tuned into resonance with transition D1. The fluorescence from the SiV^- is measured on the transitions indicated by solid grey arrows. First, a 500 ns optical pulse depletes the spin-up state 1 and initialises the SiV^- into the spin-down state 2 by optical pumping. The fluorescence collected during this first pulse, displayed in Fig. 4.5, decreases rapidly and saturates as the optical pumping is compensated by population decay back into state 1. It is possible to estimate the initialisation fidelity by considering the ratio of about 5 to 1 between the leading edge of the initialisation pulse (corresponding to

approximately 50 % of the total population as the system is initially thermalised) and the saturation value. This gives an approximate value of about 90 % of initialisation fidelity into the spin down state. A more precise value of 86 ± 2 % is extracted from an eight-level master equation model, as described in Section 4.5

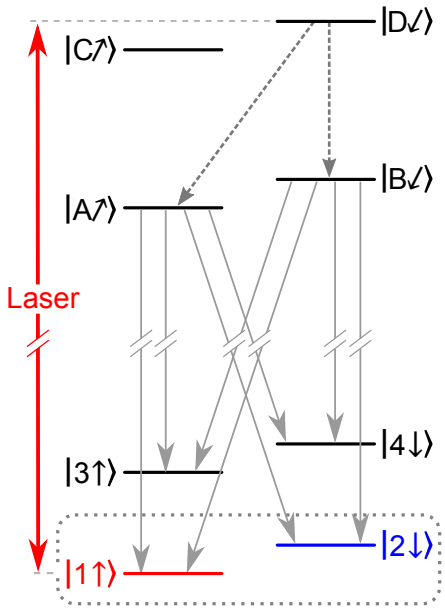

Figure 4.4 Representation of the SiV$^-$ energy levels with an applied magnetic field. The labels of the levels include their electronic spin orientation at about 0.2 T. The tilt in the indication of the spin in the excited state indicates the difference in quantisation axis between the ground and excited states. The resonant laser is depicted as a red double arrow. Grey dashed arrows correspond to the fast thermalisation among excited state levels. The transitions used for detection are marked by solid grey arrows. For clarity, the nuclear spin is not indicated. In the ground state, the dashed grey box highlights the levels 1 and 2 of the lower orbital branch on which we focus, while the levels 3 and 4 form the upper orbital branch.

The readout of the spin state is performed analogously with a second optical pulse, identical to the initialisation pulse and therefore resonant with transition D1, as shown in Fig. 4.5. The recorded fluorescence displays again optical pumping, with the leading edge indicating the degree of population recovery into the originally depleted spin-up state 1.

The spin state measurement, corresponding to the spin-up population, is taken as the peak ratio between the leading edge of the readout pulse fluorescence integrated over 30 ns and that of the initialisation pulse fluorescence, as illustrated by the dark grey areas in Fig. 4.5. This measurement method is resilient with regards to slow laser

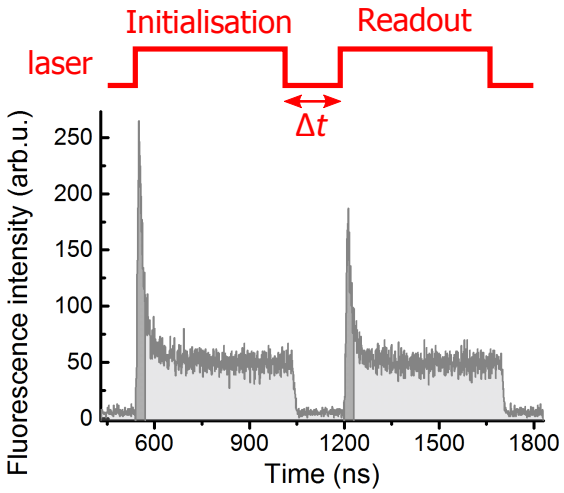

Figure 4.5 Optical initialisation and readout of the SiV^- electronic spin. The top part describes the resonant laser intensity pattern in time, composed of an initialisation pulse and a readout pulse separated by a time delay Δt. The lower part displays the corresponding fluorescence measured from the SiV^- which shows optical pumping. The dark grey area under the curve indicates the signal integrated over 30 ns under the peaks of the initialisation and readout pulses for the calculation of the peak ratio.

power fluctuations and frequency drift of the SiV^-, as both leading edges are affected similarly, their ratio remaining relatively less affected.

As the time delay Δt between the two optical pulses is increased, the recovery of the spin-up population increases, as shown in Fig. 4.6. The exponential recovery is fitted by a function of the form $1 - A \cdot exp(-\Delta t/T_{1,spin})$, where A is the amplitude of the recovery and depends on the initialisation fidelity and $T_{1,spin}$ is the spin population decay time. This allows us to extract a spin relaxation time $T_{1,spin} = 350 \pm 11$ ns at 3.5 K. This spin population decay time sets an upper bound for any subsequent coherent manipulation of the electronic spin.

It should be noted that at temperatures around 4 K, thermally excited lattice phonons are responsible for a Boltzmann distribution of the population between the two orbital branches of the ground state. This results in approximately 2/3 of the population in the lower branch states and 1/3 in the upper branch states. As it will be shown later, the rate of population transfer between the orbital branches is relatively fast compared to the population decay rate between states of different electronic spin projections within a branch, a phenomenon already evidenced in Section 3.5. As a consequence, the optical pulses are long compared to the inter-branch transitions and

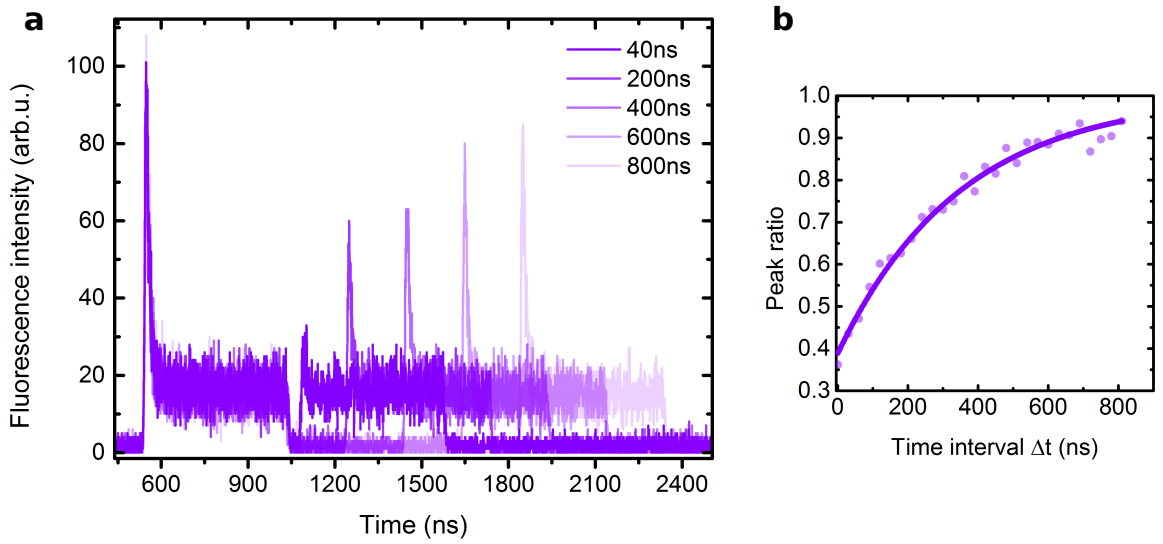

Figure 4.6 Spin decay time $T_{1,spin}$ at 3.5 K and 0.2 T (angle of $109.5 \pm 1.0°$ to the SiV axis). (a) Initialisation and readout pulses fluorescence signals as a function of the time delay between initialisation and readout. (b) Variation of the peak ratio as a function of the time delay (purple dots) and exponential fit (purple curve) with 1/e value $T_{1,spin} = 350 \pm 11$ ns.

the peak ratio as a spin state measurement is not altered by shelving into the orbital branches.

4.3 Optically detected magnetic resonance

We now aim to achieve optically detected magnetic resonance (ODMR), as a first step in addressing the SiV$^-$ spin with a microwave field.

The dissipation of microwaves in the transmission lines and wire generates heating. As a consequence, the use of a pulsed instead of continuous microwave radiation limits the temperature rise. Furthermore, due to the relatively short $T_{1,spin}$ of a few hundreds of nanoseconds, the microwave pulse has to be short enough to limit the loss of ODMR contrast due to spin population decay between initialisation and readout. The use of short pulses however broadens the ODMR signal proportionately to the inverse of the pulse duration, and can limit the ODMR contrast due to insufficient driving of the spin. As a consequence, we choose to apply a 140 ns microwave pulse, as a trade-off between those considerations.

Keeping the initialisation and readout optical pulses unchanged and fixing the delay between them at 160 ns, a 140 ns microwave pulse is applied during the time interval,

as illustrated in Fig. 4.7a. The associated heating increases the measured temperature to 4.3 K, at which $T_{1,spin} = 200$ ns (the temperature dependence of $T_{1,spin}$ is described in Chapter 5).

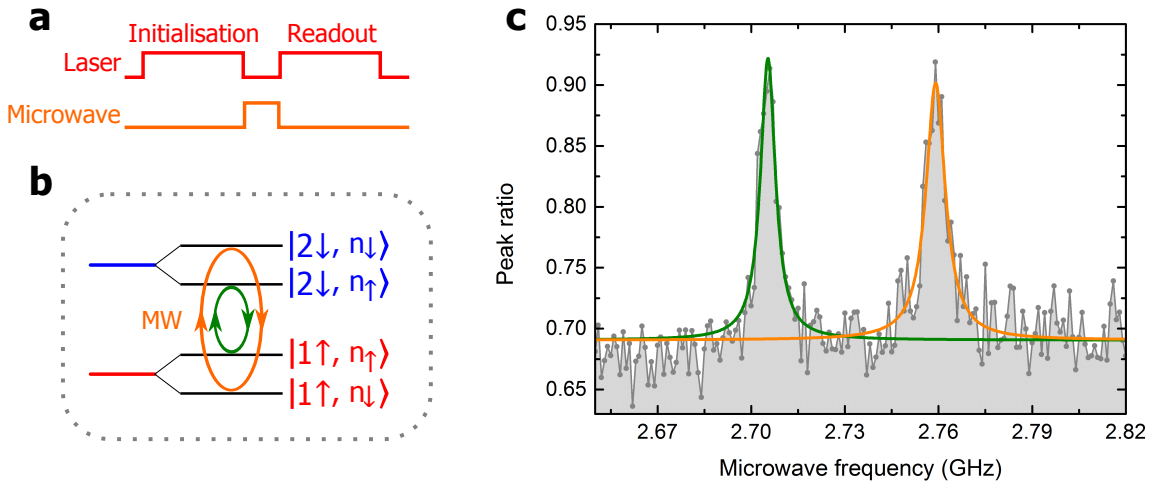

Figure 4.7 Optically detected magnetic resonance (ODMR). (a) Illustration of the microwave and resonant laser pulse patterns in time. (b) Energy level diagram of the electronic spin states in the ground state lower orbital branch split by the hyperfine interaction with the ^{29}Si $I = 1/2$ nuclear spin. The levels are labelled as in Fig. 4.4, with the addition of the nuclear spin orientations $n_\uparrow$ and $n_\downarrow$. A microwave pulse can flip the electronic spin while leaving the nuclear spin unchanged, which results in two possible microwave-induced transitions (orange and green circular arrows). (c) ODMR spectrum of the SiV^- at 0.202 T: the two microwave transitions appear as two peaks, each fitted with a Lorentzian function (colours correspond to those in (b)). The two peaks are separated by 53.7 ± 0.3 MHz (errors from the fits).

Because of the nuclear spin 1/2 of the ^{29}Si isotope, each electronic spin state is split by the hyperfine interaction, as depicted in Fig. 4.7b. The microwave can only drive the electronic spin, while the nuclear spin remains unchanged during the few hundred ns pulse, the nuclear spin magnetic moment being about three orders of magnitude smaller than the electronic one. This results in two possible microwave resonances, shown in Fig. 4.7b by circular arrows. As the microwave frequency is resonant with one of those two transitions, the microwave drives population from the initialised spin-down state back into the depleted spin-up state. This leads to a recovery of fluorescence and thus appears as a peak in the ODMR spectrum. Figure 4.7c shows the obtained ODMR spectrum at 0.202 T. The spectrum displays two peaks corresponding to the two expected resonances. The peaks are separated by 53.7 ± 0.3 MHz, corresponding to

a hyperfine splitting of approximately 27 MHz (Further considerations on the hyperfine interaction will be developed in Chapter 5.)

The ODMR contrast, taken as the ratio between the peak height and the baseline, is about 30 %. This can be compared to contrasts of standard ODMR scans with NV^- centres, with maximum values of 20 % and 40 % in continuous and pulsed ODMR, respectively [167, 168]. It should be noted however that the mechanisms involved are different, with the contrast in NV^- relying on spin-dependent shelving into a long-lived excited state [169]. ODMR measurements performed on NV^- centres at low temperatures with spin initialisation through resonant optical pumping and microwave π-pulses reach contrasts of approximately 80 % [170]. At the microwave power used here, the 140 ns microwave pulse corresponds to a π-pulse, transferring the spin from the initialised spin-down state back to the spin-up state, and is thus expected to provide the maximum contrast achievable. However, the contrast is limited by the short spin decay time of $T_{1,spin} = 200\,\text{ns}$ leading to both imperfect initialisation and population recovery irrespective of the microwave frequency. $T_{1,spin}$ and initialisation fidelity have been reported to vary with the angle between the magnetic field and the symmetry axis of the SiV^-, with $T_{1,spin}$ increasing from 60 ns for an angle of 70° to 2.4 ms for an angle close to 0° [171]. As a consequence, it is expected that the contrast can be increased considerably for small angles between the magnetic field and the SiV^- symmetry axis.

It is important to notice that, in the absence of the Jahn-Teller effect (or strain), an oscillating magnetic field cannot drive the transition between the Zeeman-split levels within an orbital branch (here levels 1 and 2). Indeed, such levels differ in spin and orbital, as shown in Fig. 2.11. This can be seen by considering the matrix of the Zeeman effect (see Section 2.4) in the spin-orbit basis $\{|e_x\uparrow\rangle, |e_x\downarrow\rangle, |e_y\uparrow\rangle, |e_y\downarrow\rangle\}$:

$$\mathcal{H}_{Zee} = \begin{pmatrix} -f\gamma_S B_z + \gamma_S B_z & \gamma_S B_x & 0 & 0 \\ \gamma_S B_x & -f\gamma_S B_z - \gamma_S B_z & 0 & 0 \\ 0 & 0 & f\gamma_S B_z + \gamma_S B_z & \gamma_S B_x \\ 0 & 0 & \gamma_S B_x & f\gamma_S B_z - \gamma_S B_z \end{pmatrix} \tag{4.1}$$

where we assume $B_y = 0$. We can see that it does not have non-diagonal components between states of different spin-orbit-defined orbitals. It is thus necessary to rely on the Jahn-Teller effect (or strain) to mix these spin-orbit-defined orbitals (see Section 2.4) in order to be able to drive the spin transitions within an orbital branch.

4.4 Rabi oscillations

The microwave frequency is now fixed in resonance with one of the two transitions and the duration of the microwave pulse is varied, as illustrated in Fig. 4.8a. To avoid any overlap between the microwave pulse and the end of the initialisation pulse, the microwave pulse starts 10 ns after triggering the end of the optical pulse, which allows the AOM-controlled laser intensity to reach a negligible level. The delay between initialisation and readout is held constant at 210 ns, a value which accommodates the longest microwave pulse. Changing the delay between initialisation and readout optical pulses in order to read out the spin state immediately after the end of the microwave pulse would include the effect of the spin population decay into the signal as $T_{1,spin}$ is comparable to the microwave pulse timescale.

Figure 4.8b shows the evolution of the spin-up population, measured through the peak ratio described earlier, as the microwave pulse duration is increased. In the top panel, the microwave is resonant with the transition between the states $\left|1\uparrow, n_\uparrow\right\rangle$ and $\left|2\downarrow, n_\uparrow\right\rangle$, where the nuclear spin is up, while in the bottom one, it is resonant with the transition between states $\left|1\uparrow, n_\downarrow\right\rangle$ and $\left|2\downarrow, n_\downarrow\right\rangle$, where the nuclear spin is down. The spin-up population (the optical pulse reads out the population in $|1\uparrow\rangle$) displays Rabi oscillations, demonstrating the coherent control of the SiV^- electronic spin (see Subsection 3.1.1 for the theory of Rabi oscillations; here, the electric dipole and the electric field of the usual description are replaced by the spin magnetic moment and the microwave oscillating magnetic field respectively). The oscillations are not centred around a peak ratio value of 1, which corresponds to the equal thermal populations between the two electronic spin states before initialisation. This comes from the fact that, due to the hyperfine splitting, the microwave pulse only addresses resonantly the electronic spin state associated with one of the two nuclear spin orientations. The relatively fast decay of the oscillations is likely an indication of a short spin dehasing time. Finally, the oscillations exhibit an upward drift which cannot be explained considering only the dynamics among the levels of the ground state lower orbital branch.

In order to verify that those oscillations correspond to Rabi oscillations, we repeat the same experiment for different values of microwave power and detuning from resonance. As expected, the Rabi frequency varies linearly with the square root of the input microwave power, as shown in Fig. 4.9a. The dependence of the effective Rabi frequency with detuning from resonance, shown in Fig. 4.9b, also behaves as expected,

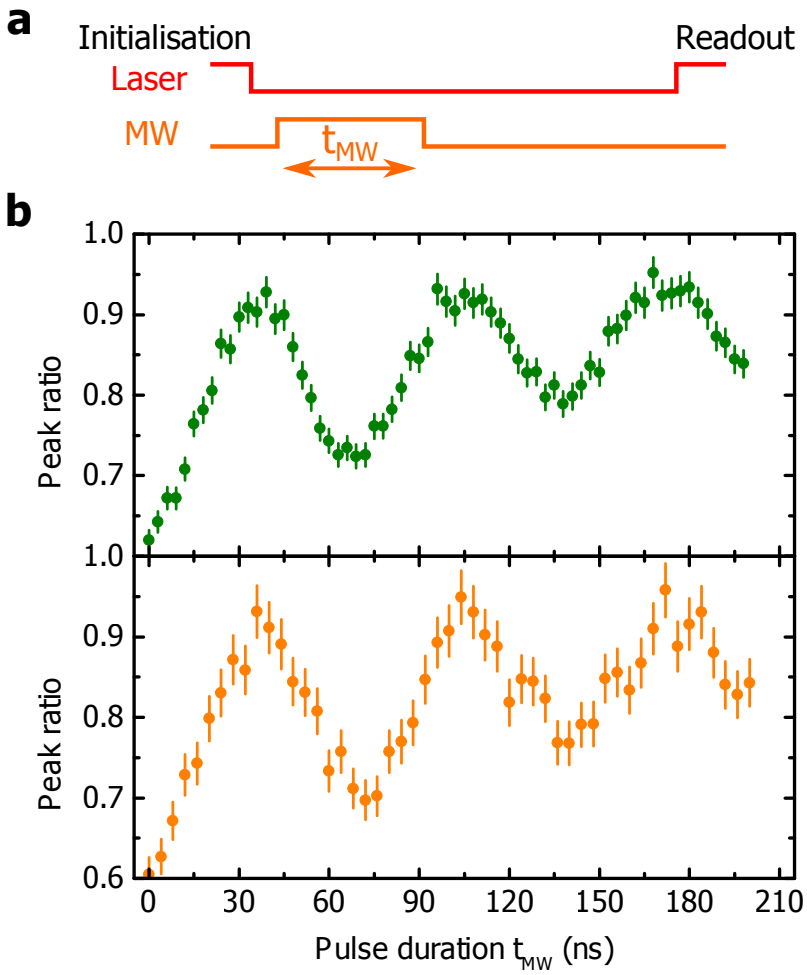

Figure 4.8 Rabi oscillations. (a) Resonant laser and microwave pulse scheme, with the duration of the microwave pulse t_{MW} being varied. The time interval between initialisation and readout is held constant at 210 ns. (b) Variation of the peak ratio as a function of the microwave pulse duration t_{MW} at 0.214 T for a microwave frequency resonant with the transition between states $\left|1\uparrow, n_\uparrow\right\rangle$ and $\left|2\downarrow, n_\uparrow\right\rangle$ (green dots), and between states $\left|1\uparrow, n_\downarrow\right\rangle$ and $\left|2\downarrow, n_\downarrow\right\rangle$ (orange dots) (colours correspond to those in Fig. 4.7b). The error bars correspond to the standard deviation of the peak ratio (the two graphs have different integration times leading to different error bars).

with a variation of the form $\sqrt{\Omega^2 + \delta^2}$, where Ω is the bare Rabi frequency in resonance and δ is the detuning.

The maximum bare Rabi frequency observed is about 15 MHz, which is comparable to the values obtained with NV$^-$ centres in similar experimental conditions. This similarity in coupling to a microwave radiation is promising for using strip lines or antenna structures developed with NV$^-$ centres [172, 173], in order to implement

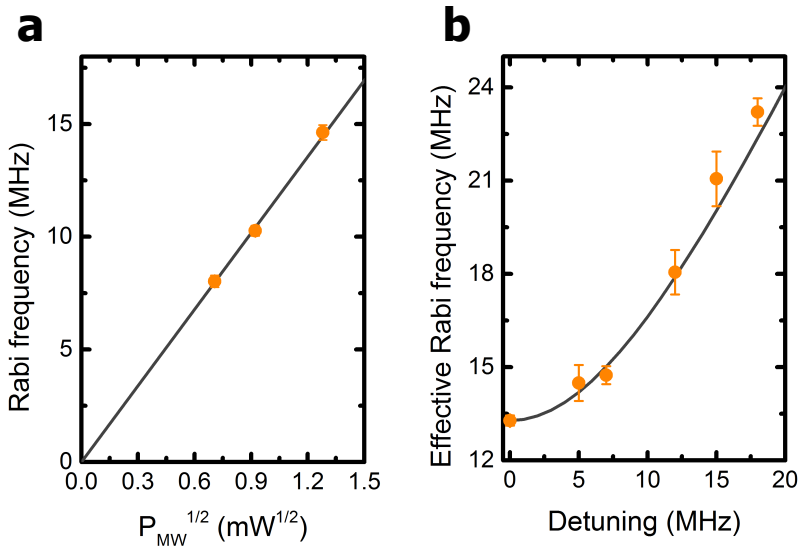

Figure 4.9 Dependence of the Rabi oscillations upon microwave power and detuning. (a) Variation of the Rabi frequency (orange dots) as a function of the square root of the input microwave power P_{MW}, for a microwave resonant with the transition between states $\left|1\uparrow, n_\downarrow\right\rangle$ and $\left|2\downarrow, n_\downarrow\right\rangle$. The error bars are smaller than the dots. The grey curve is a linear fit. (b) Variation of the effective Rabi frequency as a function of the microwave frequency detuning from the transition between $\left|1\uparrow, n_\downarrow\right\rangle$ and $\left|2\downarrow, n_\downarrow\right\rangle$ (orange dots). The grey curve is a fit of the form $\sqrt{\Omega^2+\delta^2}$, where Ω is the bare Rabi frequency and δ is the detuning. In (a) and (b), the error bars correspond to the standard error on the Rabi frequencies from fits by an exponentially decaying sine function.

homogeneous and/or fast microwave control, in particular on timescales beyond the rotating wave approximation [173, 174].

4.5 Master equation model

In order to model the Rabi oscillations and understand the dynamics involved in the presence of a microwave pulse, we develop an eight-level master equation in Lindblad form [161]. The eight levels considered encompass both orbital branches of the ground state, each split into two by the electronic Zeeman interaction, and further split by the hyperfine interaction. This leads to the energy level diagram depicted in Fig. 4.10, where states, labelled from 0 to 7 for convenience, are characterised by their electronic and nuclear spin projections. The various transition mechanisms between those states, as shown in Fig. 4.10, are described in the following.

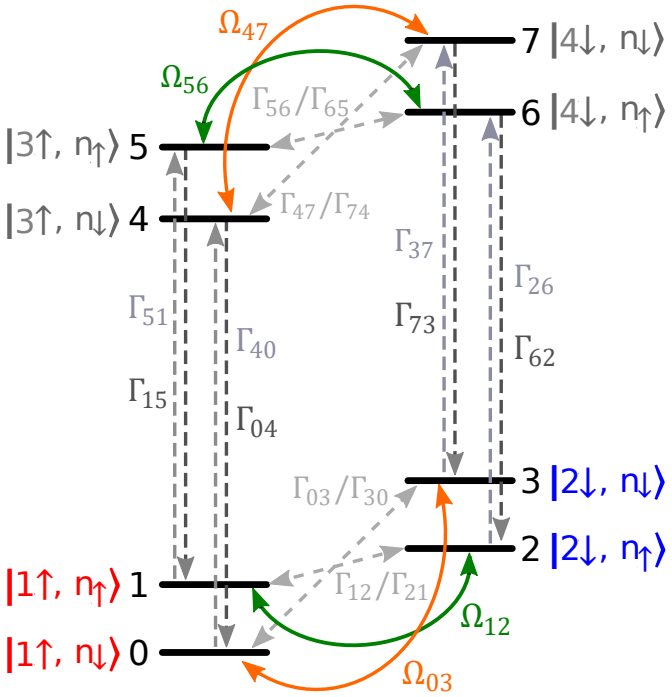

Figure 4.10 Diagram of the eight energy levels of the ground state (energy splittings are not to scale). Each state is labelled according to the labelling in Fig. 4.3, with the indication of the electronic and nuclear spin orientations at around 0.2 T. A second labelling from 0 to 7 is introduced for convenience in the master equation model. The lower orbital branch is composed of the levels labelled from 0 to 3 and the upper orbital branch is formed by the levels labelled from 4 to 7. The transitions between states considered in the model are of two kinds: the Rabi frequencies Ω_{ij} between states i and j are depicted as orange and green double arrows (colours correspond to those in Fig. 4.7b) and the population decays Γ_{ij} from state i to state j are represented by dashed grey arrows, whose relative colour intensities are a rough indication of their relative strengths.

The model consists in solving the following master equation:

$$\frac{\mathrm{d}\rho}{\mathrm{d}t} = \frac{i}{\hbar}[\rho, \mathcal{H}] + \mathcal{L}(\rho) \tag{4.2}$$

where ρ is the density matrix for the SiV$^-$ states considered, $\hbar$ is the reduced Planck constant, $\mathcal{H}$ is the Hamiltonian of the system formed by the SiV$^-$ levels considered and the microwave field in the rotating frame, and $\mathcal{L}(\rho)$ is the Lindblad superoperator. The Hamiltonian of the system in the rotating-wave approximation can be written as follows:

$$\mathcal{H} = \begin{pmatrix} E_0+\omega & 0 & 0 & \Omega_{03}/2 & 0 & 0 & 0 & 0 \\ 0 & E_1+\omega & \Omega_{12}/2 & 0 & 0 & 0 & 0 & 0 \\ 0 & \Omega_{03}/2 & E_2 & 0 & 0 & 0 & 0 & 0 \\ \Omega_{03}/2 & 0 & 0 & E_3 & 0 & 0 & 0 & 0 \\ 0 & 0 & 0 & 0 & E_4+\omega & 0 & 0 & \Omega_{47}/2 \\ 0 & 0 & 0 & 0 & 0 & E_5+\omega & \Omega_{56}/2 & 0 \\ 0 & 0 & 0 & 0 & 0 & \Omega_{56}/2 & E_6 & 0 \\ 0 & 0 & 0 & 0 & \Omega_{47}/2 & 0 & 0 & E_7 \end{pmatrix} \tag{4.3}$$

where E_i are the energies of the eight levels considered, Ω_{ij} are the Rabi frequencies between levels i and j, and ω is the frequency of the microwave. The state labelled 0 is taken as the origin of the energy scale. The energies of the other levels in the ground state lower branch are determined from the ODMR spectrum at the applied magnetic field of 0.214 T at which Rabi oscillations in Fig. 4.8 are measured:

$$E_0 = 0\,\mathrm{GHz} \tag{4.4}$$

$$E_1 = 2\pi \cdot 0.027\,\mathrm{GHz} \tag{4.5}$$

$$E_2 = 2\pi \cdot 2.899\,\mathrm{GHz} \tag{4.6}$$

$$E_3 = 2\pi \cdot 2.926\,\mathrm{GHz} \tag{4.7}$$

The energies of the levels in the upper branch are extracted from the group theoretical modelling of the optical transitions in Section 4.1.3 (more explanantion on the modelling of the hyperfine interaction can be found in Chapter 5 Section 5.1):

$$E_4 = 2\pi \cdot 51.61\,\mathrm{GHz} \tag{4.8}$$

$$E_5 = 2\pi \cdot 51.63\,\mathrm{GHz} \tag{4.9}$$

$$E_6 = 2\pi \cdot 54.24\,\mathrm{GHz} \tag{4.10}$$

$$E_7 = 2\pi \cdot 54.26\,\mathrm{GHz} \tag{4.11}$$

The microwave-induced bare Rabi frequencies are extracted from the Rabi oscillation curves fitted by a sine function with an exponential decay:

$$\Omega_{12} = 2\pi \cdot 14.7\,\mathrm{MHz} \tag{4.12}$$

$$\Omega_{03} = 2\pi \cdot 14.4\,\mathrm{MHz} \tag{4.13}$$

The bare Rabi frequencies in the upper branch are assumed to be similar with $\Omega_{47} = \Omega_{56} = 2\pi \cdot 14.5\,\mathrm{MHz}$.

The Lindblad superoperator, accounting for the relaxation mechanisms linked to the coupling of the SiV^- with its environment, is of the form:

$$\mathcal{L}(\rho) = \sum_{i,j} \mathcal{L}_{ij}(\rho) = -\frac{1}{2}\sum_{i,j}\left(C_{ij}^{\dagger}C_{ij}\rho + \rho C_{ij}^{\dagger}C_{ij}\right) + \sum_{i,j} C_{ij}\rho C_{ij}^{\dagger} \tag{4.14}$$

with the collapse operators $C_{ij} = \sqrt{\Gamma_{ij}}\,|j\rangle\langle i|$ describing the relaxation from state $|i\rangle$ to state $|j\rangle$ with decay rate Γ_{ij}. The electronic spin decay rates within the lower branch are directly linked to the spin population decay time $T_{1,spin}$ through:

$$\Gamma = \frac{1}{2T_{1,spin}} \tag{4.15}$$

All the electronic spin decay rates in the lower branch of the ground state are assumed to be equal, thus giving:

$$\Gamma_{03} = \Gamma_{30} = \Gamma_{12} = \Gamma_{21} = 1.39\,\mathrm{MHz} \tag{4.16}$$

The corresponding decays within the upper branch are assumed equal to those in the lower branch, leading to:

$$\Gamma_{47} = \Gamma_{74} = \Gamma_{56} = \Gamma_{65} = 1.39\,\mathrm{MHz} \tag{4.17}$$

The microwave-induced heating, and hence the sample temperature, increase linearly with the microwave pulse duration. As will be developed in Chapter 5 Section 5.2, the spin population decay time decreases with temperature. This effect is accounted for in the model by adjusting the value of the spin decay rates with respect to the temperature measured for a given pulse duration.

Since at temperatures around 4 K, the upper orbital branch of the ground state is thermally populated, population transfers from one orbital branch to the other have

to be taken into account. We first consider the interbranch downward and upward rates, Γ_{down} and Γ_{up} respectively, where both electronic and nuclear spin orientations are preserved. Those rates are directly linked to the orbital population decay time $T_{1,orbital}$ through:

$$\frac{1}{T_{1,orbital}} = \Gamma_{up} + \Gamma_{down} \tag{4.18}$$

with $\Gamma_{up} = \Gamma_{down} \cdot e^{\frac{-\Delta E}{k_B T}}$ where k_B is the Boltzmann constant and ΔE is the energy difference between the lower and upper branches, taken to be approximately 52.4 GHz. This guarantees a Boltzmann population distribution between the lower and upper orbital branches. The downward rates associated with all the spin-preserving interbranch transitions are assumed equal, thus giving:

$$\Gamma_{51} = \Gamma_{40} = \Gamma_{73} = \Gamma_{62} = \frac{1}{T_{1,orbital}\left(1 + e^{\frac{-\Delta E}{k_B T}}\right)} \tag{4.19}$$

And similarly for the upward rates:

$$\Gamma_{15} = \Gamma_{04} = \Gamma_{37} = \Gamma_{26} = \frac{e^{\frac{-\Delta E}{k_B T}}}{T_{1,orbital}\left(1 + e^{\frac{-\Delta E}{k_B T}}\right)} \tag{4.20}$$

Due to the Boltzmann factor, those rates vary with temperature, depending on the microwave pulse duration. Furthermore, $T_{1,orbital}$ itself decreases with temperature, effect which will be examined in Chapter 5 Section 5.2. The rates in the model are thus adjusted to account for the microwave-induced heating of the sample, using the measured temperature increase with respect to the pulse duration.

The other interbranch rates, more precisely those associated with electron spin-flipping transitions as well as all nuclear spin-flipping transitions, are considered negligible compared to the spin-preserving rates.

The initial conditions of populations in the different states immediately after initialisation are as follows:

$$\rho_{00} = \rho_{11} = 0.5 * (1 - \mathcal{I}) * 1 / \left(1 + e^{\frac{-\Delta E}{k_B T}}\right) \tag{4.21}$$

$$\rho_{22} = \rho_{33} = 0.5 * \mathcal{I} * 1 / \left(1 + e^{\frac{-\Delta E}{k_B T}}\right) \tag{4.22}$$

$$\rho_{44} = \rho_{55} = 0.5 * (1 - \mathcal{I}) * e^{\frac{-\Delta E}{k_B T}} / \left(1 + e^{\frac{-\Delta E}{k_B T}}\right) \tag{4.23}$$

$$\rho_{66} = \rho_{77} = 0.5 * \mathcal{I} * e^{\frac{-\Delta E}{k_B T}} / \left(1 + e^{\frac{-\Delta E}{k_B T}}\right) \tag{4.24}$$

where ρ_{ii} is the density matrix element corresponding to the population in state i. The factors $1/\left(1 + e^{\frac{-\Delta E}{k_B T}}\right)$ for states in the lower orbital branch and $e^{\frac{-\Delta E}{k_B T}} / \left(1 + e^{\frac{-\Delta E}{k_B T}}\right)$ for states in the upper orbital branch ensure an initial Boltzmann population distribution between the two branches. This is an approximation since the microwave pulse starts about 10 ns after the end of the optical initialisation pulse, but it takes a few tens of nanoseconds for the orbital population decay (quantified by $T_{1,orbital}$) to restore a Boltzmann distribution. Pairs of states differing only by their nuclear spin projections (namely 0 and 1, 2 and 3, 4 and 5, 6 and 7) are assumed to have the same initial populations. As a consequence, a factor 0.5 is applied to the populations of each pair to ensure that their sum is equal to the population of an equivalent single energy level. Finally, $\mathcal{I}$ corresponds to the initialisation fidelity into states with an electronic spin down (namely states 2 and 3 in the lower branch, 6 and 7 in the upper branch), resulting in a factor $1 - \mathcal{I}$ for the populations of the other states. The value of $\mathcal{I}$ is considered as an adjustable parameter. The best fit to the experimental curve is obtained with a value of $86 \pm 2\,\%$, in agreement with the value obtained from the optical pumping signal.

The master equation is solved numerically in time over a total duration of 200 ns, corresponding to the experimental delay between the start of the microwave pulse following initialisation and the optical readout pulse. An example is given in Fig. 4.11, for a microwave pulse of 100 ns resonant with the transition between states 1 and 2 and thus detuned from the other possible transitions in both orbital branches, as illustrated in Fig. 4.11a. Figure 4.11b shows the populations of the four states in the upper (top panel) and in the lower (bottom panel) orbital branches plotted as a function of time. In the lower orbital branch, the populations of states 1 and 2 display Rabi oscillations during the microwave pulse while simultaneously decaying on a timescale of $T_{1,spin}$.

Once the microwave is off, Rabi oscillations cease and the populations keep on decaying according to $T_{1,spin}$.

States 0 and 3, for which the microwave frequency is detuned by about 54 MHz, are also driven by the microwave and display oscillations of smaller amplitude and faster effective Rabi frequency in accordance with this detuning. They also experience population decay due to $T_{1,spin}$.

In the upper orbital branch of the ground state, due to different level splittings, the microwave is detuned from both possible transitions by more than 200 MHz and the detunings are thus too large for the microwave to induce sizeable Rabi oscillations. In the case of states 5 and 6, oscillations arise with a similar frequency to those between states 1 and 2 with a slight delay due to the spin-preserving orbital transitions between states 1 and 5 and states 2 and 6, denoted $\Gamma_{15/51}$ and $\Gamma_{26/62}$ in the model and Fig. 4.10. The timescale of this population transfer is approximately 50 ns, which is comparable to the 34 ns half-period of the oscillations in states 1 and 2. This transfer is fast enough to induce oscillations into states 5 and 6, but too slow for it to be approximated as immediate, thus leading to a delay compared to the oscillations in 1 and 2. This delay causes the oscillations in 5 and 6 to decrease in amplitude as dephasing is accumulated, an effect which, added to the $T_{1,spin}$-related decay, leads to a faster population decay in 5 and 6 compared to 4 and 7. Reciprocally, the populations in 1 and 2 decay faster than those in 0 and 3 because of the orbital transfer from 5 and 6. It should be noted that, although less obvious, the same spin-preserving orbital population transfer occurs between 0 and 4 and between 3 and 7 on the same timescale. However, due to the detuning of the microwave frequency with the transition between 0 and 4, the impact of the dephasing arising from the orbital transfer of the Rabi oscillations is reduced.

In order to simulate the experiment, where readout is performed after 200 ns after the start of the microwave pulse, we solve the master equation for times up to 200 ns for different durations of microwave pulse. The populations at 200 ns (indicated by dots in Fig. 4.11b) are then plotted as a function of the microwave pulse duration. The simulation for a microwave resonant with the transition between states 1 and 2 (see Fig. 4.12a), is shown in Fig. 4.12b. Here, the effect of the orbital population transfer appears more clearly for the four states of the upper orbital branch, which follow the evolutions of those in the lower branch. The decay of the oscillations is mainly caused by the orbital transfers between the two branches, as longer microwave pulses lead to the accumulation of more dephasing, in agreement with the faster decay in time of the resonantly driven states 1 and 2 compared to 0 and 3. As the microwave

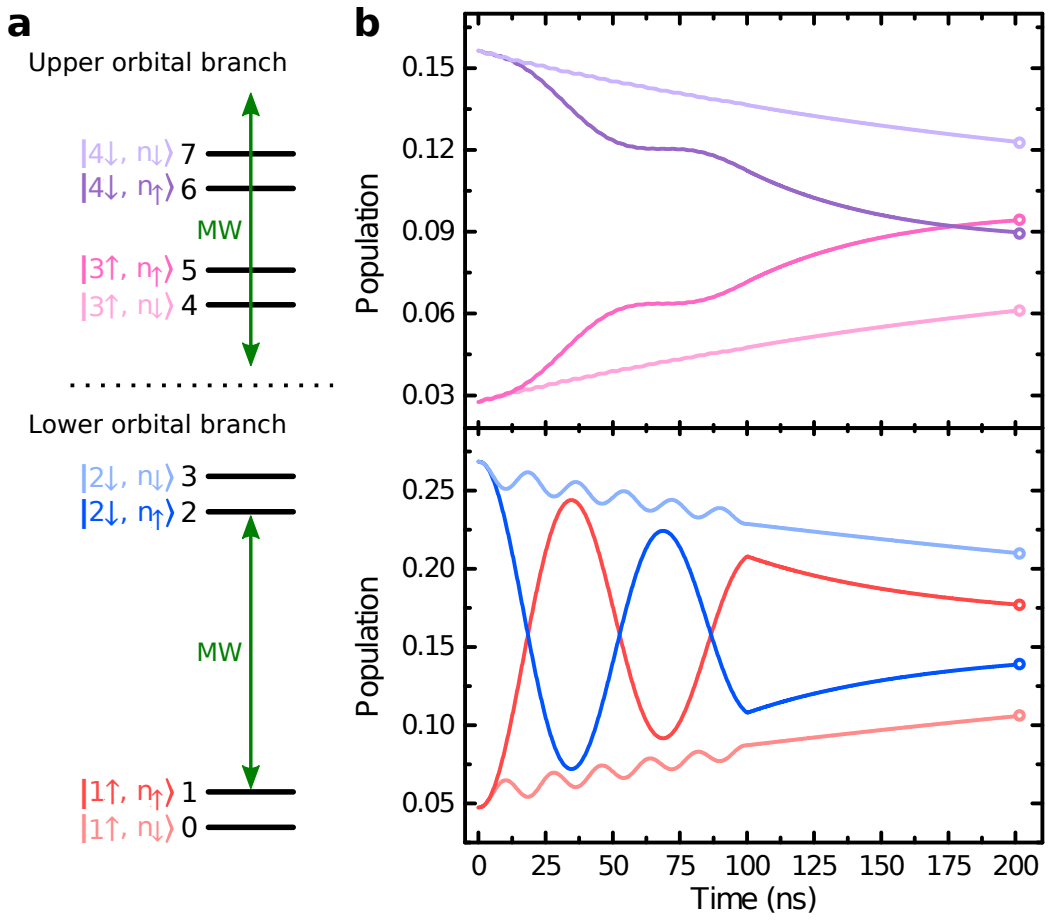

Figure 4.11 Solution in time of the master equation. (a) Diagram of the energy levels in the upper and lower branches of the ground state. The microwave is taken in resonance with the transition between states 1 and 2 and is thus detuned from all the other possible transitions in the lower and upper branches, in accordance with the energy splittings in Eqs. 4.4 to 4.11. (b) Simulated evolution in time of the populations of the upper orbital branch levels (top panel) and of the lower orbital branch levels (bottom panel) for a 100 ns microwave pulse. The colours correspond to those in (a). The final populations at 200 ns corresponding to the experimental readout time are indicated by circles.

pulse duration is increased, the temperature of the sample rises, which leads to the decrease of $T_{1,spin}$ and $T_{1,orbital}$. The former is responsible for the populations within each orbital branch converging faster and faster towards thermal equilibrium as the pulse duration is increased, despite the delay between initialisation and readout being held constant. The latter increases slightly the decay rate of the oscillations. The Boltzmann factors in the orbital transfer rates lead to the general upward population

shift in the upper orbital and to the downward shift in the lower one, and increase more significantly the decay of the oscillations.

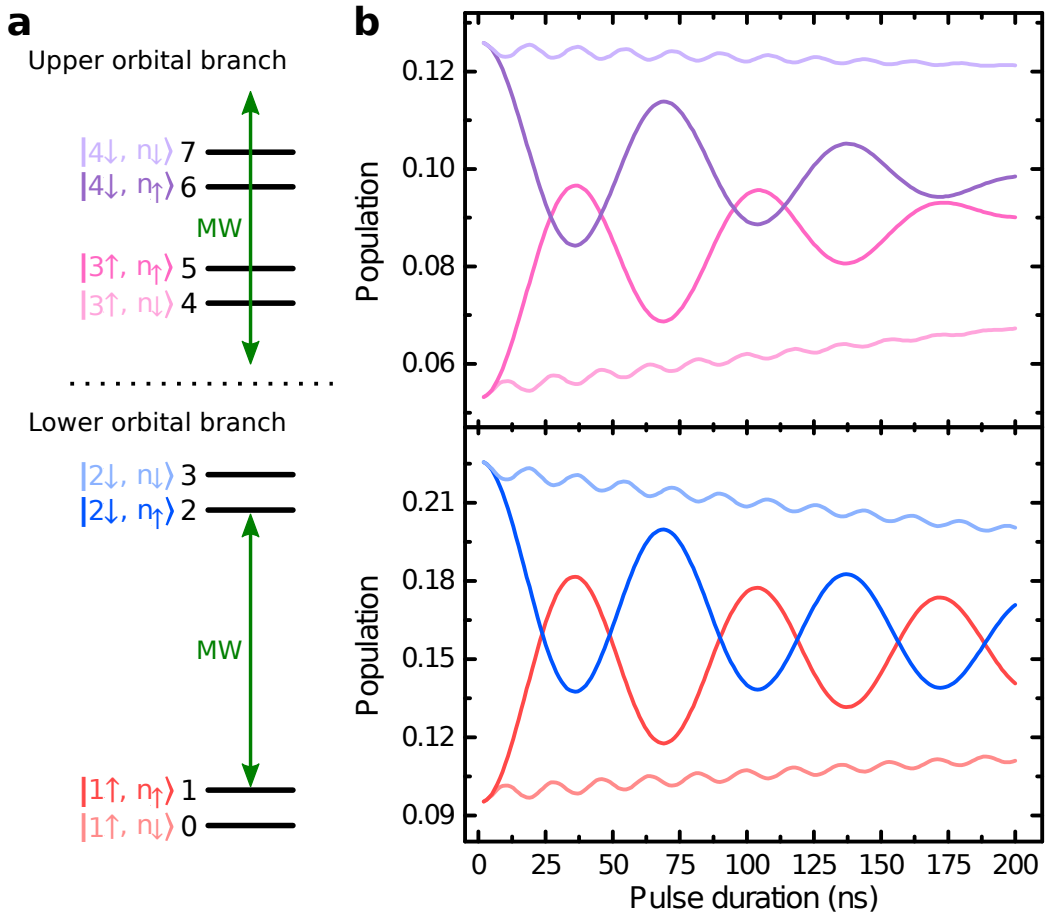

Figure 4.12 Simulation of Rabi oscillations. (a) Diagram of the energy levels in the upper and lower branches of the ground state. The microwave is taken in resonance with the transition between states 1 and 2 and is thus detuned from all the other possible transitions in the lower and upper branches, in accordance with the energy splittings in Eqs. 4.4 to 4.11. (b) Simulated evolution of the level populations at 200 ns as a function of the microwave pulse duration for the upper orbital branch levels (top panel) and the lower orbital branch levels (bottom panel). The colours correspond to those in (a).

Experimentally, the spin state is read out through a laser pulse resonant with transition D1. In this model, this corresponds to reading out the populations in the hyperfine levels labelled 0 and 1, as they are only 27 MHz apart and the optical linewidth of the transition is about 600 MHz in the absence of power broadening. In order to reproduce the experimental values of the peak ratio where the peak of the readout pulse is divided by that of the initialisation pulse, the sum of the final

populations in states 0 and 1 is divided by the sum of their initial populations. The resulting simulated Rabi oscillation curves are displayed in Fig. 4.13 and superimposed with the experimental data points. The good agreement between the simulated curves and the experimental data points confirms that the master equation model we have developed captures most of the dynamics of the system. From the analysis of the model, we can conclude that the upward drift of the experimental curve is a consequence of the orbital transfers between the two branches of the ground state combined with the microwave heating-induced increase in orbital transfers and spin decay rates. The progressive decrease in amplitude of the oscillations can be described entirely by the spin-preserving orbital transfers between the two branches of the ground state without introducing any other source of dephasing.

4.6 Ramsey interferometry

We now make use of the coherent control over the SiV^- spin to obtain a direct measurement of its dephasing time T_2^*, corresponding to the duration beyond which the phase ϕ in the superposition $|\uparrow\rangle + e^{i\phi}|\downarrow\rangle$ is randomised by noise. To this end, we implement Ramsey interferometry [175, 154], with a pulse sequence consisting of two $\pi/2$ microwave pulses (see Subsection 3.1.1 for the definition of a $\pi/2$-pulse) separated by a variable delay, as illustrated in Fig. 4.14a.

The frequency of the microwave is first fixed such that its detuning from the transition between nuclear spin-up levels is twice that from the transition between nuclear spin-down levels (36 MHz and 18 MHz, respectively), as illustrated in Fig. 4.14b left panel. The obtained evolution of the peak ratio as a function of the free precession interval between the two $\pi/2$-pulses is shown in Fig. 4.14b right panel. The frequency of the Ramsey fringes is equal to the detuning of the microwave frequency from a given transition [154]. As a consequence, the oscillations due to the transition between nuclear spin-up levels have twice the frequency of those associated with the transition between nuclear spin-down levels. This results in a beating in the overall signal, as observed experimentally.

We repeat the same measurement with the frequency of the microwave detuned by the same amount from both transitions so that both oscillations have the same frequency and thus add constructively, as illustrated in Fig. 4.14c left panel. The obtained signal is shown in Fig. 4.14c right panel and can be fitted by a simple function of the form $\cos(2\pi\delta\tau)\exp(-\tau/T_2^*)$, where δ is the common detuning of the microwave

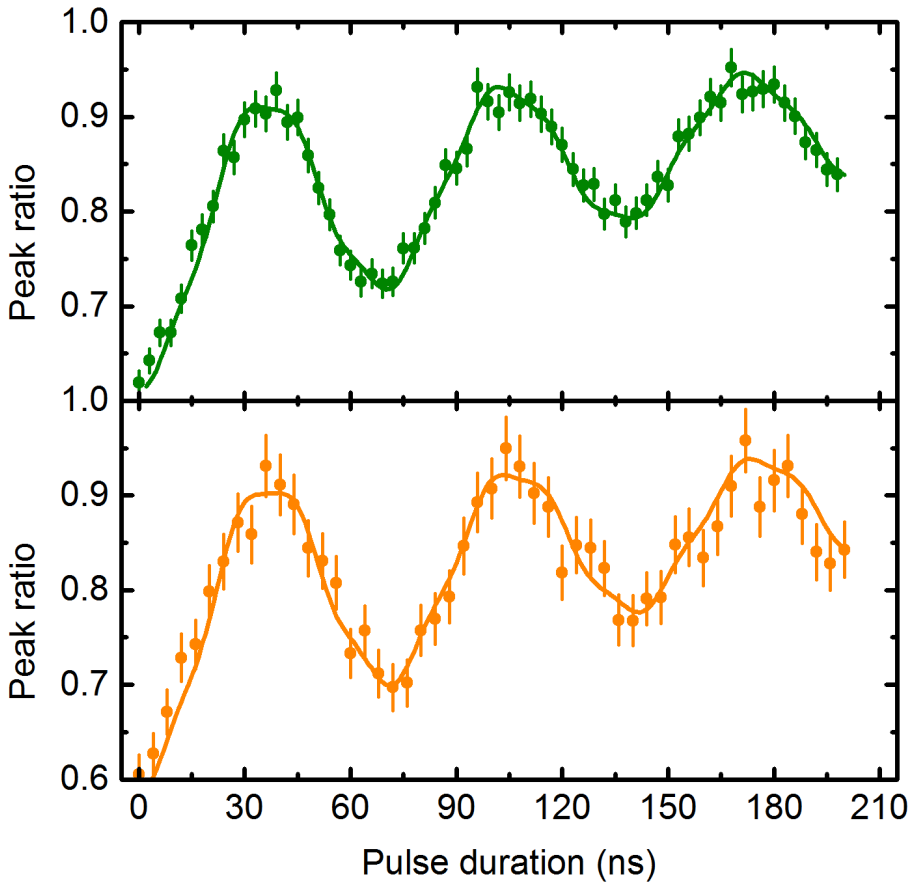

Figure 4.13 Comparison between experimental and simulated Rabi oscillations. The sum of the simulated populations at 200 ns for levels 0 and 1, normalised to the sum of their initial populations at 0 ns, is plotted as solid curves for a microwave resonant with the transition between states 1 ($\left|1\uparrow, n_\uparrow\right\rangle$) and 2 ($\left|2\downarrow, n_\uparrow\right\rangle$) (green curve) and between states 0 ($\left|1\uparrow, n_\downarrow\right\rangle$) and 3 ($\left|2\downarrow, n_\downarrow\right\rangle$) (orange curve). The corresponding experimental data points from Fig. 4.8 are plotted for comparison.

pulses with both transitions and τ is the free precession interval. We thus obtain a direct measurement of the dephasing time of the electronic spin $T_2^* = 115 \pm 9$ ns at 3.6 K. This value is significantly larger than the 45 ns extracted from the CPT measurements. While during a Ramsey measurement, the spin is left to evolve freely between microwave pulses, a CPT experiment relies on constant driving of the system by two laser fields which induce dephasing through noise, as discussed in Section 3.4. Ramsey interferometry thus provides a more reliable measurement. However, the CPT model used to extract the dephasing time takes into account the extra dephasing from the lasers. The discrepancy between the CPT and Ramsey results is due to

the fact that the SiV^- used for CPT was slightly strained, unlike the one used for Ramsey interferometry. The reason for this difference will be developed in Chapter 5 Sections 5.2 and 5.3.

4.7 Conclusion

We have evidenced a direct interaction between a single SiV^- centre and a microwave field. Through the realisation of optically detected magnetic resonance, we have been able to identify the spin-flipping transitions which can be efficiently driven by microwave. We have then achieved coherent control of the SiV^- electronic spin using microwave pulses. Such a control is demonstrated for both ^{29}Si nuclear spin states, making it possible to use the nuclear spin as a second qubit and take advantage of its likely much longer coherence times. The coherent control by microwave does not rely on any particular orientation of the magnetic field, thus giving more flexibility than all-optical control for which a Λ-scheme is necessary. In particular, bringing the magnetic field close to alignment with the SiV symmetry axis would provide several advantages. Firstly, it would increase considerably the spin decay time $T_{1,spin}$, with values reaching more than 2 ms [171]. Secondly, due to the spin quantisation axis being the same in the ground and excited states, optical transitions between states of different spin orientations are forbidden as shown in Chapter 2 Section 2.5. It would thus be possible to take advantage of the spin-cycling transitions for single-shot readout of the SiV^- spin state [176, 177], which would be a key ingredient for many quantum information protocols, such as deterministic teleportation and quantum error correction [1, 178]. Finally, the combination of the optical qualities of the SiV^- with the microwave addressing of some of its states makes the SiV^- a promising system to be used as a quantum transducer between optical and microwave photons [179]. This would be of particular interest in hybrid architectures combining the scalability of superconducting qubits which operate in the microwave regime and the low losses in optical communications for long-distance information transfer. The value of the spin dephasing time appears relatively modest even for solid-state qubits [30, 40, 180–182], and in particular compared to that of the NV^- centre, where the dephasing times are measured in the range of milliseconds [183, 184] and even approaching a second [185]. A very recent EPR measurement on SiV^0 reports a dephasing time of more than 100 µs at cryogenic temperatures [186]. It is thus necessary to investigate the causes for such a short coherence time in order to improve it.

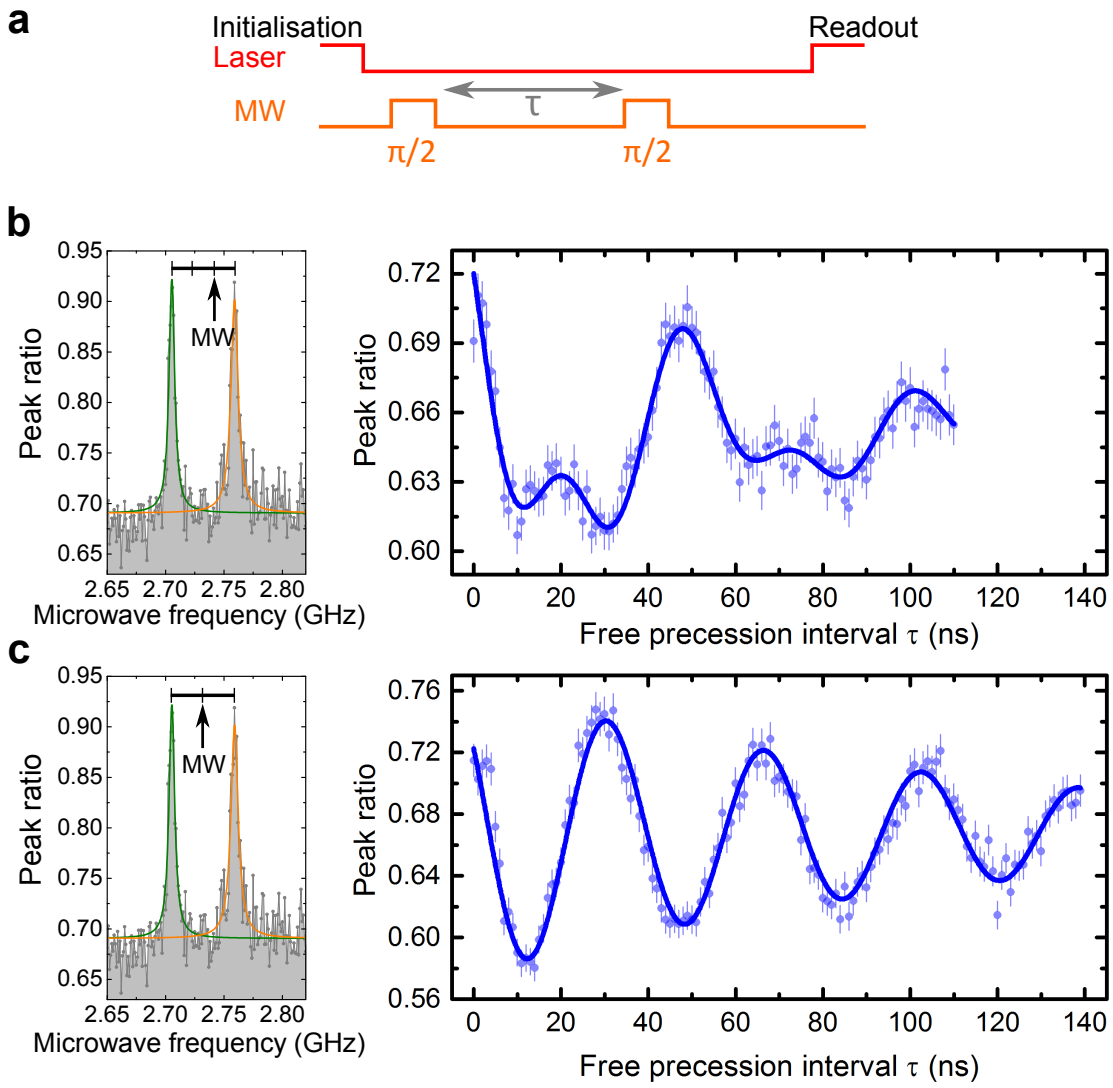

Figure 4.14 Ramsey interferometry. (a) Ramsey sequence: two microwave $\pi/2$ pulses, each corresponding to a duration of 8 ns, are separated by a variable delay τ. The delay between optical initialisation and readout pulses is held constant at 160 ns not to include the effect of the spin decay into the measured signal. (b) Ramsey oscillations (blue dots) for a microwave frequency detuned by $\delta_1 = 36$ MHz from the transition between nuclear spin-up levels and by $\delta_2 = 18$ MHz from the transition between nuclear spin-down levels, as indicated in the ODMR spectrum on the left. The Ramsey oscillations are fitted with a function of the form $(A_1 \cos(2\pi\tau\delta_1) + A_2 \cos(2\pi\tau\delta_2)) \exp(-\tau/T_2^*)$, where A_1 and A_2 are the amplitudes of the respective oscillations and T_2^* is the spin dephasing time. The fit is diplayed as a solid blue curve. (c) Ramsey oscillations at 3.6 K (blue dots) for a microwave frequency detuned by $\delta = 27$ MHz from both transitions, as indicated in the ODMR spectrum on the left. The Ramsey oscillations are fitted with a function of the form $A \cos(2\pi\tau\delta) \exp(-\tau/T_2^*))$, where A is the amplitude of the oscillations and $T_2^* = 115 \pm 9$ ns is the spin dephasing time. The fit is diplayed as a solid blue curve.

Chapter 5

Interactions with the environment

The advantage of solid-state systems over trapped atoms in terms of scalability have to be balanced against decoherence which arises when any quantum system is surrounded by an environment with which it interacts. However, by understanding these interactions, we can devise ways to mitigate them. In addition, some of theses interactions can actually be taken advantage of, as they provide additional resources for quantum information processing.

In this chapter, we explore the interactions of the SiV^- centre with three particular elements of its environment, namely a single nuclear spin, lattice phonons and strain, and evaluate their impact on the properties of the SiV− as a quantum bit. Those results were obtained with the technical assistance of David-Dominik Jarausch, Christian Hepp, Lina Klintberg and Jonas N. Becker for the nuclear spin and lattice phonons parts, and have been published in Ref. [166], and the data of the strain part were taken together with Tina Müller and partially published in Ref. [144].

5.1 ^{29}Si silicon-vacancy centres: coupling to the nuclear spin

^{28}Si is by far the most common isotope of silicon, with a natural abundance of 92.3 %. However, it does not possess a nuclear spin. As a consequence, in order to investigate the hyperfine interaction of an SiV^- with a nuclear spin, we have implanted a diamond sample with $^{29}Si^+$ ions, which possess a nuclear spin $I = 1/2$. The details of the sample preparation and experimental equipment are the same as those described in Chapter 4 Section 4.1.

We aim to explore the coupling strength of the SiV^- electronic spin with the nuclear spin of its ^{29}Si atom. To this end, we need to lift the spin degeneracy with an external magnetic field, which is here oriented with an angle of $109.5 \pm 1.0°$. We investigate the low magnetic field regime (around 0.2 T) using optically detected magnetic resonance. As described in Chapter 4 Section 4.3, the ODMR spectrum displays two resonances, each corresponding to a transition between states of opposite electronic spin with the nuclear spin remaining unchanged, up or down (as illustrated in Fig. 5.1 inset). We measure the frequencies of those two resonances at different values of the applied magnetic field, as shown in Fig. 5.1 as orange and green dots. The resonance frequencies shift with the magnetic field while maintaining a constant separation of 53.7 ± 0.3 MHz between them. This corresponds to a hyperfine splitting of the states of approximately 27 MHz.

In order to extract information about the hyperfine coupling, we fit the observed frequency shift using the group theoretical model described in Chapter 2 Section 2.4. The parameters of the Hamiltonians of the Jahn-Teller effect, of the spin-orbit coupling and of the Zeeman effect are deduced by fitting the evolution of the optical transitions predicted by the model as a function of the external magnetic field with the corresponding experimental measurement, as was shown in Fig. 4.2. From this, we have deduced the relative energies of the electronic states of the SiV^- (see Fig. 4.3).

This model is here expanded to include interactions due to the ^{29}Si nuclear spin $I = 1/2$. The hyperfine interaction between the nuclear spin $\vec{I}$ and the SiV^- electron spin $\vec{S}$ is of the form $\mathcal{H}_{HF} = \vec{I} \cdot \bar{A} \cdot \vec{S}$, with $\bar{A}$ the hyperfine coupling tensor. The hyperfine coupling can be separated into parallel $A_\parallel$ and orthogonal $A_\perp$ components with respect to the main symmetry axis of the SiV^- centre [187]. This leads to the following expression: $\mathcal{H}_{HF} = A_\parallel S_z I_z + A_\perp (S_x I_x + S_y I_y)$. The orbital contribution to the hyperfine coupling is thought to be minor as the hyperfine coupling measured by EPR is close to isotropic [187]. The nuclear Zeeman interaction is included with: $\mathcal{H}_{nZee} = -\frac{g_{^{29}Si}\mu_n}{\hbar} \vec{I} \cdot \vec{B}$, where $\mu_n = 7.6\,\mathrm{MHz\,T^{-1}}$ is the nuclear magneton and $g_{^{29}Si} = -1.11$ is the nuclear Landé factor for ^{29}Si [188]. We fit the measured transition frequencies from the ODMR spectra with the energy differences of the hyperfine levels from the model. This is shown in Fig. 5.1 as orange and green solid curves, the two dashed grey curves corresponding to the transitions where the nuclear spin is flipped. In this way, we can extract a value for $A_\parallel = 70 \pm 2$ MHz, in agreement with the previously reported values [187, 171] as well as theoretical predictions [96]. At the low magnetic fields studied here (approximately 0.2 T), the quantisation axes for the electron and

nuclear spins remain dictated by the spin-orbit coupling and the hyperfine interaction respectively, and are both close to alignment with the symmetry axis of the SiV^-. Thus, $A_\perp$ has little influence on the measured hyperfine splitting in this configuration.

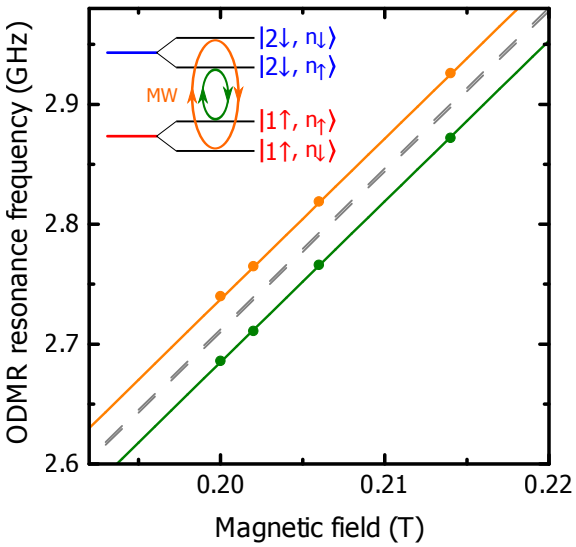

Figure 5.1 Magnetic field dependence of ODMR resonances. (Inset) Energy level diagram of the electronic spin states in the ground state lower orbital branch split by the hyperfine interaction with the ^{29}Si $I = 1/2$ nuclear spin. The levels are labelled as in Fig. 4.3, with the addition of the electronic spin orientations at around 0.2 T. An applied microwave can flip the electronic spin while leaving the nuclear spin unchanged, which results in two possible microwave-induced transitions (orange and green circular arrows). (Main figure) Variation of the ODMR resonances with the applied magnetic field (orange and green dots). The frequencies of the resonances are determined through Lorentzian fits of the resonance peaks of the ODMR spectra (colours correspond to those in the inset). Errors are smaller than dots. The curves correspond to the splittings between the energy levels considered, as simulated by the group theoretical model expanded to include the nuclear spin. Orange and green curves correspond to the transitions indicated in the inset, the two overlapping grey dashed curves correspond to the transitions where both electronic and nuclear spins are flipped.

5.2 Single phonon-mediated spin dephasing and decay

We have seen in Chapter 4 Section 4.5 how transitions between the two orbital branches of the ground state play an important role in the electronic spin dynamics of the SiV^-

centre. We here investigate more closely those transitions and their impact on the spin coherence.

5.2.1 Spin dephasing

At around 4 K, both orbital branches of the ground state are populated following a Boltzmann distribution. This population is a direct consequence of transitions taking place between those two orbital branches. We investigate the dynamics of those transitions using the same SiV^- centre and experimental setup as those described in Section 4.1. In the absence of magnetic field, the spin sublevels are degenerate and only the orbital branches can be addressed (see Fig. 5.2a). We measure the orbital decay time $T_{1,orbital}$ through a pump-probe experiment, analogous to that used to measure the spin decay time $T_{1,spin}$ and described in Section 4.2. A first 500 ns optical pulse resonant with transition β depletes the population in the upper orbital branch of the ground state and initialises the SiV^- into the lower ground state orbital branch through optical pumping, as shown in Fig. 5.2b. After a time delay, a second 500 ns optical pulse resonant with transition β measures the population recovery into the upper ground state orbital branch. By varying the time delay between the pulses, we measure an exponential recovery of the orbital population whose fit allows us to extract a value of $T_{1,orbital} = 70 \pm 3$ ns at 3.5 K, as shown in Fig. 5.2.

Considering that lattice phonons are the most likely cause of these orbital transitions, it is necessary to investigate how $T_{1,orbital}$ is affected by temperature. Figure 5.3 displays the variation of the transition rate $1/(2T_{1,orbital})$ as a function of the measured temperature. The observed linear dependence indicates that orbital transitions result from the absorption (upward transition) and emission (downward transition) of a single phonon resonant with the orbital transition [130]. To reach this conclusion, Jahnke *et al.* [130] consider a linear interaction between the E-symmetric ground state orbitals and E-symmetric phonon modes. To first-order, they obtain the following upward and downward transition rates:

$$\Gamma_{up} = 2\pi \sum_k n_{-,k} \left|\chi_k\right|^2 \delta\left(\Delta E, \omega_k\right) \tag{5.1}$$

$$\Gamma_{down} = 2\pi \sum_k \left(n_{+,k} + 1\right) \left|\chi_k\right|^2 \delta\left(\Delta E, \omega_k\right) \tag{5.2}$$

where $n_{p,k}$ is the occupation of the acoustic mode of polarisation p and wavevector k, and $\left|\chi_k\right|^2$ is the coupling rate to a single phonon of wavevector k. Summing over all

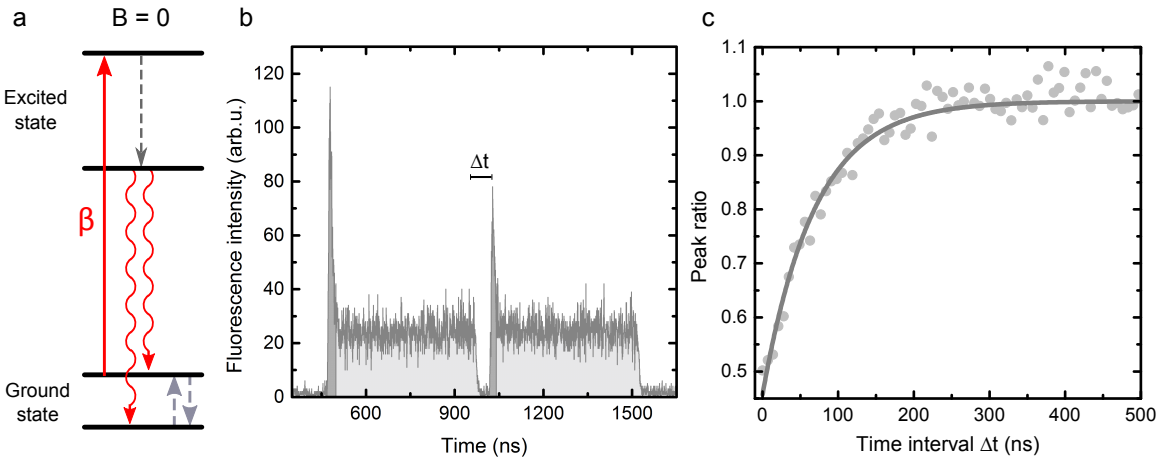

Figure 5.2 Measurement of the orbital decay time $T_{1,orbital}$ at 3.5 K in the absence of magnetic field by a pump-probe experiment. (a) Energy levels of the SiV^- at zero magnetic field. We excite transition β resonantly (red arrow) and measure the fluorescence from the lower branch of the excited state (wiggly red arrows). Dashed grey arrows represent phonon-induced thermalisation processes. (b) Temporal dependence of the fluorescence intensity during the initialisation pulse followed by the readout pulse, separated by a delay Δt. The signal displays a sharp decay indicating depletion of the population in the upper orbital branch of the ground state and optical pumping into the lower orbital branch. The fluorescence signal integrated to calculate the peak ratio (corresponding to the population in the upper orbital branch of the ground state) is indicated in dark grey. (c) Variation of the peak ratio as a function of the delay Δt between initialisation and readout (grey dots). The population recovery into the upper branch of the ground state is fitted with an exponential curve with time constant $T_{1,orbital} = 70 \pm 3$ ns.

available phonon modes leads to:

$$\Gamma_{up} = 2\pi\chi\rho(\Delta E)^3 n(\Delta E, T) \tag{5.3}$$

$$\Gamma_{down} = 2\pi\chi\rho(\Delta E)^3 (n(\Delta E, T) + 1) \tag{5.4}$$

with $\chi\Delta E$ the interaction frequency, $\rho(\Delta E)^2$ the density of modes and $n(\Delta E, T)$ the Bose-Einstein distribution. In Γ_{down}, the additional $+1$ in $(n(\Delta E, T) + 1)$ can be interpreted physically as the spontaneous emission of a phonon while $n(\Delta E, T)$ can be thought of as stimulated emission. A Taylor expansion of the Bose-Einstein distribution in T leads both rates to be linear in temperature.

As was evidenced by the master equation model for Rabi oscillations (see Section 4.5), transitions between orbital branches act as a dephasing mechanism for the spin of the SiV^-. To evaluate the link between orbital transitions and spin dephasing, we perform

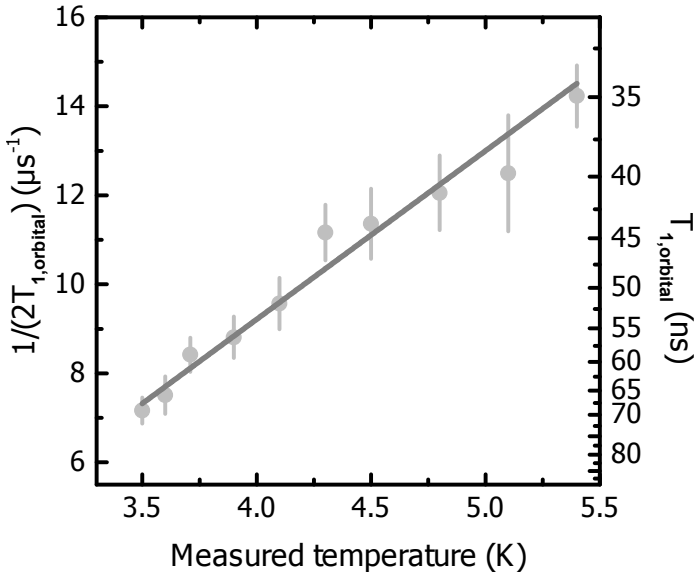

Figure 5.3 Temperature dependence of the orbital decay time $T_{1,orbital}$ in the ground state (grey dots). Error bars correspond to the standard error from the exponential fit of the population recovery. The solid grey curve is a linear fit with $1/(2T_{1,orbital})\,(\mathrm{MHz}) = (3.8 \pm 0.2)(\mathrm{MHz\,K^{-1}}) * T\,(\mathrm{K}) - (5.8 \pm 0.8)\,(\mathrm{MHz})$.

Ramsey interferometry on the electronic spin at various temperatures. Figure 5.4 shows the temperature dependence of the spin dephasing rate $1/T_2^*$. This dependence is plotted along that of the orbital transition rate $1/(2T_{1,orbital})$. We not only see that the dephasing rate varies linearly with temperature, but also that it follows $1/(2T_{1,orbital})$. This shows that single-phonon-induced excitations from the lower orbital branch to the upper one is a dominant cause of spin dephasing. Physically, this can be understood as follows. A superposition of spin in the lower ground state orbital branch can be excited by a single phonon resonant with the orbital splitting at about 50 GHz to the upper orbital branch. There, due to the different spin splitting between the two orbital branches, an extra phase is accumulated between the two components of the spin superposition, which thus leads to the dephasing of the spin state.

Considering this dephasing mechanism, the spin dephasing rate $1/T_2^*$ is to be compared to the upward transition rate Γ_{up} between orbital branches. At those low temperatures, the Boltzmann distribution of the population between the two orbital branches indicates that the upward transition rate Γ_{up} and downward transition rate Γ_{down} differ by a Boltzmann factor:

$$\Gamma_{up} = \Gamma_{down} \cdot e^{\frac{-\Delta E}{k_B T}} \tag{5.5}$$

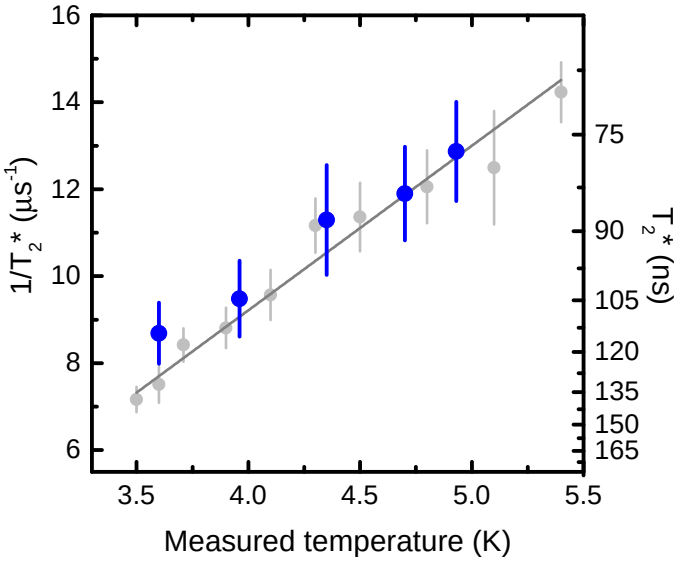

Figure 5.4 Temperature dependence of the spin dephasing rate $1/T_2^*$ (blue dots) determined by Ramsey interferometry (as described in Section 4.6). Error bars correspond to the standard errors from the cosine fits of the Ramsey signals. The values and linear fit of $1/(2T_{1,orbital})$ from Fig. 5.3 are displayed as grey dots an grey curve, respectively.

with $\frac{1}{T_{1,orbital}} = \Gamma_{up} + \Gamma_{down}$ where k_B is the Boltzmann constant and $\Delta E \approx 50\,\mathrm{GHz}$ is the energy difference between the lower and upper branches. We thus obtain:

$$\Gamma_{up} = \frac{1}{T_{1,orbital}\left(1 + e^{\frac{\Delta E}{k_B T}}\right)} \tag{5.6}$$

As a consequence, at around 4 K, $\Gamma_{up} < 1/(2T_{1,orbital})$ and hence, $1/T_2^* > \Gamma_{up}$. This strongly suggest that other dephasing mechanisms also contribute to the spin dephasing rate $1/T_2^*$ of this SiV^-. We can decompose the spin dephasing rate into the contribution Γ_{up} from single-phonon excitation to the upper orbital branch and the contribution γ from the remaining dephasing mechanisms:

$$1/T_2^* = \Gamma_{up} + \gamma \tag{5.7}$$

To extract the contribution of the remaining dephasing mechanisms, we thus need to determine Γ_{up}. However, in our experimental setup, due to the thermometer being

located below the sample mount, the sample temperature tends to be underestimated $T_{measured} < T$ as most of the heating comes from the microwave radiation on top of the sample. In Fig. 5.5, we plot as a solid grey curve the lower bound $\Gamma_{up,min}$ obtained by taking $T = T_{measured}$ in the Boltzmann factor and using the linear dependence of $1/T_{1,orbital}$ from Fig. 5.3. As expected, this curve lies below the experimental values of $1/T_2^*$. Adding a constant to $\Gamma_{up,min}$ allows us to compensate for this difference (dotted grey curve in Fig. 5.5), and we therefore extract an upper bound γ_{max} on the contribution from other dephasing sources with $1/\gamma_{max} \approx 300\,\text{ns}$. This characteristic time can be taken as a lower bound for T_2^* in the absence of single-phonon-mediated dephasing.

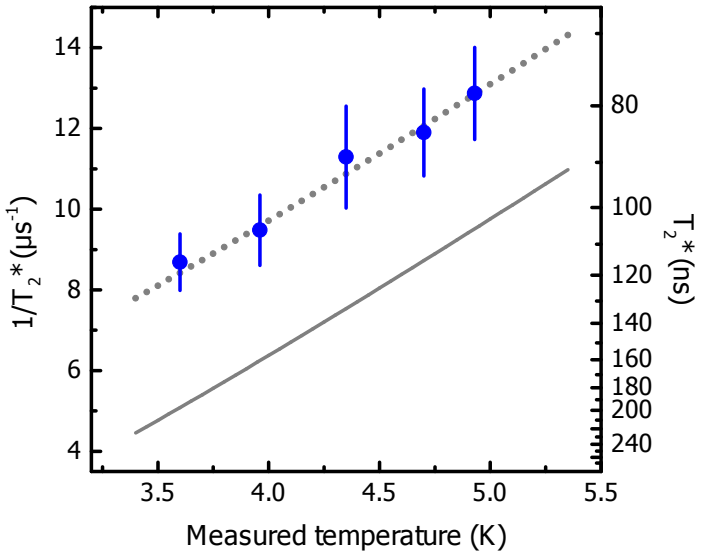

Figure 5.5 Comparison between the temperature dependence of the spin dephasing rate $1/T_2^*$ (blue dots) and that of the lower bound of the upward orbital transition rate $\Gamma_{up,min}$ (solid grey curve). The dotted grey curve corresponds to $\Gamma_{up,min} + 1/(300\,\text{ns})$.

Among the possible sources of this extra dephasing, the dominant one is likely to be the bath of ^{13}C nuclear spins and of nitrogen impurity electronic spins in the HPHT diamond sample. Such magnetic dephasing mechanisms can be minimised by using isotopically purified diamond for ^{13}C and purer diamond samples grown by chemical vapour deposition (CVD) for nitrogen impurities. Furthermore, techniques such as spin echo and dynamical decoupling can be used to eliminate the impact of its lower frequency components on the spin coherence, and are routinely implemented with NV^- centres [143, 184, 189, 190].

5.2.2 Spin population decay

We now investigate whether the spin decay time $T_{1,spin}$ is also affected by the thermally excited transitions between orbital branches. We thus measure the temperature dependence of the spin decay rate $1/(2T_{1,spin})$, as shown in Fig. 5.6. Its linear dependence with temperature indicates that it is also dominated by a single phonon process.

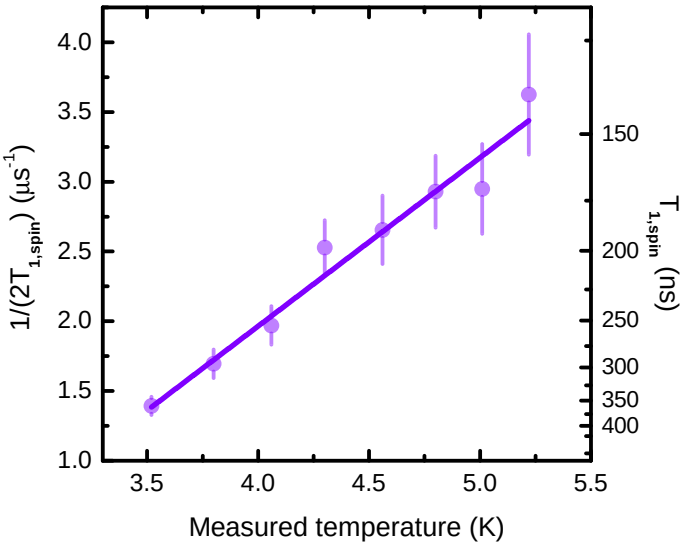

Figure 5.6 Temperature dependence of the spin decay time $T_{1,spin}$ (purple dots). Error bars correspond the the standard error from the fit of the exponential recovery (see Section 4.2). The solid purple curve is a linear fit with $1/(2T_{1,spin})\,(\mathrm{MHz}) = (1.2 \pm 0.1)(\mathrm{MHz\,K^{-1}}) * T\,(\mathrm{K}) - (2.9 \pm 0.4)\,(\mathrm{MHz})$.

The suggested dominant mechanism for spin decay relies on excitation to the upper orbital branch of the ground state followed by relaxation back to the lower orbital branch. One of those two transitions could happen between two states with different dominant spin orientations, thus leading to a spin flip in the lower branch of the ground state. To verify this possibility, we make use of the group theoretical modelling of the SiV^- from Section 4.1.3 to deduce the tomography of the ground state manifold at 0.2 T, as shown in Fig. 5.7 for the lower orbital branch and in Fig. 5.8 for the upper orbital branch. Each state is dominated by a given projection of the electron spin and of the nuclear spin, but also includes weaker components of the other

projections, especially for the electron spin. It is thus possible to have spin-preserving transitions between states of opposite dominant spin orientations, as will be developed in Section 5.3. This mechanism also explains why $T_{1,spin}$ can reach several milliseconds [171] when the magnetic field is aligned with the SiV symmetry axis which otherwise mixes the spin as defined by the spin-orbit interaction, as seen in Chapter 2 Section 2.5.

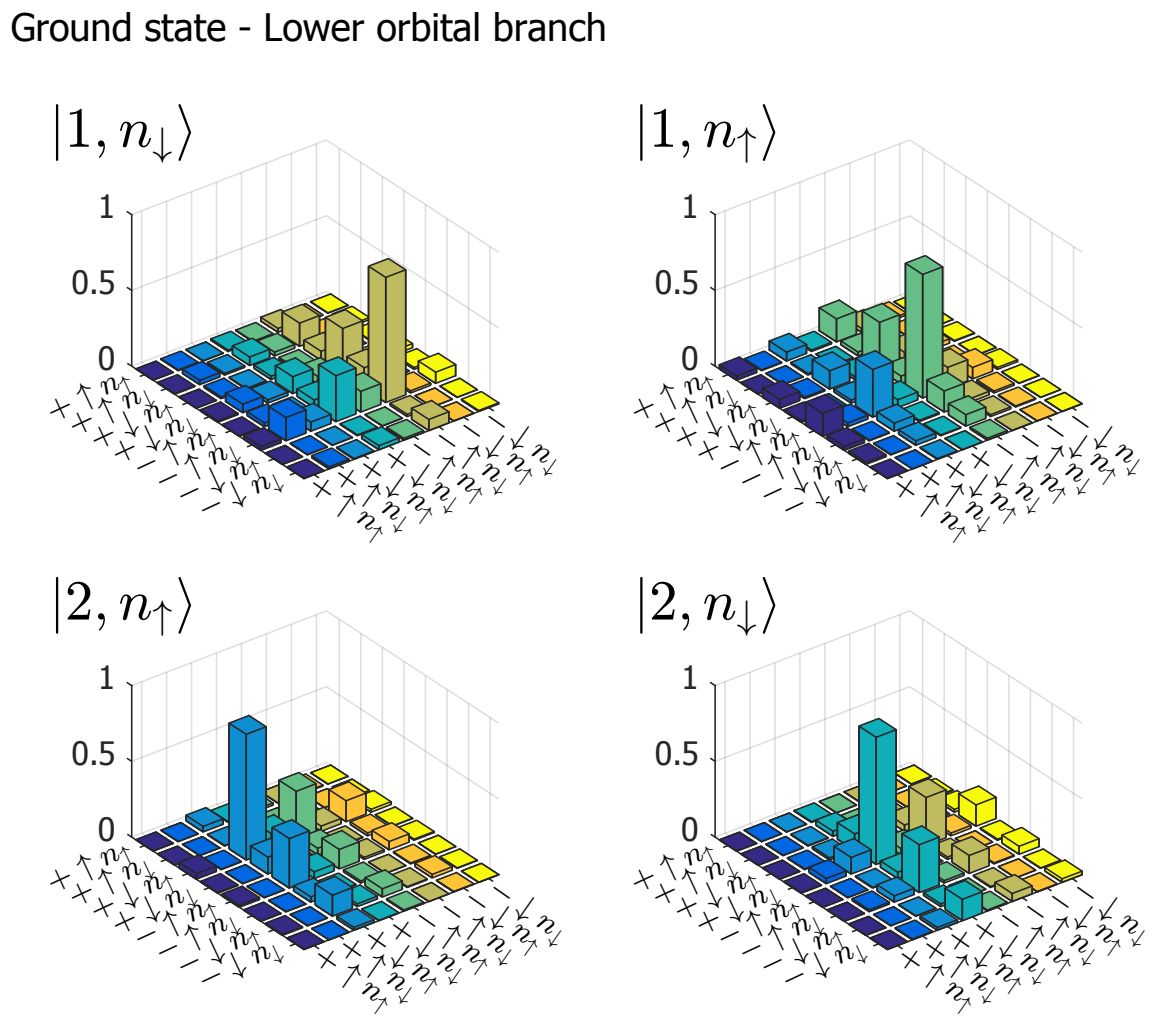

Figure 5.7 Simulated tomography of the SiV^- eigenstates in the lower branch of the ground state at 0.2 T and for an angle of 109.5° between magnetic field and SiV axis. The basis used is the eigenbasis of the spin-orbit coupling (see Section 2.4) expanded with the nuclear spin states $|n_\uparrow\rangle$ and $|n_\downarrow\rangle$. Each bar indicates the norm of the corresponding component in the density matrix of the state.

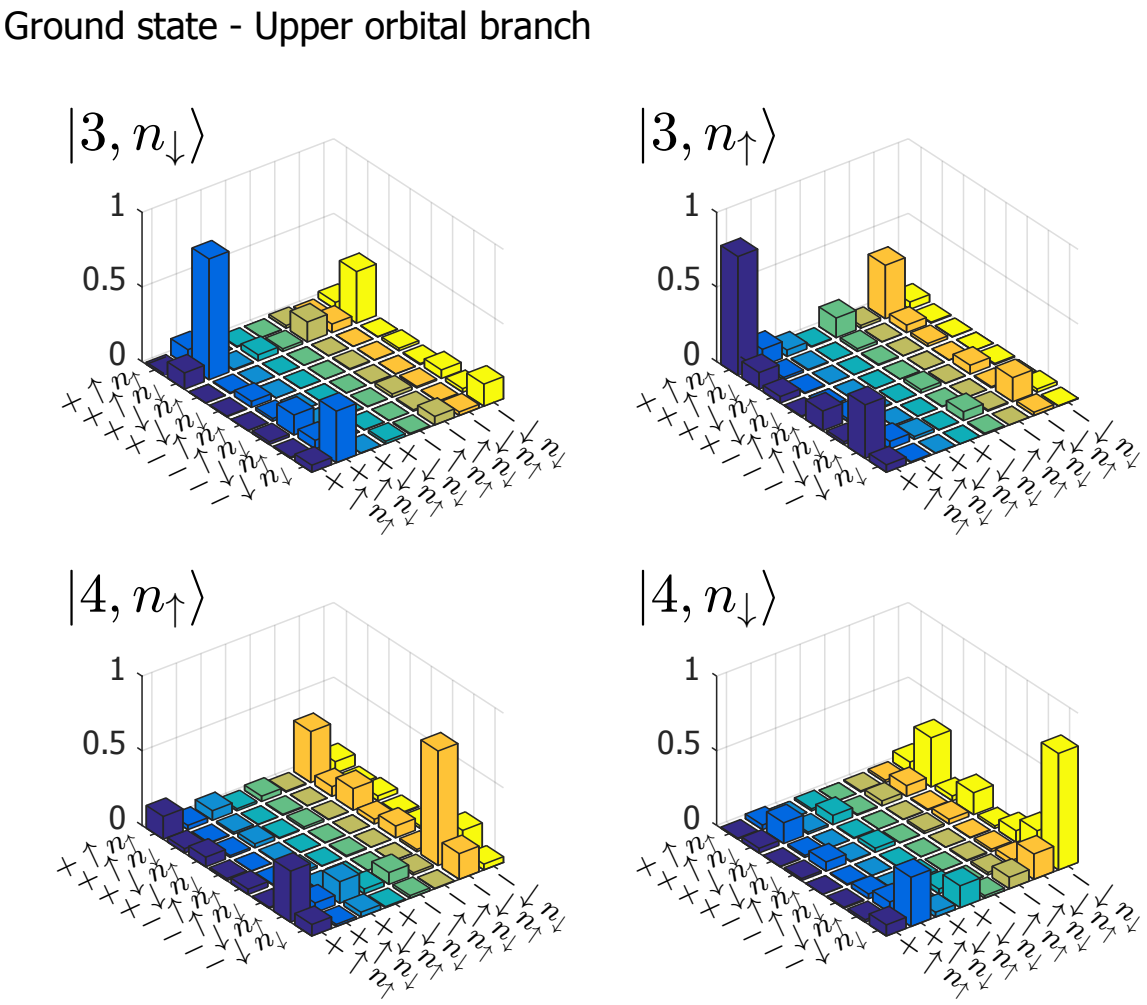

Figure 5.8 Simulated tomography of the SiV^- eigenstates in the upper branch of the ground state at 0.2 T and for an angle of 109.5° between magnetic field and SiV axis. The basis used is the eigenbasis of the spin-orbit coupling (see Section 2.4) expanded with the nuclear spin states $|n_\uparrow\rangle$ and $|n_\downarrow\rangle$. Each bar indicates the norm of the corresponding component in the density matrix of the state.

5.2.3 Discussion

Both dephasing and population decay of the SiV^- spin are limited by single-phonon transitions between the orbital branches of the ground state, as evidenced by their temperature dependence. Hence, an obvious way to improve the coherence times of the spin is to cool the SiV^- down. At 1 K, a temperature achievable by evaporative cooling of liquid helium, Γ_{up} is already decreased by more than an order of magnitude compared to its value at 3.6 K. Reaching the mK range using a dilution refrigerator will then virtually eliminate this source of decoherence. Another approach would consist in

decreasing the density of states of phonons at 50 GHz, the orbital transition frequency. This would most likely require nanostructures smaller than 120 nm, the half-wavelength of those phonons in diamond. This is not only challenging from a fabrication point of view but would also bring the SiV^- in close proximity with surfaces, which are notorious sources of spin decoherence for NV^- centres [191–193]. However, it should be noted that some of the surface-related decoherence arises from electric noise to which SiV^- is insensitive to first order due to its inversion symmetry [99, 136]. Finally, an alternative strategy relies on applying strain to the SiV^- which, as we are going to see in the following section, splits the orbital branches further apart, thus increasing the energy required for phonons to cause decoherence.

5.3 SiV^- centres in nanodiamonds: Influence of strain

The solid-state environment of the SiV^- can present inclusions and vacancies as well as structural defects such as grain boundaries, stacking fault and dislocations. Such defects, especially structural ones, are difficult to eliminate and are thus likely to be present in most crystals. The most notable consequence of structural defects is local distortions of the carbon lattice. This local alteration of the positions of atoms is likely to impact the electronic states of any SiV^- centre located nearby. It is thus important to investigate how SiV^- states are affected by strain and how the SiV^- optical and spin properties are altered. We here study single SiV^- centres in diamond nanocrystals, which exhibit significant strain from the growth process.

5.3.1 Experimental setup and samples

The experimental setup used for these experiments is the same as the one described in Section 3.2. The sample studied consists of nanodiamonds grown on an iridium substrate. Their fabrication process is described in Ref.[94]. They have a diameter of approximately 130 nm with 40 nm standard deviation. The substrate is composed of a 150 nm-thick iridium layer deposited on a 40 nm buffer layer of yttria-stabilised zirconia, itself on a silicon substrate. The growth process consists in seeding nanodiamonds (Microdiamant Liquid Diamond MSY) with sizes up to 30 nm on the iridium surface. Then, a microwave plasma assisted CVD process is used to grow the nanodiamonds on the seeds. Silicon is incorporated during the growth by etching of the cut areas of the

silicon substrate [94]. The iridium layer reduces the amount of silicon incorporated from the substrate and permits a limited lattice mismatch with the diamond nanocrystals [94]. For this sample, no preferential orientation of the nanodiamonds has been imposed, which results in a variety of possible orientations of SiV centres with regards to the applied magnetic field. An average density of one bright SiV^- centre per $50 \times 50\,\mu m^2$ has been observed. The strain in nanodiamonds likely originates from lattice mismatch between nanodiamond and substrate, a difference of thermal expansion coefficients and growth stress when slightly differently oriented crystallites merge into a single nanocrystal [123, 144]. The use of nanodiamonds also presents major advantages. In fact, it has been shown that the excitation efficiency of single SiV^- centres can be enhanced in nanodiamonds, possibly due to an increase of the absorption coefficient linked to a change in the vibronic states of the centre, or to the possibility of development of resonant modes (Mie resonances) of the light in nanodiamonds smaller than the excitation wavelength [115, 123]. Furthermore, the sub-wavelength size of nanodiamonds eliminates total internal reflections present in bulk, and therefore enhances the luminescence extraction [115, 123].

5.3.2 Shift of energy levels

We start by measuring the non-resonant spectra of strained SiV^- centres in nanodiamonds as well as the magnetic field dependence of the optical transitions. Figure 5.9 shows the Zeeman spectra of three SiV^- centres. At zero magnetic field, the splittings between optical transitions differ from unstrained centres and vary from centre to centre. Tracing the transitions back to the energy levels, these spectra indicate that strain induces larger splittings between the orbital branches in the ground and excited states. The general pattern of the magnetic field dependence of transitions is the same, with each transition splitting into four and the presence of avoided crossings. However, the magnitude of the splittings with magnetic field varies between the centres. This is owing to the absence of a preferential growth orientation; nanodiamonds and hence SiV centres have a random orientation with respect to the applied magnetic field.

We investigate this behaviour further by using the group theoretical approach presented in Section 2.4. Assuming uniaxial stress, a group theoretical analysis performed in Refs. [149, 194] leads to the following Hamiltonian for strain, when

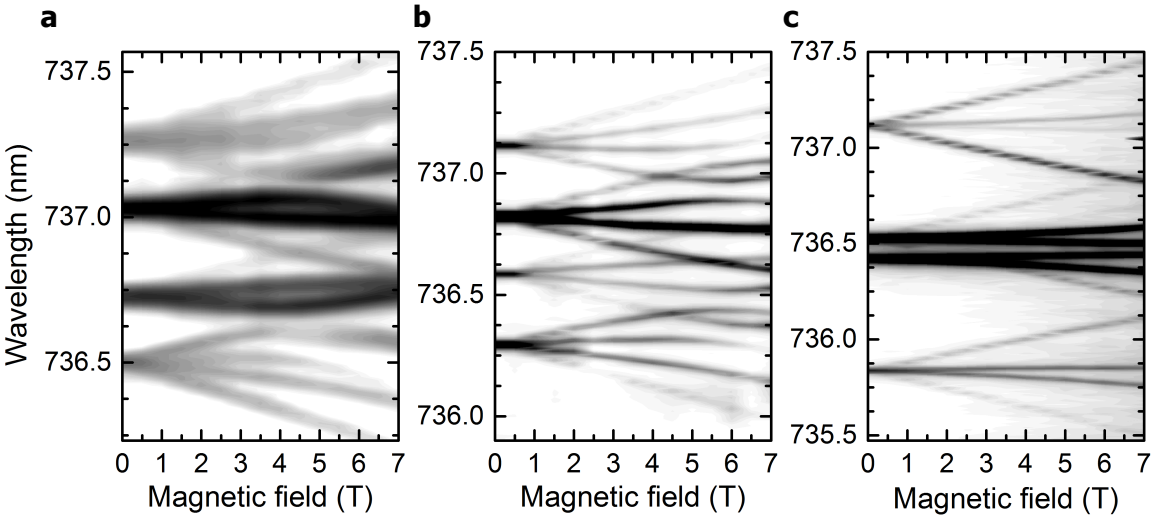

Figure 5.9 Magnetic field dependence of the fluorescence spectra for single SiV^- centres in nanodiamonds, referred to as SiV A in (a), SiV B in (b) and SiV C in (c). The intensity scale is logarithmic for (a) and (c), linear for (b). Due to the growth conditions, the relative orientations of the SiV centres with respect to the external magnetic field are unknown.

expressed in the basis $\{|e_x\uparrow\rangle, |e_x\downarrow\rangle, |e_y\uparrow\rangle, |e_y\downarrow\rangle\}$:

$$\mathcal{H}_{strain} = \begin{pmatrix} \alpha-\delta & 0 & \beta & 0 \\ 0 & \alpha-\delta & 0 & \beta \\ \beta & 0 & -\alpha-\delta & 0 \\ 0 & \beta & 0 & -\alpha-\delta \end{pmatrix} \tag{5.8}$$

where α, β and δ are scaling factors which describe the response of the SiV^- centre to a strain contribution of symmetry E_{gx}, E_{gy} and A_{1g}, respectively. These factors can be different between ground and excited states. As the model focuses on splittings among the levels of the ground state and of the excited state, the parameter δ, which acts similarly on all the levels, is ignored and taken equal to zero. This Hamiltonian is added to the group theoretical model to simulate the experimental fluorescence spectra. An example of such a simulation is given in Fig.5.10 for SiV B presented in Fig. 5.9b.

Despite the strong assumption of the stress being uniaxial, we can see that the model captures the influence of strain on the SiV^- fluorescence. It also allows us to determine an angle of $70 \pm 5°$ between SiV axis and magnetic field from the splitting of the transitions. We can see from the simulated energy levels displayed in Fig. 5.11 that the orbital splitting is indeed larger than for unstrained centres with a value of

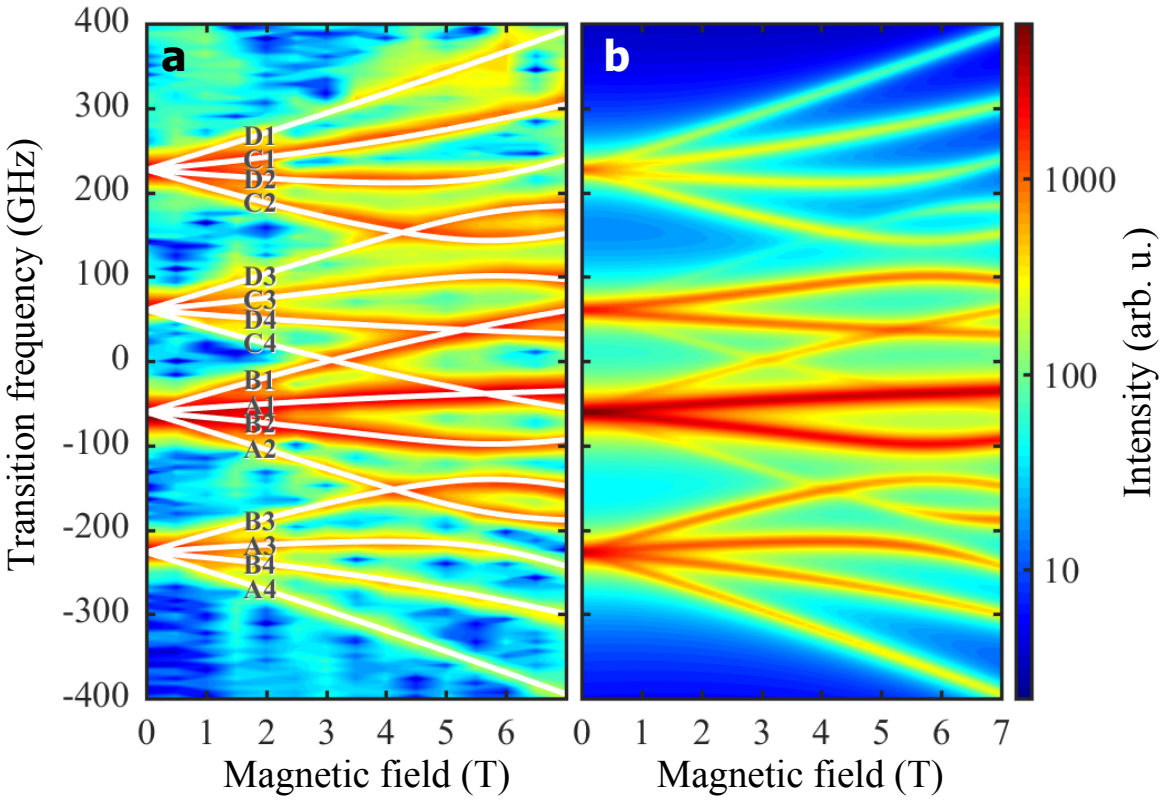

Figure 5.10 Simulation of the Zeeman splitting for the emitter presented in Fig. 5.9b. (a) Experimental spectra as a function of magnetic field superimposed with the simulated optical transitions as white curves. Transition labels correspond to the energy levels displayed in Fig. 5.11. (b) Fully simulated optical spectra. The fit between the magnetic field splitting for the experimental spectra and the simulated transitions allows us to determine that the SiV axis makes an angle of $70 \pm 5°$ to the applied magnetic field. The strain parameters used are $\alpha_g = 13 \pm 1\,\text{GHz}$ and $\beta_g = 76 \pm 3\,\text{GHz}$ for the ground state, and $\alpha_e = 10 \pm 1\,\text{GHz}$ and $\beta_e = 57 \pm 3\,\text{GHz}$ for the excited state.

more than 100 GHz compared to the usual 50 GHz. This results in the avoided crossing between states $|2\rangle$ and $|3\rangle$ occurring at a larger magnetic field. This link between strain and larger orbital splitting can be seen in the strain matrix acting on the same elements as the spin-orbit Hamiltonian (see Eq. 2.1), which is mainly responsible for the orbital splitting. We also notice that strain does not couple the different spin states and only alters the orbital part of the wavefunctions. However, due to the strong interplay between orbitals and spin in the physics of the SiV$^-$, we can expect that strain does have an impact on the spin properties.

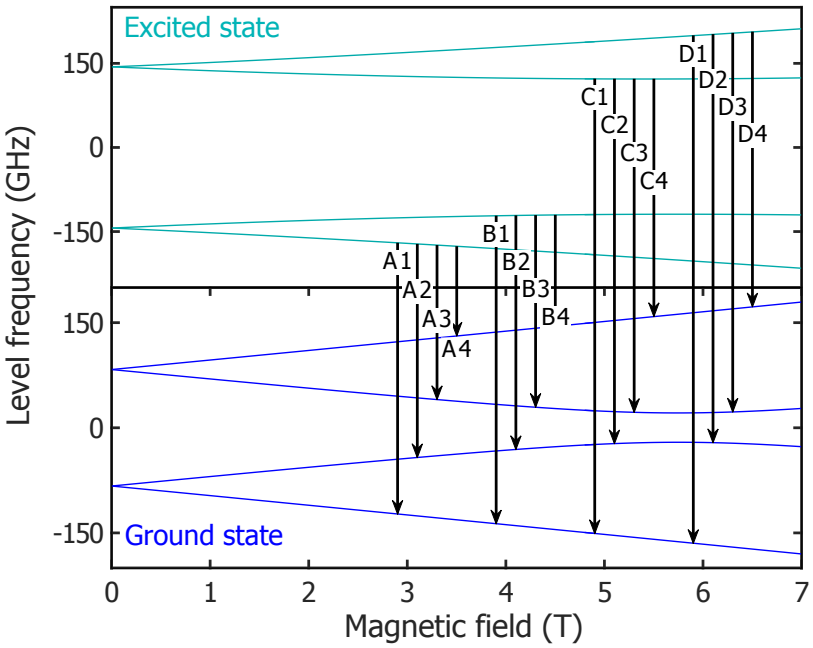

Figure 5.11 Simulated energy levels deduced from Fig. 5.10.

5.3.3 Optical selection rules

To evaluate the influence of strain on spin properties, we perform resonant excitation of SiV B under magnetic field. As in Chapter 2 Section 2.3.1, we selectively populate an excited state with a given spin orientation and measure the resulting optical spectrum. Figure 5.12a displays the fluorescence spectra obtained when populating levels D and C, the two levels of opposite spin orientations in the excited state upper orbital branch.

The two resonant spectra display a certain selectivity in the fluorescing optical transitions. However, they are not completely complementary and several transitions show clear fluorescence in both spectra. We trace back those transitions to the energy levels, as illustrated in 5.12b. In the excited state upper branch, transitions are seen to occur from the addressed level only, but in the lower branch, fluorescence is observed from both levels even though some degree of selectivity remains, with the level of same spin orientation as the addressed one generating more fluorescence than the level of opposite spin orientation. We repeat the experiment, addressing levels A and B of the lower branch of the excited state, as shown in Fig. 5.13a. The obtained spectra are completely complementary and transitions only occur from the addressed level, as illustrated in Fig. 5.13b. This shows that, while spin selectivity is preserved within each excited state orbital branch, thermalisation does not preserve this selectivity. Strain thus seems to have an impact on the spin part of the SiV^- states.

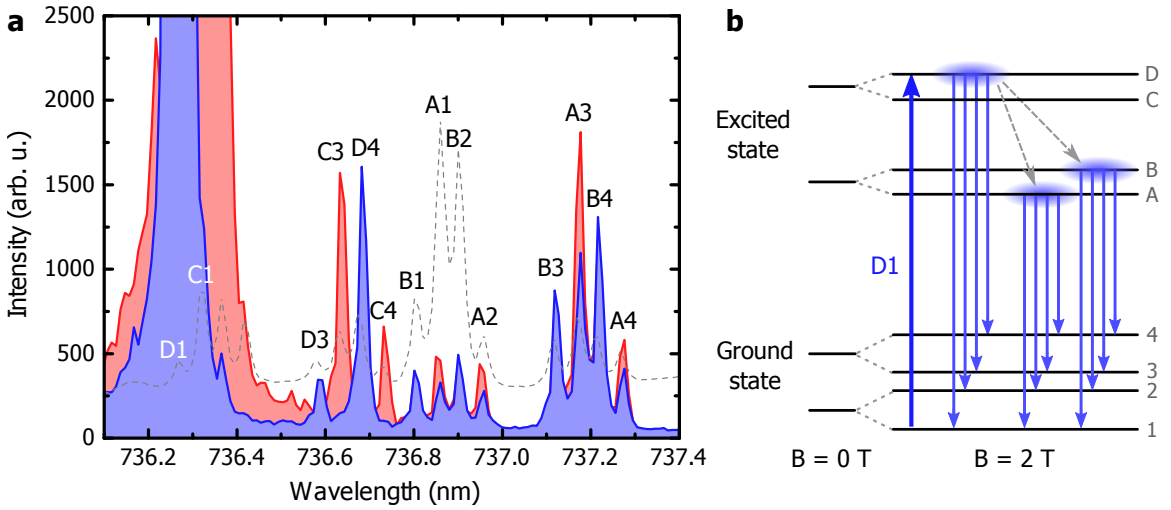

Figure 5.12 Resonant excitation of SiV B under a magnetic field of 2 T. (a) Fluorescence spectra obtained when resonantly exciting transition D1 (blue shaded curve) and C1 (red shaded curve). Each transition is labelled according to Figs. (b) and 5.10. The non-resonant spectrum at 2 T is displayed as a dashed grey curve. (b) Representation of the energy levels of the SiV$^-$ with resonant excitation of transition D1 displayed as a dark blue arrow. Experimentally measured optical transitions occur from excited state levels D, B and A to the four ground state levels, as represented by light blue arrows. Grey dashed arrows indicate the observed thermalisation among the excited state levels.

To verify this, we compare the simulated tomographies of the states of the strained SiV B, as shown in Fig. 5.14, with that of states simulated using the same parameters except the strain ones which are set to zero, as seen in Fig. 5.15. We can see that while in both cases, states contain some components of both spin orientations, with one dominating the other, the states in the strained case contain larger components of the minority spin orientation.

In order to gain further understanding of the interplay between strain and spin-orbit coupling, we express both Hamiltonians in the eigenbasis of the spin-orbit coupling $\{|e_+\uparrow\rangle, |e_+\downarrow\rangle, |e_-\uparrow\rangle, |e_-\downarrow\rangle\}$ (see Section 2.4):

$$\mathcal{H}_{SO}^{\pm} = \begin{pmatrix} \lambda/2 & 0 & 0 & 0 \\ 0 & -\lambda/2 & 0 & 0 \\ 0 & 0 & -\lambda/2 & 0 \\ 0 & 0 & 0 & \lambda/2 \end{pmatrix} \tag{5.9}$$

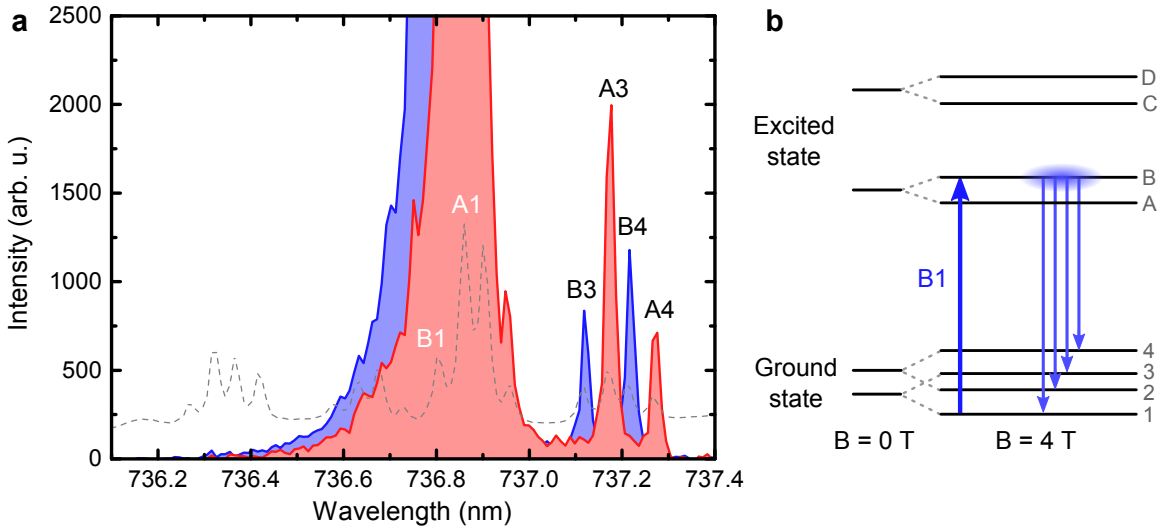

Figure 5.13 Resonant excitation of SiV B under a magnetic field of 2 T. (a) Fluorescence spectra obtained when resonantly exciting transition B1 (blue shaded curve) and A1 (red shaded curve). Each transition is labelled according to Figs. (b) and 5.10. The non-resonant spectrum at 2 T is displayed as a dashed grey curve. (b) Representation of the energy levels of the SiV^- with resonant excitation of transition B1 displayed as a dark blue arrow. Experimentally measured optical transitions occur from excited state level B to the four ground state levels, as represented by light blue arrows.

$$\mathcal{H}^{\pm}_{strain} = \begin{pmatrix} 0 & 0 & -(\alpha - i\beta) & 0 \\ 0 & 0 & 0 & -(\alpha - i\beta) \\ -(\alpha + i\beta) & 0 & 0 & 0 \\ 0 & -(\alpha + i\beta) & 0 & 0 \end{pmatrix} \tag{5.10}$$

While the strain Hamiltonian does not couple states with different spins, it is not diagonal in the spin-orbit basis and thus couples the orbital states dictated by the spin-orbit coupling. Consequently, strain and spin-orbit coupling compete to determine the orbital part of the states. As the spin-orbit coupling fixes the spin orientation to its orbital eigenstates, we can thus consider that strain indirectly weakens the spin quantisation axis determined by the spin-orbit coupling, resulting in a larger mixing of spin orientations in the presence of an external magnetic field. As transitions between orbital branches are mediated by single phonons [130], the corresponding operator $\mathcal{T}$ couples the same states as strain and the Jahn-Teller effect and thus changes the orbital from e_+ to e_- and inversely. To first order, Fermi's golden rule gives that the transition probability is proportional to $|\langle f|\mathcal{T}|i\rangle|^2$ where $|i\rangle$ and $|f\rangle$ are the initial and final states respectively. The diagonal of the state tomographies in Fig.5.15 represents

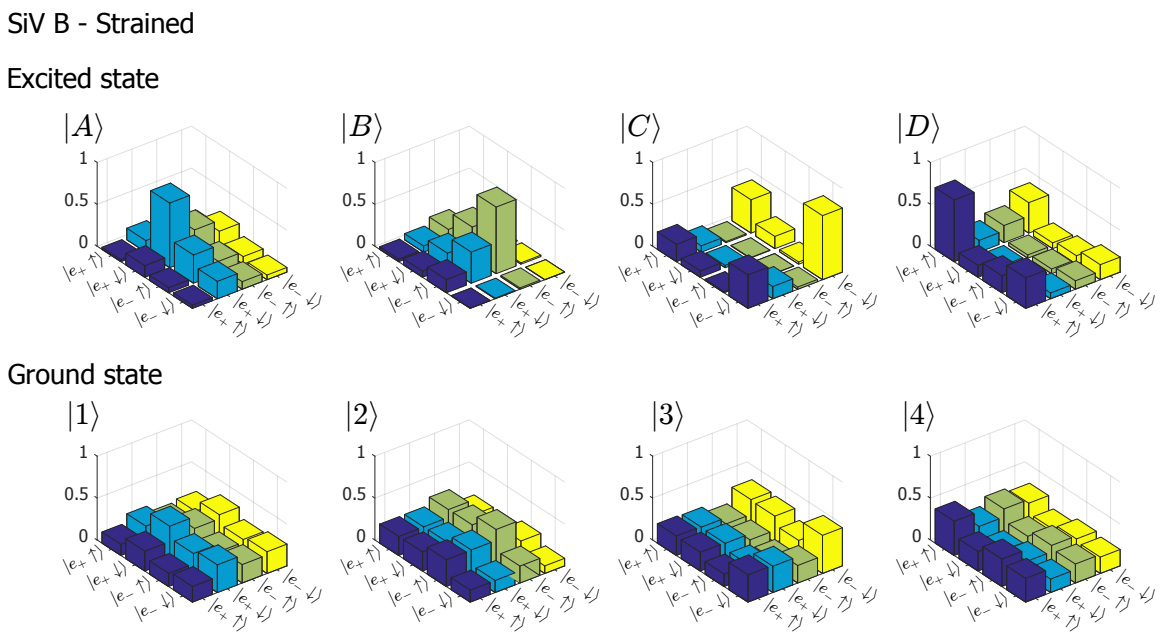

Figure 5.14 Tomography of the states of the strained SiV B at 2 T and for an angle of 70° between SiV axis and magnetic field. (The basis used is the eigenbasis of the spin-orbit coupling (see Section 2.4). Each bar indicates the norm of the corresponding component in the density matrix of the state.)

the diagonal of the density matrices of the states, which corresponds to the populations along the different basis states. We can see that state $|D\rangle$ has mainly components along the basis states $|e_+\uparrow\rangle$ and $|e_-\downarrow\rangle$. These will thus be transferred to $|e_-\uparrow\rangle$ and $|e_+\downarrow\rangle$ respectively. The components of $|A\rangle$ and $|B\rangle$ are mainly along $|e_-\uparrow\rangle$ and $|e_+\downarrow\rangle$, while those of $|C\rangle$ are along $|e_+\uparrow\rangle$ and $|e_-\downarrow\rangle$. As a consequence, $|D\rangle$ can relax to $|A\rangle$ and $|B\rangle$, but not to $|C\rangle$. The same analysis can be done for relaxation from state $|C\rangle$. We have thus shown that strain, through its alteration of orbitals and with its interplay with the spin-orbit coupling, has an impact on the spin properties of the SiV$^-$. This influence leads to a modification of transition selection rules, highlighting the importance of both the orbital and spin components of the SiV$^-$ eigenstates.

5.3.4 Coherent population trapping

With evidence of strain impacting upon the transitions between orbital branches, where such transitions are a major source of decoherence, we investigate the link between strain and coherence. We use coherent population trapping to probe the spin dephasing of an SiV$^-$ in a nanodiamond, with strain causing a ground state splitting

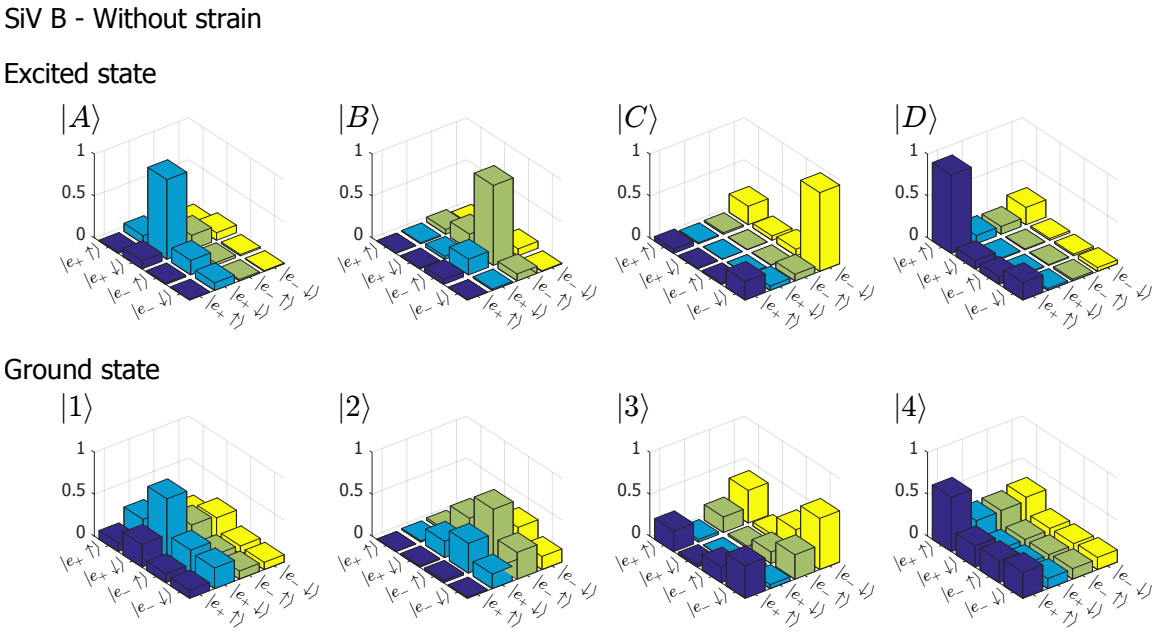

Figure 5.15 Tomography of the states simulated using the same parameters as in Fig. 5.14, with the exception of all strain parameters set to zero. (The basis used is the eigenbasis of the spin-orbit coupling (see Section 2.4). Each bar indicates the norm of the corresponding component in the density matrix of the state.)

of 360 ± 5 GHz. The setup is similar to that described in Chapter 3 Section 3.2, and the transitions addressed are transitions D1 and D2, as in Fig. 3.8. We managed to achieve CPT, as shown in Fig. 5.16. We can see that the driven transitions display some spectral wandering, which is caused by the relative fluctuation of the excited state level with respect to both ground state levels. The latter two do not appear to fluctuate significantly with respect to each other as the two-photon resonance leading to CPT occurs for the same values of detunings for both transitions.

By decreasing the power of both lasers, we can reach a CPT dip of 12 ± 1 MHz with laser powers close to saturation, as seen in Fig. 5.17a. This value is very similar to that obtained for the SiV^- with about 6 times less strain in bulk diamond under similar excitation conditions (see Section 3.3). Furthermore, by repeating CPT scans in time, as diplayed in Fig. 5.17b, we can see that the two-photon resonance condition fluctuates, sign that the two ground state levels exhibit frequency fluctuations with respect to each other. Fluctuations faster than the experimental acquisition time of about 15 s over the CPT dip widen this dip. As a consequence, we can assume that the CPT dip value measured is only an upper bound. It thus appears that a spin coherence

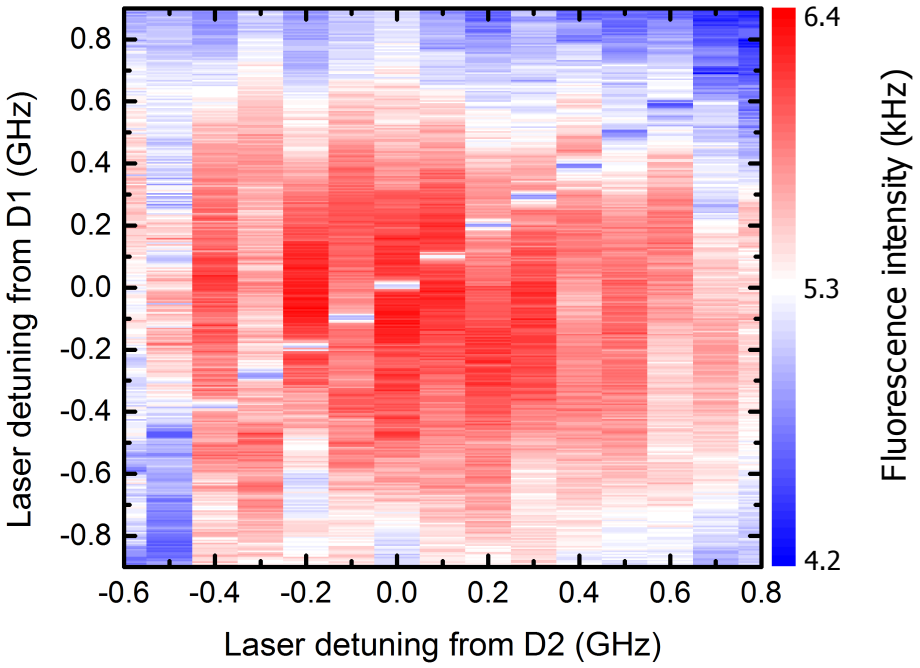

Figure 5.16 Coherent population trapping on a strained SiV$^-$ centre in a nanodiamond. The fluorescence from the SiV$^-$ is plotted (colour scale) as a function of the detunings of each laser addressing transitions D1 and D2. A magnetic field of 9 T is applied to allow selective addressing of the two driven transitions.

comparable to that obtained for low strain SiV$^-$ centres in bulk can be obtained with strongly strained centres in nanodiamonds.

The origin of the spectral wandering and ground state splitting fluctuations is unclear. It has been reported that other colour centres in diamond, such as chromium centres and NV$^-$ centres, experience worse emission properties in nanodiamonds than in bulk, including shorter lifetimes by more than one order of magnitude [184, 195, 196]. This is generally attributed to the proximity of the surface where diverse impurities and charge traps influence the dynamics and coherence of the centre [184, 147]. Surface treatments have been shown to affect the emission quality of colour centres in diamond with a view to improving it [147, 197].

5.3.5 Discussion: Using strain to improve the spin coherence time

We have seen in Section 5.2 that spin decoherence is dominated at 4 K by phonons resonant with the splitting between the two orbital branches of the ground state.

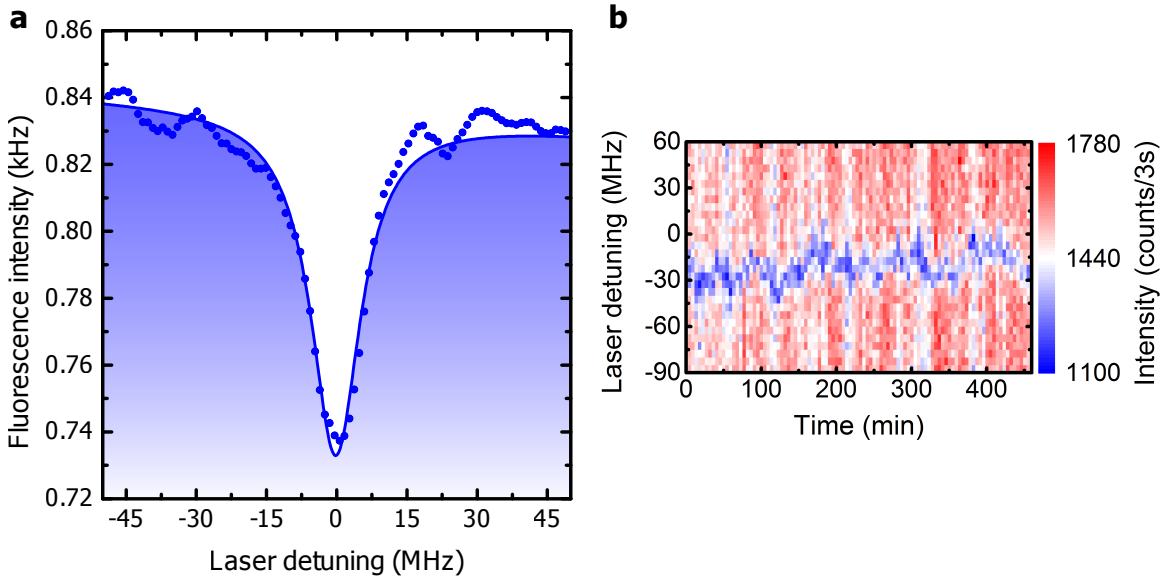

Figure 5.17 Coherent population trapping on a strained SiV^- at low laser powers (90 nW corresponding to half saturation power for transition D2 and 180 nW corresponding approximately to saturation power for transition D1). (a) CPT scan. (b) CPT scans measured as a function of time. Fluorescence intensity is colour-coded.

This decoherence is thus directly proportional to the phonon population, which is of the form $\omega^3 n(\omega,T)$, where ω is the frequency of the phonons. This is obtained by considering a linear SiV-phonon coupling in ω, a phonon density of states varying as ω^2 in bulk and their population following Bose-Einstein statistics $n(\omega,T)$ [130]. While at 4 K the population of phonons at 50 GHz is still significant, increasing the orbital splitting by applying strain would lead to first an increase in phonon population, followed by a decrease for splittings beyond approximately 230 GHz. At this energy, the decrease due to the Bose-Einstein statistics starts to dominate over the increase of density of states and we reach a net decrease of phonon population for splittings beyond 600 GHz. The fact that strain allows transitions to occur between more levels, as seen in Subsection 5.3.3 would be overcome by the depletion of the phonons mediating those transitions. Furthermore, nanodiamonds or diamond nanostructures with dimensions smaller than the phonon half-wavelength ($\approx$ 120 nm) would also deplete the density of states of phonons responsible for spin decoherence. If the observed frequency fluctuations can be overcome through surface treatments, strained diamond nanostructures would thus be an ideal platform to eliminate the dominant source of decoherence of the SiV^- spin.

5.4 Conclusion

In this chapter, we have investigated the interaction of the SiV^- centre with certain elements of its environment. We have determined, through ODMR, a value of the hyperfine constant $A_{\parallel} = 70 \pm 2\,\mathrm{MHz}$ between the SiV^- electronic spin and the nuclear spin of the ^{29}Si atom. Through the temperature dependence of the spin dephasing time and the spin decay time, we have shown that both are dominated by single phonon-mediated transitions between ground state orbital branches. And finally, we have shown with SiV^- centres in nanodiamonds that strain increases the orbital splitting and indirectly affects the spin composition of the SiV^- states, thus relaxing the selectivity of phonon-mediated transitions. While it is clear that some interactions, such as phonons, have a detrimental effect on the spin coherence properties, others, such as nuclear spins and strain, can be used as resources. We have mentioned how strain can advantageously eliminate phonon-induced spin decoherence. A natural extension of this work would be to deterministically apply strain to an SiV^- and measure the corresponding evolution of the spin coherence properties until no improvement can be measured and other decoherence mechanisms become dominant. Furthermore, the controlled application of strain can be used to tune the emission wavelength to interface emitters for quantum communication applications. Another axis of development will be to gain control over the ^{29}Si nuclear spin, starting with initialisation and readout using the SiV^- spin, and followed by its coherent control with a radiofrequency, with a view to performing quantum gates between the two spins [67, 69–72].

Conclusion and outlook

In this thesis, we have investigated the spin properties of the SiV^- centre with the perspective of integrating it into a quantum network as a spin-photon interface. The desirable optical qualities of this colour centre already make it an advantageous source of indistinguishable photons for applications in quantum optics and quantum communications [136, 128].

In this work, we have shown, through the analysis of the fluorescence emitted under resonant excitation and in the presence of an external magnetic field, that the SiV^- offers a spin degree of freedom $S = 1/2$, which can be operated as a well-defined quantum bit for quantum computing. This also implies that the emitted photons, through their frequency, are correlated with the electronic spin state. We have then showed, through the realisation of coherent population trapping, that this electronic spin can be controlled with light, and thus, that the spin state can be correlated with incoming photons. We have hence evidenced the potential for two-way spin-photon interfacing using the SiV^- centre.

While the control over the photon side of this interface is fairly trivial, the spin side also needs to be controlled independently. We have addressed this point and demonstrated coherent control of the spin state of a single SiV^- using microwave pulses. Such a control is at the basis of quantum information processing algorithms [1, 2, 198] and constitutes a stepping stone for the implementation of quantum gates using the spin of the SiV^-.

As coherent control allows to encode quantum information into the spin degree of freedom, the ensuing interrogation concerns the time during which such information can be reliably processed and stored by this spin. Using coherent population trapping, we have extracted a first estimation of the spin dephasing time, and coherent control has allowed us, through Ramsey interferometry, to get a more direct measurement leading to a value of 115 ± 9 ns at 3.6 K. Considering that such a coherence time appears modest compared to other solid-state systems [40, 180, 181], we have investigated what

its primary limitation is and have determined that single-phonon-mediated transitions between ground state orbital branches is the dominant source of spin dephasing.

We have then examined the impact of crystalline strain on the SiV^- eigenstates and suggested how it can be taken advantage of to circumvent this limitation. Strain increases the splitting of the orbital branches and can in this way allow us to reach energies at which phonon population is negligible at 4 K. We have also briefly investigated another resource to have access to longer coherence times: the nuclear spin of ^{29}Si, for which we have measured, through optically detected magnetic resonance, a hyperfine constant of 70 ± 2 MHz.

In summary, we have shown through our study of the spin of the SiV^- that this colour centre is a promising system to be used as a spin-photon interface.

A complementary extension of this work will consist in achieving all-optical control of the spin state. Indeed, while microwave control offers the opportunity to work in a magnetic field configuration enabling single-shot readout of the spin state [176, 177] through cycling transitions, all-optical control will allow us to reach ultrafast control using ps pulses [36, 37, 199, 200], hence compensating for the short spin dephasing time.

Further developments on the path towards quantum computing closely follow the direction set by the NV^- centre, with first the demonstration of spin-photon entanglement [64], followed by photon-mediated spin-spin entanglement [65, 66]. One of the main difficulties in these experiments is the low intensity of the zero-phonon line of the NV^- centre, which considerably limits the rate of entangling events. These protocols will thus greatly benefit from the intense zero-phonon line of the SiV^-.

Similarly to the NV^- centre, the nuclear spin can be used as an asset for its long coherence due to weak coupling to its environment [73]. The milestones would include its coherent control through the electronic spin [69–71, 67, 72], demonstration of its entanglement with the electronic spin [67] or other nuclear spins [68], its use as an ancilla qubit for computation protocols [74], and its single-shot readout [201, 202].

However, for such experiments and to match the spin properties of the NV^- centre, much progress is needed to improve the electronic spin coherence time. To address this issue, operating at lower temperatures appears straightforward, but requires to be able to pump on liquid helium to reach 1 K or even to operate in a dilution refrigerator with optical access. An alternative approach consists in taking advantage of the sensitivity of SiV^- to strain to reach orbital splittings at which phonon population is negligible at 4 K. In order to apply large amounts of static strain in a controllable and scalable

way, a very promising approach is to use SiV^- centres implanted into a diamond cantilever [203, 204]. Such a device induces strain on the colour centre by applying a voltage between the cantilever and the surface underneath, causing the cantilever to bend towards the surface. Several of such devices would furthermore allow us to apply different amounts of strain to different centres and thus tune them in and out of resonance at will. Operated with an alternating voltage, this also opens the way to optomechanical experiments where spin and photons interact with mechanical modes [204–209]. The large strain susceptibility of SiV^-, which is 3-4 orders of magnitude larger than that of the NV^- centre ground state [135, 204], and the use of diamond optomechanical cavities [139] will help to reach the strong coupling regime with a view to implementing phonon-mediated quantum-information processing and quantum metrology [210]. Compared to photons, phonons have the advantage of needing a propagation medium, which can thus restrict interactions to the desired qubits and limit the risk of leakage to other qubits.

Finally, the SiV^- centre's strong zero-phonon line, its low inhomogeneous broadening and suitability as source of indistinguishable photons [136, 137], and the capacity to implant it with nanometric precision [138] make it a good candidate as a single-photon emitter in photonic structures [128, 211–214]. Those optical properties would in particular be of interest in photonic cavities to work towards strong coupling between SiV^- and photons. Reaching this regime would allow us to achieve photon blockade [215–217], where strong coupling with a single SiV^- only allows one photon to enter the cavity at a time depending on the state of the SiV^-. This would be crucial towards the implementation of quantum many-body simulations [218, 219] using a lattice of cavities, each containing a strongly coupled SiV^- [220–222]. Such an architecture would allow us to mimic solid-state phenomena exhibitted by electrons in the lattice of atoms. The strength of this approach would rely on having the capacity to taylor the cavity lattice at the single "atom" level through the individual control over the SiV^- state in each cavity. Another potential candidate for such experiments is the germanium-vacancy centre in diamond [103, 104]. This centre is thought to exhibit a high quantum efficiency based on the observation of non-linearities at the single-photon level for a single centre in a diamond photonic waveguide [223].

Bibliography

[1] M. A. Nielsen and I. L. Chuang, *Quantum Computation and Quantum Information*. Cambridge University Press, 2000.

[2] P. Shor, "Algorithms for quantum computation: discrete logarithms and factoring," in *Proceedings 35th Annual Symposium on Foundations of Computer Science*, pp. 124–134, IEEE Comput. Soc. Press, 1994.

[3] L. M. K. Vandersypen, M. Steffen, G. Breyta, C. S. Yannoni, M. H. Sherwood, and I. L. Chuang, "Experimental realization of Shor's quantum factoring algorithm using nuclear magnetic resonance," *Nature*, vol. 414, no. 6866, pp. 883–887, 2001.

[4] E. Knill, R. Laflamme, and G. J. Milburn, "A scheme for efficient quantum computation with linear optics," *Nature*, vol. 409, pp. 46–52, jan 2001.

[5] J. L. O'Brien, G. J. Pryde, A. G. White, T. C. Ralph, and D. Branning, "Demonstration of an all-optical quantum controlled-NOT gate," *Nature*, vol. 426, pp. 264–267, nov 2003.

[6] P. Kok, W. J. Munro, K. Nemoto, T. C. Ralph, J. P. Dowling, and G. J. Milburn, "Linear optical quantum computing with photonic qubits," *Reviews of Modern Physics*, vol. 79, pp. 135–174, jan 2007.

[7] J. C. F. Matthews, A. Politi, A. Stefanov, and J. L. O'Brien, "Manipulation of multiphoton entanglement in waveguide quantum circuits," *Nature Photonics*, vol. 3, pp. 346–350, jun 2009.

[8] R. Okamoto, J. L. O'Brien, H. F. Hofmann, and S. Takeuchi, "Realization of a Knill-Laflamme-Milburn controlled-NOT photonic quantum circuit combining effective optical nonlinearities.," *Proceedings of the National Academy of Sciences of the United States of America*, vol. 108, pp. 10067–71, jun 2011.

[9] Y. Li, P. C. Humphreys, G. J. Mendoza, and S. C. Benjamin, "Resource Costs for Fault-Tolerant Linear Optical Quantum Computing," *Physical Review X*, vol. 5, p. 041007, oct 2015.

[10] T. D. Ladd, F. Jelezko, R. Laflamme, Y. Nakamura, C. Monroe, and J. L. O'Brien, "Quantum computers," *Nature*, vol. 464, pp. 45–53, mar 2010.

[11] D. P. DiVincenzo, "The physical implementation of quantum computation," *Fortschritte Der Physik-progress of Physics*, vol. 48, no. 9-11, pp. 771–783, 2000.

[12] D. Leibfried, B. DeMarco, V. Meyer, D. Lucas, M. Barrett, J. Britton, W. M. Itano, B. Jelenković, C. Langer, T. Rosenband, and D. J. Wineland, "Experimental demonstration of a robust, high-fidelity geometric two ion-qubit phase gate," *Nature*, vol. 422, pp. 412–415, mar 2003.

[13] S. Gulde, M. Riebe, G. P. T. Lancaster, C. Becher, J. Eschner, H. Häffner, F. Schmidt-Kaler, I. L. Chuang, and R. Blatt, "Implementation of the Deutschâ€"Jozsa algorithm on an ion-trap quantum computer," *Nature*, vol. 421, pp. 48–50, jan 2003.

[14] M. Riebe, H. Häffner, C. F. Roos, W. Hänsel, J. Benhelm, G. P. T. Lancaster, T. W. Körber, C. Becher, F. Schmidt-Kaler, D. F. V. James, and R. Blatt, "Deterministic quantum teleportation with atoms," *Nature*, vol. 429, pp. 734–737, jun 2004.

[15] M. D. Barrett, J. Chiaverini, T. Schaetz, J. Britton, W. M. Itano, J. D. Jost, E. Knill, C. Langer, D. Leibfried, R. Ozeri, and D. J. Wineland, "Deterministic quantum teleportation of atomic qubits," *Nature*, vol. 429, pp. 737–739, jun 2004.

[16] D. Hanneke, J. P. Home, J. D. Jost, J. M. Amini, D. Leibfried, and D. J. Wineland, "Realization of a programmable two-qubit quantum processor," *Nature Physics*, vol. 6, pp. 13–16, jan 2010.

[17] C. Ospelkaus, U. Warring, Y. Colombe, K. R. Brown, J. M. Amini, D. Leibfried, and D. J. Wineland, "Microwave quantum logic gates for trapped ions," *Nature*, vol. 476, pp. 181–184, aug 2011.

[18] M. Mielenz, H. Kalis, M. Wittemer, F. Hakelberg, U. Warring, R. Schmied, M. Blain, P. Maunz, D. L. Moehring, D. Leibfried, and T. Schaetz, "Arrays of individually controlled ions suitable for two-dimensional quantum simulations," *Nature Communications*, vol. 7, p. ncomms11839, jun 2016.

[19] C.-w. Chou, C. Kurz, D. B. Hume, P. N. Plessow, D. R. Leibrandt, and D. Leibfried, "Preparation and coherent manipulation of pure quantum states of a single molecular ion," *Nature*, vol. 545, pp. 203–207, may 2017.

[20] T. Yamamoto, Y. A. Pashkin, O. Astafiev, Y. Nakamura, and J. S. Tsai, "Demonstration of conditional gate operation using superconducting charge qubits," *Nature*, vol. 425, pp. 941–944, oct 2003.

[21] I. Chiorescu, Y. Nakamura, C. J. P. M. Harmans, and J. E. Mooij, "Coherent Quantum Dynamics of a Superconducting Flux Qubit," *Science*, vol. 299, no. 5614, 2003.

[22] A. Wallraff, D. I. Schuster, A. Blais, L. Frunzio, R.-S. Huang, J. Majer, S. Kumar, S. M. Girvin, and R. J. Schoelkopf, "Strong coupling of a single photon to a superconducting qubit using circuit quantum electrodynamics," *Nature*, vol. 431, pp. 162–167, sep 2004.

[23] L. DiCarlo, J. M. Chow, J. M. Gambetta, L. S. Bishop, B. R. Johnson, D. I. Schuster, J. Majer, A. Blais, L. Frunzio, S. M. Girvin, and R. J. Schoelkopf, "Demonstration of two-qubit algorithms with a superconducting quantum processor," *Nature*, vol. 460, pp. 240–244, jul 2009.

[24] M. H. Devoret and R. J. Schoelkopf, "Superconducting Circuits for Quantum Information: An Outlook," *Science*, vol. 339, no. 6124, 2013.

[25] M. D. Shulman, O. E. Dial, S. P. Harvey, H. Bluhm, V. Umansky, and A. Yacoby, "Demonstration of Entanglement of Electrostatically Coupled Singlet-Triplet Qubits," *Science*, vol. 336, no. 6078, 2012.

[26] B. M. Maune, M. G. Borselli, B. Huang, T. D. Ladd, P. W. Deelman, K. S. Holabird, A. A. Kiselev, I. Alvarado-Rodriguez, R. S. Ross, A. E. Schmitz, M. Sokolich, C. A. Watson, M. F. Gyure, and A. T. Hunter, "Coherent singlet-triplet oscillations in a silicon-based double quantum dot," *Nature*, vol. 481, pp. 344–347, jan 2012.

[27] M. Yamamoto, S. Takada, C. Bäuerle, K. Watanabe, A. D. Wieck, and S. Tarucha, "Electrical control of a solid-state flying qubit," *Nature Nanotechnology*, vol. 7, pp. 247–251, mar 2012.

[28] B. E. Kane, "A silicon-based nuclear spin quantum computer," *Nature*, vol. 393, no. 6681, pp. 133–137, 1998.

[29] J. J. L. Morton, A. M. Tyryshkin, R. M. Brown, S. Shankar, B. W. Lovett, A. Ardavan, T. Schenkel, E. E. Haller, J. W. Ager, and S. A. Lyon, "Solid-state quantum memory using the 31P nuclear spin," *Nature*, vol. 455, pp. 1085–1088, oct 2008.

[30] A. Morello, J. J. Pla, F. A. Zwanenburg, K. W. Chan, K. Y. Tan, H. Huebl, M. Möttönen, C. D. Nugroho, C. Yang, J. A. van Donkelaar, A. D. C. Alves, D. N. Jamieson, C. C. Escott, L. C. L. Hollenberg, R. G. Clark, and A. S. Dzurak, "Single-shot readout of an electron spin in silicon," *Nature*, vol. 467, pp. 687–691, oct 2010.

[31] J. J. Pla, K. Y. Tan, J. P. Dehollain, W. H. Lim, J. J. L. Morton, D. N. Jamieson, A. S. Dzurak, and A. Morello, "A single-atom electron spin qubit in silicon," *Nature*, vol. 489, pp. 541–545, sep 2012.

[32] A. Imamoğlu, D. D. Awschalom, G. Burkard, D. P. DiVincenzo, D. Loss, M. Sherwin, and A. Small, "Quantum Information Processing Using Quantum Dot Spins and Cavity QED," *Physical Review Letters*, vol. 83, pp. 4204–4207, nov 1999.

[33] P. Michler, A. Kiraz, C. Becher, W. V. Schoenfeld, P. M. Petroff, L. Zhang, E. Hu, and A. Imamoğlu, "A Quantum Dot Single-Photon Turnstile Device," *Science*, vol. 290, no. 5500, 2000.

[34] X. Li, Y. Wu, D. Steel, D. Gammon, T. H. Stievater, D. S. Katzer, D. Park, C. Piermarocchi, and L. J. Sham, "An All-Optical Quantum Gate in a Semiconductor Quantum Dot," *Science*, vol. 301, no. 5634, 2003.

[35] M. Atatüre, J. Dreiser, A. Badolato, A. Högele, K. Karrai, and A. Imamoglu, "Quantum-Dot Spin-State Preparation with Near-Unity Fidelity," *Science*, vol. 312, no. 5773, 2006.

[36] D. Press, T. D. Ladd, B. Zhang, and Y. Yamamoto, "Complete quantum control of a single quantum dot spin using ultrafast optical pulses," *Nature, Published online: 13 November 2008; | doi:10.1038/nature07530*, vol. 456, no. 7219, p. 218, 2008.

[37] D. Press, K. De Greve, P. L. McMahon, T. D. Ladd, B. Friess, C. Schneider, M. Kamp, S. Höfling, A. Forchel, and Y. Yamamoto, "Ultrafast optical spin echo in a single quantum dot," *Nature Photonics*, vol. 4, pp. 367–370, jun 2010.

[38] A. Dousse, J. Suffczyński, A. Beveratos, O. Krebs, A. Lemaître, I. Sagnes, J. Bloch, P. Voisin, and P. Senellart, "Ultrabright source of entangled photon pairs," *Nature*, vol. 466, pp. 217–220, jul 2010.

[39] R. Stockill, M. J. Stanley, L. Huthmacher, E. Clarke, M. Hugues, A. J. Miller, C. Matthiesen, C. L. Gall, and M. Atatüre, "Phase-tuned entangled state generation between distant spin qubits," *Arxiv:1702.03422*, feb 2017.

[40] K. Saeedi, S. Simmons, J. Z. Salvail, P. Dluhy, H. Riemann, N. V. Abrosimov, P. Becker, H.-J. Pohl, J. J. L. Morton, and M. L. W. Thewalt, "Room-Temperature Quantum Bit Storage Exceeding 39 Minutes Using Ionized Donors in Silicon-28," *Science*, vol. 342, no. 6160, 2013.

[41] C. Yin, M. Rancic, G. G. de Boo, N. Stavrias, J. C. McCallum, M. J. Sellars, and S. Rogge, "Optical addressing of an individual erbium ion in silicon," *Nature*, vol. 497, pp. 91–94, may 2013.

[42] K. De Greve, P. L. McMahon, D. Press, T. D. Ladd, D. Bisping, C. Schneider, M. Kamp, L. Worschech, S. Höfling, A. Forchel, and Y. Yamamoto, "Ultrafast coherent control and suppressed nuclear feedback of a single quantum dot hole qubit," *Nature Physics*, vol. 7, pp. 872–878, aug 2011.

[43] M. J. Stanley, C. Matthiesen, J. Hansom, C. Le Gall, C. H. H. Schulte, E. Clarke, and M. Atatüre, "Dynamics of a mesoscopic nuclear spin ensemble interacting with an optically driven electron spin," *Physical Review B*, vol. 90, p. 195305, nov 2014.

[44] R. Stockill, C. Le Gall, C. Matthiesen, L. Huthmacher, E. Clarke, M. Hugues, and M. Atatüre, "Quantum dot spin coherence governed by a strained nuclear environment," *Nature Communications*, vol. 7, p. 12745, sep 2016.

[45] G. L. Harris, *Properties of Silicon Carbide*. INSPEC, United Kingdom, 1995.

[46] P. Klimov, A. Falk, B. Buckley, and D. Awschalom, "Electrically Driven Spin Resonance in Silicon Carbide Color Centers," *Physical Review Letters*, vol. 112, p. 087601, feb 2014.

[47] A. L. Falk, P. V. Klimov, B. B. Buckley, V. Ivády, I. A. Abrikosov, G. Calusine, W. F. Koehl, Á. Gali, and D. D. Awschalom, "Electrically and Mechanically Tunable Electron Spins in Silicon Carbide Color Centers," *Physical Review Letters*, vol. 112, p. 187601, may 2014.

[48] A. M. Zaitsev, *Optical Properties of Diamond*. Berlin, Heidelberg: Springer Berlin Heidelberg, 2001.

[49] F. Jelezko and J. Wrachtrup, "Single defect centres in diamond: A review," *physica status solidi (a)*, vol. 203, pp. 3207–3225, oct 2006.

[50] I. Aharonovich and E. Neu, "Diamond Nanophotonics," *Advanced Optical Materials*, vol. 2, pp. 911–928, oct 2014.

[51] L. Wei, P. K. Kuo, R. L. Thomas, T. R. Anthony, and W. F. Banholzer, "Thermal conductivity of isotopically modified single crystal diamond," *Physical Review Letters*, vol. 70, pp. 3764–3767, jun 1993.

[52] I. Aharonovich, A. D. Greentree, and S. Prawer, "Diamond photonics," *Nature Photonics*, vol. 5, 2011.

[53] B. J. M. Hausmann, B. Shields, Q. Quan, P. Maletinsky, M. McCutcheon, J. T. Choy, T. M. Babinec, A. Kubanek, A. Yacoby, M. D. Lukin, and M. LoncÌ†ar, "Integrated Diamond Networks for Quantum Nanophotonics," *Nano Letters*, vol. 12, pp. 1578–1582, mar 2012.

[54] B. J. M. Hausmann, I. Bulu, V. Venkataraman, P. Deotare, and M. Lončar, "Diamond nonlinear photonics," *Nature Photonics*, vol. 8, pp. 369–374, apr 2014.

[55] F. Neugart, A. Zappe, F. Jelezko, C. Tietz, J. P. Boudou, A. Krueger, and J. Wrachtrup, "Dynamics of diamond nanoparticles in solution and cells," *Nano Letters*, vol. 7, no. 12, pp. 3588–3591, 2007.

[56] Y.-R. Chang, H.-Y. Lee, K. Chen, C.-C. Chang, D.-S. Tsai, C.-C. Fu, T.-S. Lim, Y.-K. Tzeng, C.-Y. Fang, C.-C. Han, H.-C. Chang, and W. Fann, "Mass production and dynamic imaging of fluorescent nanodiamonds," *Nature Nanotechnology*, vol. 3, pp. 284–288, may 2008.

[57] O. Faklaris, V. Joshi, T. Irinopoulou, P. Tauc, M. Sennour, H. Girard, C. Gesset, J.-C. Arnault, A. Thorel, J.-P. Boudou, P. A. Curmi, and F. Treussart, "Photoluminescent Diamond Nanoparticles for Cell Labeling: Study of the Uptake Mechanism in Mammalian Cells," *ACS Nano*, vol. 3, pp. 3955–3962, dec 2009.

[58] A. Härtl, E. Schmich, J. A. Garrido, J. Hernando, S. C. R. Catharino, S. Walter, P. Feulner, A. Kromka, D. Steinmüller, and M. Stutzmann, "Protein-modified nanocrystalline diamond thin films for biosensor applications," *Nature Materials*, vol. 3, pp. 736–742, oct 2004.

[59] J. Wang, M. A. Firestone, O. Auciello, and J. A. Carlisle, "Surface Functionalization of Ultrananocrystalline Diamond Films by Electrochemical Reduction of Aryldiazonium Salts," *Langmuir*, vol. 20, pp. 11450–11456, dec 2004.

[60] V. Acosta and P. Hemmer, "Nitrogen-vacancy centers: Physics and applications," *MRS Bulletin*, vol. 38, pp. 127–130, feb 2013.

[61] L. Childress and R. Hanson, "Diamond NV centers for quantum computing and quantum networks," *MRS Bulletin*, vol. 38, pp. 134–138, feb 2013.

[62] M. Lončar and A. Faraon, "Quantum photonic networks in diamond," *MRS Bulletin*, vol. 38, pp. 144–148, feb 2013.

[63] S. Hong, M. S. Grinolds, L. M. Pham, D. Le Sage, L. Luan, R. L. Walsworth, and A. Yacoby, "Nanoscale magnetometry with NV centers in diamond," *MRS Bulletin*, vol. 38, pp. 155–161, feb 2013.

[64] E. Togan, Y. Chu, A. S. Trifonov, L. Jiang, J. Maze, L. Childress, M. V. G. Dutt, A. S. Sorensen, P. R. Hemmer, A. S. Zibrov, and M. D. Lukin, "Quantum entanglement between an optical photon and a solid-state spin qubit," *Nature*, vol. 466, no. 7307, pp. 730—-U4, 2010.

[65] H. Bernien, B. Hensen, W. Pfaff, G. Koolstra, M. S. Blok, L. Robledo, T. H. Taminiau, M. Markham, D. J. Twitchen, L. Childress, and R. Hanson, "Heralded entanglement between solid-state qubits separated by three metres," *Nature*, vol. 497, pp. 86–90, apr 2013.

[66] B. Hensen, H. Bernien, A. E. Dréau, A. Reiserer, N. Kalb, M. S. Blok, J. Ruitenberg, R. F. L. Vermeulen, R. N. Schouten, C. Abellán, W. Amaya, V. Pruneri, M. W. Mitchell, M. Markham, D. J. Twitchen, D. Elkouss, S. Wehner, T. H. Taminiau, and R. Hanson, "Loophole-free Bell inequality violation using electron spins separated by 1.3 kilometres," *Nature*, vol. 526, pp. 682–686, oct 2015.

[67] P. Neumann, N. Mizuochi, F. Rempp, P. Hemmer, H. Watanabe, S. Yamasaki, V. Jacques, T. Gaebel, F. Jelezko, and J. Wrachtrup, "Multipartite Entanglement Among Single Spins in Diamond," *Science*, vol. 320, no. 5881, 2008.

[68] W. Pfaff, T. H. Taminiau, L. Robledo, H. Bernien, M. Markham, D. J. Twitchen, and R. Hanson, "Demonstration of entanglement-by-measurement of solid-state qubits," *Nature Physics*, vol. 9, no. 1, pp. 29–33, 2013.

[69] F. Jelezko, T. Gaebel, I. Popa, M. Domhan, A. Gruber, and J. Wrachtrup, "Observation of Coherent Oscillation of a Single Nuclear Spin and Realization of a Two-Qubit Conditional Quantum Gate," *Physical Review Letters*, vol. 93, p. 130501, sep 2004.

[70] L. Childress, M. V. G. Dutt, J. M. Taylor, A. S. Zibrov, F. Jelezko, J. Wrachtrup, P. R. Hemmer, and M. D. Lukin, "Coherent dynamics of coupled electron and nuclear spin qubits in diamond," *Science*, vol. 314, no. 5797, pp. 281–285, 2006.

[71] M. V. G. Dutt, L. Childress, L. Jiang, E. Togan, J. Maze, F. Jelezko, A. S. Zibrov, P. R. Hemmer, and M. D. Lukin, "Quantum register based on individual electronic and nuclear spin qubits in diamond," *Science*, vol. 316, no. 5829, pp. 1312–1316, 2007.

[72] T. H. Taminiau, J. J. T. Wagenaar, T. van der Sar, F. Jelezko, V. V. Dobrovitski, and R. Hanson, "Detection and Control of Individual Nuclear Spins Using a Weakly Coupled Electron Spin," *Physical Review Letters*, vol. 109, p. 137602, sep 2012.

[73] G. D. Fuchs, G. Burkard, P. V. Klimov, and D. D. Awschalom, "A quantum memory intrinsic to single nitrogenâ€"vacancy centres in diamond," *Nature Physics*, vol. 7, pp. 789–793, jun 2011.

[74] L. Jiang, J. S. Hodges, J. R. Maze, P. Maurer, J. M. Taylor, D. G. Cory, P. R. Hemmer, R. L. Walsworth, A. Yacoby, A. S. Zibrov, and M. D. Lukin, "Repetitive Readout of a Single Electronic Spin via Quantum Logic with Nuclear Spin Ancillae," *Science*, vol. 326, no. 5950, 2009.

[75] F. Dolde, H. Fedder, M. W. Doherty, T. Nöbauer, F. Rempp, G. Balasubramanian, T. Wolf, F. Reinhard, L. C. L. Hollenberg, F. Jelezko, and J. Wrachtrup, "Electric-field sensing using single diamond spins," *Nature Physics*, vol. 7, pp. 459–463, jun 2011.

[76] J. R. Maze, P. L. Stanwix, J. S. Hodges, S. Hong, J. M. Taylor, P. Cappellaro, L. Jiang, M. V. G. Dutt, E. Togan, A. S. Zibrov, A. Yacoby, R. L. Walsworth, and M. D. Lukin, "Nanoscale magnetic sensing with an individual electronic spin in diamond," *Nature*, vol. 455, no. 7213, pp. 644—-U41, 2008.

[77] M. S. Grinolds, S. Hong, P. Maletinsky, L. Luan, M. D. Lukin, R. L. Walsworth, and A. Yacoby, "Nanoscale magnetic imaging of a single electron spin under ambient conditions," *Nature Physics*, vol. 9, pp. 215–219, feb 2013.

[78] H. J. Mamin, M. Kim, M. H. Sherwood, C. T. Rettner, K. Ohno, D. D. Awschalom, and D. Rugar, "Nanoscale Nuclear Magnetic Resonance with a Nitrogen-Vacancy Spin Sensor," *Science*, vol. 339, no. 6119, 2013.

[79] T. Staudacher, F. Shi, S. Pezzagna, J. Meijer, J. Du, C. A. Meriles, F. Reinhard, and J. Wrachtrup, "Nuclear Magnetic Resonance Spectroscopy on a (5-Nanometer)3 Sample Volume," *Science*, vol. 339, no. 6119, 2013.

[80] G. Kucsko, P. C. Maurer, N. Y. Yao, M. Kubo, H. J. Noh, P. K. Lo, H. Park, and M. D. Lukin, "Nanometre-scale thermometry in a living cell," *Nature*, vol. 500, pp. 54–58, jul 2013.

[81] D. M. Toyli, C. F. de las Casas, D. J. Christle, V. V. Dobrovitski, and D. D. Awschalom, "Fluorescence thermometry enhanced by the quantum coherence of single spins in diamond.," *Proceedings of the National Academy of Sciences of the United States of America*, vol. 110, pp. 8417–21, may 2013.

[82] T. Plakhotnik, M. W. Doherty, J. H. Cole, R. Chapman, and N. B. Manson, "All-Optical Thermometry and Thermal Properties of the Optically Detected Spin Resonances of the NV^- Center in Nanodiamond," *Nano Letters*, vol. 14, pp. 4989–4996, sep 2014.

[83] L. P. McGuinness, Y. Yan, A. Stacey, D. A. Simpson, L. T. Hall, D. Maclaurin, S. Prawer, P. Mulvaney, J. Wrachtrup, F. Caruso, R. E. Scholten, and L. C. L. Hollenberg, "Quantum measurement and orientation tracking of fluorescent nanodiamonds inside living cells," *Nature Nanotechnology*, vol. 6, pp. 358–363, jun 2011.

[84] L. T. Hall, G. C. G. Beart, E. A. Thomas, D. A. Simpson, L. P. McGuinness, J. H. Cole, J. H. Manton, R. E. Scholten, F. Jelezko, J. Wrachtrup, S. Petrou, and L. C. L. Hollenberg, "High spatial and temporal resolution wide-field imaging of neuron activity using quantum NV-diamond," *Scientific Reports*, vol. 2, pp. 281–285, may 2012.

[85] D. Riedel, I. Söllner, B. J. Shields, S. Starosielec, P. Appel, E. Neu, P. Maletinsky, and R. J. Warburton, "Deterministic enhancement of coherent photon generation from a nitrogen-vacancy center in ultrapure diamond," *Arxiv:1703.00815*, mar 2017.

[86] H. J. Kimble, "The quantum internet," *Nature*, vol. 453, pp. 1023–1030, jun 2008.

[87] A. T. Collins, M. Kamo, and Y. Sato, "A Spectroscopic Study of Optical-centers In Diamond Grown By Microwave-assisted Chemical Vapor-deposition," *Journal of Materials Research*, vol. 5, no. 11, pp. 2507–2514, 1990.

[88] J. Ruan, W. J. Choyke, and W. D. Partlow, "Si Impurity In Chemical Vapor-deposited Diamond Films," *Applied Physics Letters*, vol. 58, no. 3, pp. 295–297, 1991.

[89] H. Sternschulte, K. Thonke, R. Sauer, P. C. Munzinger, and P. Michler, "1.681-ev Luminescence Center In Chemical-vapor-deposited Homoepitaxial Diamond Films," *Physical Review B*, vol. 50, no. 19, pp. 14554–14560, 1994.

[90] C. D. Clark, H. Kanda, I. Kiflawi, and G. Sittas, "Silicon Defects In Diamond," *Physical Review B*, vol. 51, no. 23, pp. 16681–16688, 1995.

[91] A. Dietrich, T. Teraji, J. Isoya, L. J. Rogers, and F. Jelezko, "Isotopically varying spectral features of silicon-vacancy in diamond," *New J. Phys.*, vol. 16, no. 16, p. 113019, 2014.

[92] C. Clark and C. Dickerson, "The 1.681 eV centre in polycrystalline diamond," *Surface and Coatings Technology*, vol. 47, pp. 336–343, aug 1991.

[93] A. T. Collins, L. Allers, C. J. H. Wort, and G. A. Scarsbrook, "The Annealing of Radiation-damage In Debeers Colorless Cvd Diamond," *Diamond and Related Materials*, vol. 3, no. 4-6, pp. 932–935, 1994.

[94] E. Neu, D. Steinmetz, J. Riedrich-Möller, S. Gsell, M. Fischer, M. Schreck, and C. Becher, "Single photon emission from silicon-vacancy colour centres in chemical vapour deposition nano-diamonds on iridium," *New Journal of Physics*, vol. 13, no. 2, pp. 025012—-, 2011.

[95] J. P. Goss, R. Jones, S. J. Breuer, P. R. Briddon, and S. Oberg, "The twelve-line 1.682eV luminescence center in diamond and the vacancy-silicon complex," *Physical Review Letters*, vol. 77, no. 14, pp. 3041–3044, 1996.

[96] J. P. Goss, P. R. Briddon, and M. J. Shaw, "Density functional simulations of silicon-containing point defects in diamond," *Physical Review B*, vol. 76, no. 7, p. 75204, 2007.

[97] U. F. S. D'Haenens-Johansson, A. M. Edmonds, B. L. Green, M. E. Newton, G. Davies, P. M. Martineau, R. U. A. Khan, and D. J. Twitchen, "Optical properties of the neutral silicon split-vacancy center in diamond," *Physical Review B*, vol. 84, no. 24, p. 245208, 2011.

[98] S. S. Moliver, "Electronic structure of neutral silicon-vacancy complex in diamond," *Technical Physics*, vol. 48, no. 11, pp. 1449–1453, 2003.

[99] A. Gali and J. R. Maze, "Ab initio study of the split silicon-vacancy defect in diamond: Electronic structure and related properties," *Physical Review B*, vol. 88, p. 235205, dec 2013.

[100] J. P. Goss, P. R. Briddon, R. Jones, and S. Sque, "Donor and acceptor states in diamond," *Diamond and Related Materials*, vol. 13, no. 4-8, pp. 684–690, 2004.

[101] R. Larico, W. V. M. Machado, J. F. Justo, and L. V. C. Assali, "Microscopic structure of nickel-dopant centers in diamond," *Brazilian Journal of Physics*, vol. 36, no. 2A, pp. 267–269, 2006.

[102] L. V. C. Assali, W. V. M. Machado, R. Larico, and J. F. Justo, "Cobalt in diamond: An ab initio investigation," *Diamond and Related Materials*, vol. 16, no. 4-7, pp. 819–822, 2007.

[103] T. Iwasaki, F. Ishibashi, Y. Miyamoto, Y. Doi, S. Kobayashi, T. Miyazaki, K. Tahara, K. D. Jahnke, L. J. Rogers, B. Naydenov, F. Jelezko, S. Yamasaki, S. Nagamachi, T. Inubushi, N. Mizuochi, and M. Hatano, "Germanium-Vacancy Single Color Centers in Diamond.," *Scientific reports*, vol. 5, p. 12882, aug 2015.

[104] Y. N. Palyanov, I. N. Kupriyanov, Y. M. Borzdov, and N. V. Surovtsev, "Germanium: a new catalyst for diamond synthesis and a new optically active impurity in diamond," *Scientific Reports*, vol. 5, p. 14789, oct 2015.

[105] K. Iakoubovskii, G. Adriaenssens, M. Nesládek, and L. Stals, "Photoluminescence excitation and quenching spectra in CVD diamond films," *Diamond and Related Materials*, vol. 8, pp. 717–720, mar 1999.

[106] H. P. Bovenkerk, F. P. Bundy, H. T. Hall, H. M. Strong, and R. H. Wentorf, "Preparation of Diamond," *Nature*, vol. 184, pp. 1094–1098, oct 1959.

[107] T. Teraji, "Chemical vapor deposition of homoepitaxial diamond films," *physica status solidi (a)*, vol. 203, pp. 3324–3357, oct 2006.

[108] M. S. Dresselhaus and R. Kalish, *Ion Implantation in Diamond, Graphite and Related Materials*. Springer Science & Business Media, 2013.

[109] J. F. Ziegler, M. Ziegler, and J. Biersack, "Srim - the stopping and range of ions in matter (2010)," *Nuclear Instruments and Methods in Physics Research Section B: Beam Interactions with Materials and Atoms*, vol. 268, no. 11, pp. 1818–1823, 2010.

[110] L. Bergman, B. R. Stoner, K. F. Turner, J. T. Glass, and R. J. Nemanich, "Microphotoluminescence and Raman scattering study of defect formation in diamond films," *Journal of Applied Physics*, vol. 73, pp. 3951–3957, apr 1993.

[111] T. Feng and B. D. Schwartz, "Characteristics and Origin of the 1.681 Ev Luminescence Center In Chemical-vapor-deposited Diamond Films," *Journal of Applied Physics*, vol. 73, no. 3, pp. 1415–1425, 1993.

[112] J. Barjon, E. Rzepka, F. Jomard, J. M. Laroche, D. Ballutaud, T. Kociniewski, and J. Chevallier, "Silicon incorporation in CVD diamond layers," *Physica Status Solidi A-applications and Materials Science*, vol. 202, no. 11, pp. 2177–2181, 2005.

[113] J. P. Goss, R. Jones, S. J. Breuer, P. R. Briddon, and S. Öberg, "The Twelve-Line 1.682 eV Luminescence Center in Diamond and the Vacancy-Silicon Complex," *Physical Review Letters*, vol. 77, pp. 3041–3044, sep 1996.

[114] W. Saslow, T. K. Bergstresser, and M. L. Cohen, "Band Structure and Optical Properties of Diamond," *Physical Review Letters*, vol. 16, pp. 354–356, feb 1966.

[115] E. Neu, M. Agio, and C. Becher, "Photophysics of single silicon vacancy centers in diamond: implications for single photon emission," *Optics Express*, vol. 20, no. 18, pp. 19956–19971, 2012.

[116] R. E. Evans, A. Sipahigil, D. D. Sukachev, A. S. Zibrov, and M. D. Lukin, "Narrow-Linewidth Homogeneous Optical Emitters in Diamond Nanostructures via Silicon Ion Implantation," *Physical Review Applied*, vol. 5, p. 044010, apr 2016.

[117] Y. Chu, N. de Leon, B. Shields, B. Hausmann, R. Evans, E. Togan, M. J. Burek, M. Markham, A. Stacey, A. Zibrov, A. Yacoby, D. Twitchen, M. Loncar, H. Park, P. Maletinsky, and M. Lukin, "Coherent Optical Transitions in Implanted Nitrogen Vacancy Centers," *Nano Letters*, vol. 14, pp. 1982–1986, apr 2014.

[118] A. T. Collins, M. F. Thomaz, and M. I. B. Jorge, "Luminescence decay time of the 1.945 eV centre in type Ib diamond," *Journal of Physics C: Solid State Physics*, vol. 16, pp. 2177–2181, apr 1983.

[119] G. Davies, "The Jahn-Teller effect and vibronic coupling at deep levels in diamond," *Reports on Progress in Physics*, vol. 44, pp. 787–830, jul 1981.

[120] J. Walker, "Optical absorption and luminescence in diamond," *Reports on Progress in Physics*, vol. 42, pp. 1605–1659, oct 1979.

[121] A. A. Gorokhovsky, A. V. Turukhin, R. R. Alfano, and W. Phillips, "Photoluminescence Vibrational Structure of Si Center In Chemical-vapor-deposited Diamond," *Applied Physics Letters*, vol. 66, no. 1, pp. 43–45, 1995.

[122] K. Iakoubovskii, G. J. Adriaenssens, N. N. Dogadkin, and A. A. Shiryaev, "Optical characterization of some irradiation-induced centers in diamond," *Diamond and Related Materials*, vol. 10, no. 1, pp. 18–26, 2001.

[123] E. Neu, M. Fischer, S. Gsell, M. Schreck, and C. Becher, "Fluorescence and polarization spectroscopy of single silicon vacancy centers in heteroepitaxial nanodiamonds on iridium," *Physical Review B*, vol. 84, no. 20, p. 205211, 2011.

[124] A. M. Zaitsev, "Vibronic spectra of impurity-related optical centers in diamond," *Physical Review B*, vol. 61, no. 19, pp. 12909–12922, 2000.

[125] H. Bernien, L. Childress, L. Robledo, M. Markham, D. Twitchen, and R. Hanson, "Two-Photon Quantum Interference from Separate Nitrogen Vacancy Centers in Diamond," *Physical Review Letters*, vol. 108, p. 043604, jan 2012.

[126] T. G. Bilodeau, K. Doverspike, U. Strom, J. A. Freitas, and R. Rameshan, "Calorimetric Absorption-spectroscopy and Photoluminescence Study of Defects In Diamond," *Diamond and Related Materials*, vol. 2, no. 5-7, pp. 699–703, 1993.

[127] A. V. Turukhin, C. H. Liu, A. A. Gorokhovsky, R. R. Alfano, and W. Phillips, "Picosecond photoluminescence decay of Si-doped chemical-vapor-deposited diamond films," *Physical Review B*, vol. 54, no. 23, pp. 16448–16451, 1996.

[128] A. Sipahigil, R. E. Evans, D. D. Sukachev, M. J. Burek, J. Borregaard, M. K. Bhaskar, C. T. Nguyen, J. L. Pacheco, H. A. Atikian, C. Meuwly, R. M. Camacho, F. Jelezko, E. Bielejec, H. Park, M. Lončar, and M. D. Lukin, "An integrated diamond nanophotonics platform for quantum-optical networks," *Science*, vol. 354, no. 6314, 2016.

[129] S. A. Grudinkin, N. A. Feoktistov, A. V. Medvedev, K. V. Bogdanov, A. V. Baranov, A. Y. Vul', and V. G. Golubev, "Luminescent isolated diamond particles with controllably embedded silicon-vacancy colour centres," *Journal of Physics D-applied Physics*, vol. 45, no. 6, p. 62001, 2012.

[130] K. D. Jahnke, A. Sipahigil, J. M. Binder, M. W. Doherty, M. Metsch, L. J. Rogers, N. B. Manson, M. D. Lukin, and F. Jelezko, "Electronâ€"phonon processes of the silicon-vacancy centre in diamond," *New Journal of Physics*, vol. 17, p. 043011, apr 2015.

[131] C. Kurtsiefer, S. Mayer, P. Zarda, and H. Weinfurter, "Stable Solid-State Source of Single Photons," *Physical Review Letters*, vol. 85, pp. 290–293, jul 2000.

[132] J. Wrachtrup and F. Jelezko, "Processing quantum information in diamond," *Journal of Physics-condensed Matter*, vol. 18, no. 21, pp. S807—-S824, 2006.

[133] E. Neu, C. Hepp, M. Hauschild, S. Gsell, M. Fischer, H. Sternschulte, D. Steinmüller-Nethl, M. Schreck, and C. Becher, "Low-temperature investigations of single silicon vacancy colour centres in diamond," *New J. Phys.*, vol. 15, no. 15, 2013.

[134] S. W. Brown and S. C. Rand, "Site Symmetry Analysis of the 738 Nm Defect In Diamond," *Journal of Applied Physics*, vol. 78, no. 6, pp. 4069–4075, 1995.

[135] H. Sternschulte, K. Thonke, J. Gerster, W. Limmer, R. Sauer, J. Spitzer, and P. C. Munzinger, "Uniaxial-stress and Zeeman Splitting of the 1.681 Ev Optical-center In A Homoepitaxial Cvd Diamond Film," *Diamond and Related Materials*, vol. 4, no. 10, pp. 1189–1192, 1995.

[136] A. Sipahigil, K. Jahnke, L. Rogers, T. Teraji, J. Isoya, A. Zibrov, F. Jelezko, and M. Lukin, "Indistinguishable Photons from Separated Silicon-Vacancy Centers in Diamond," *Physical Review Letters*, vol. 113, p. 113602, sep 2014.

[137] L. Rogers, K. Jahnke, T. Teraji, L. Marseglia, C. Müller, B. Naydenov, H. Schauffert, C. Kranz, J. Isoya, L. McGuinness, and F. Jelezko, "Multiple intrinsically identical single-photon emitters in the solid state," *Nature Communications*, vol. 5, p. 4739, aug 2014.

[138] T. Schröder, M. E. Trusheim, M. Walsh, L. Li, J. Zheng, M. Schukraft, A. Sipahigil, R. E. Evans, D. D. Sukachev, C. T. Nguyen, J. L. Pacheco, R. M. Camacho, E. S. Bielejec, M. D. Lukin, and D. Englund, "Scalable focused ion beam creation of nearly lifetime-limited single quantum emitters in diamond nanostructures," *Nature Communications*, vol. 8, p. 15376, may 2017.

[139] M. J. Burek, C. Meuwly, R. E. Evans, M. K. Bhaskar, A. Sipahigil, S. Meesala, D. D. Sukachev, C. T. Nguyen, J. L. Pacheco, E. Bielejec, M. D. Lukin, M. Lončar, A. John, and D. P. N. Lebedev, "A fiber-coupled diamond quantum nanophotonic interface," *Arxiv:1612.05285*, 2016.

[140] K. Iakoubovskii and A. Stesmans, "Characterization of hydrogen and silicon-related defects in CVD diamond by electron spin resonance," *Physical Review B*, vol. 66, no. 19, p. 195207, 2002.

[141] X. B. Zhu, S. Saito, A. Kemp, K. Kakuyanagi, S. Karimoto, H. Nakano, W. J. Munro, Y. Tokura, M. S. Everitt, K. Nemoto, M. Kasu, N. Mizuochi, and K. Semba, "Coherent coupling of a superconducting flux qubit to an electron spin ensemble in diamond," *Nature*, vol. 478, no. 7368, pp. 221–224, 2011.

[142] Y. Kubo, C. Grezes, A. Dewes, T. Umeda, J. Isoya, H. Sumiya, N. Morishita, H. Abe, S. Onoda, T. Ohshima, V. Jacques, A. Dréau, J.-F. Roch, I. Diniz, A. Auffeves, D. Vion, D. Esteve, and P. Bertet, "Hybrid Quantum Circuit with a Superconducting Qubit Coupled to a Spin Ensemble," *Physical Review Letters*, vol. 107, p. 220501, nov 2011.

[143] T. van der Sar, Z. H. Wang, M. S. Blok, H. Bernien, T. H. Taminiau, D. M. Toyli, D. A. Lidar, D. D. Awschalom, R. Hanson, and V. V. Dobrovitski, "Decoherence-protected quantum gates for a hybrid solid-state spin register," *Nature*, vol. 484, no. 7392, pp. 82–86, 2012.

[144] T. Müller, C. Hepp, B. Pingault, E. Neu, S. Gsell, M. Schreck, H. Sternschulte, D. Steinmüller-Nethl, C. Becher, and M. Atatüre, "Optical signatures of silicon-vacancy spins in diamond," *Nature Communications*, vol. 5, p. 083002, feb 2014.

[145] B. Pingault, J. N. Becker, C. H. Schulte, C. Arend, C. Hepp, T. Godde, A. I. Tartakovskii, M. Markham, C. Becher, and M. Atatüre, "All-Optical Formation of Coherent Dark States of Silicon-Vacancy Spins in Diamond," *Physical Review Letters*, vol. 113, p. 263601, dec 2014.

[146] C. Matthiesen, A. N. Vamivakas, and M. Atatüre, "Subnatural Linewidth Single Photons from a Quantum Dot," *Phys. Rev. Lett.*, vol. 108, p. 93602, 2012.

[147] E. Neu, F. Guldner, C. Arend, Y. Liang, S. Ghodbane, H. Sternschulte, D. Steinmüller-Nethl, A. Krueger, and Becher, "Low temperature iinvestigation and surface treatments of colloidal narrowband fluorescent nanodiamonds," *ArXiv: 1302.3188v1*, 2013.

[148] C. Hepp, T. Müller, V. Waselowski, J. N. Becker, B. Pingault, H. Sternschulte, D. Steinmüller-Nethl, A. Gali, J. R. Maze, M. Atatüre, and C. Becher, "Electronic Structure of the Silicon Vacancy Color Center in Diamond," *Physical Review Letters*, vol. 112, p. 036405, jan 2014.

[149] C. J. Hepp, *Electronic structure of the silicon-vacancy color center in diamond*. PhD thesis, Universität des Saarlandes, 2014.

[150] M. S. Dresselhaus, G. Dresselhaus, and A. Jorio, *Group Theory: Application to the Physics of Condensed Matter*. Springer-Verlag Berlin, 2008.

[151] M. Tinkham, *Group Theory and Quantum Mechanics*. Dover Publications, Inc., Mineola, New York, 1964.

[152] F. S. Ham, "Dynamical Jahn-Teller Effect in Paramagnetic Resonance Spectra: Orbital Reduction Factors and Partial Quenching of Spin-Orbit Interaction," *Physical Review*, vol. 138, pp. A1727–A1740, jun 1965.

[153] E. Tosatti, N. Manini, and O. Gunnarsson, "Surprises in the orbital magnetic moment and g factor of the dynamic Jahn-Teller ion C 60," *Physical Review B*, vol. 54, pp. 17184–17190, dec 1996.

[154] C. J. Foot, *Atomic Physics*. Oxford University Press, 2005.

[155] M. Fleischhauer, A. Imamoğlu, and J. P. Marangos, "Electromagnetically induced transparency: Optics in coherent media," *Reviews of Modern Physics*, vol. 77, pp. 633–673, jul 2005.

[156] R. Loudon, *The Quantum Theory of Light*. Oxford University Press, 1973.

[157] J. P. Hadden, J. P. Harrison, A. C. Stanley-Clarke, L. Marseglia, Y.-L. D. Ho, B. R. Patton, J. L. O'Brien, and J. G. Rarity, "Strongly enhanced photon collection from diamond defect centers under microfabricated integrated solid immersion lenses," *Applied Physics Letters*, vol. 97, p. 241901, dec 2010.

[158] L. Marseglia, J. P. Hadden, A. C. Stanley-Clarke, J. P. Harrison, B. Patton, Y.-L. D. Ho, B. Naydenov, F. Jelezko, J. Meijer, P. R. Dolan, J. M. Smith, J. G. Rarity, and J. L. O'Brien, "Nanofabricated solid immersion lenses registered to single emitters in diamond," *Applied Physics Letters*, vol. 98, p. 133107, mar 2011.

[159] A. Lazoudis, T. Kirova, E. H. Ahmed, L. Li, J. Qi, and A. M. Lyyra, "Electromagnetically induced transparency in an open Λ -type molecular lithium system," *Physical Review A*, vol. 82, p. 023812, aug 2010.

[160] J. D. Pritchard, *Cooperative Optical Non-linearity in a blockaded Rydberg Ensemble*. PhD thesis, Durham University, 2011.

[161] H. J. Carmichael, *Statistical Methods in Quantum Optics 1 : Master Equations and Fokker-Planck Equations*. Springer Berlin Heidelberg, 1999.

[162] C. Santori, P. Tamarat, P. Neumann, J. Wrachtrup, D. Fattal, R. G. Beausoleil, J. Rabeau, P. Olivero, A. D. Greentree, S. Prawer, F. Jelezko, and P. Hemmer, "Coherent Population Trapping of Single Spins in Diamond under Optical Excitation," *Physical Review Letters*, vol. 97, p. 247401, dec 2006.

[163] C. G. Yale, B. B. Buckley, D. J. Christle, G. Burkard, F. J. Heremans, L. C. Bassett, and D. D. Awschalom, "All-optical control of a solid-state spin using coherent dark states.," *Proceedings of the National Academy of Sciences of the United States of America*, vol. 110, pp. 7595–600, may 2013.

[164] J. Hansom, C. H. H. Schulte, C. Le Gall, C. Matthiesen, E. Clarke, M. Hugues, J. M. Taylor, and M. Atatüre, "Environment-assisted quantum control of a solid-state spin via coherent dark states," *Nature Physics*, sep 2014.

[165] D. A. Golter and H. Wang, "Optically Driven Rabi Oscillations and Adiabatic Passage of Single Electron Spins in Diamond," *Physical Review Letters*, vol. 112, p. 116403, mar 2014.

[166] B. Pingault, D.-D. Jarausch, C. Hepp, L. Klintberg, J. N. Becker, M. Markham, C. Becher, and M. Atatüre, "Coherent control of the silicon-vacancy spin in diamond," *Nature Communications*, vol. 8, p. 15579, may 2017.

[167] J.-P. Tetienne, L. Rondin, P. Spinicelli, M. Chipaux, T. Debuisschert, J.-F. Roch, and V. Jacques, "Magnetic-field-dependent photodynamics of single NV defects in diamond: an application to qualitative all-optical magnetic imaging," *New Journal of Physics*, vol. 14, p. 103033, oct 2012.

[168] M. Steiner, P. Neumann, J. Beck, F. Jelezko, and J. Wrachtrup, "Universal enhancement of the optical readout fidelity of single electron spins at nitrogen-vacancy centers in diamond," *Physical Review B - Condensed Matter and Materials Physics*, vol. 81, no. 3, pp. 1–6, 2010.

[169] M. W. Doherty, N. B. Manson, P. Delaney, F. Jelezko, J. Wrachtrup, and L. C. Hollenberg, "The nitrogen-vacancy colour centre in diamond," *Physics Reports*, vol. 528, no. 1, pp. 1–45, 2013.

[170] L. Robledo, L. Childress, H. Bernien, B. Hensen, P. F. A. Alkemade, and R. Hanson, "High-fidelity projective read-out of a solid-state spin quantum register," *Nature*, vol. 477, pp. 574–578, sep 2011.

[171] L. J. Rogers, K. D. Jahnke, M. H. Metsch, A. Sipahigil, J. M. Binder, T. Teraji, H. Sumiya, J. Isoya, M. D. Lukin, P. Hemmer, and F. Jelezko, "All-optical initialization, readout, and coherent preparation of single silicon-vacancy spins in diamond," *Physical Review Letters*, vol. 113, no. 26, pp. 1–5, 2014.

[172] K. Bayat, J. Choy, A. V. Shneidman, S. Meesala, M. Farrokh Baroughi, and M. Loncar, "Uniform and large volume microwave magnetic coupling to NV centers in diamond using split ring resonators," *Cleo: 2014*, p. JW2A.130, 2014.

[173] G. D. Fuchs, V. V. Dobrovitski, D. M. Toyli, F. J. Heremans, and D. D. Awschalom, "Gigahertz dynamics of a strongly driven single quantum spin.," *Science (New York, N.Y.)*, vol. 326, pp. 1520–2, dec 2009.

[174] J. Scheuer, X. Kong, R. S. Said, J. Chen, A. Kurz, L. Marseglia, J. Du, P. R. Hemmer, S. Montangero, T. Calarco, B. Naydenov, and F. Jelezko, "Precise qubit control beyond the rotating wave approximation," *New Journal of Physics*, vol. 16, p. 093022, sep 2014.

[175] N. F. Ramsey, "A Molecular Beam Resonance Method with Separated Oscillating Fields," *Physical Review*, vol. 78, pp. 695–699, jun 1950.

[176] A. N. Vamivakas, C.-Y. Lu, C. Matthiesen, Y. Zhao, S. Fält, A. Badolato, and M. Atatüre, "Observation of spin-dependent quantum jumps via quantum dot resonance fluorescence," *Nature*, vol. 467, pp. 297–300, sep 2010.

[177] L. Robledo, L. Childress, H. Bernien, B. Hensen, P. F. A. Alkemade, and R. Hanson, "High-fidelity projective read-out of a solid-state spin quantum register," *Nature*, vol. 477, no. 7366, pp. 574–578, 2011.

[178] J. M. Elzerman, R. Hanson, L. H. Willems van Beveren, B. Witkamp, L. M. K. Vandersypen, and L. P. Kouwenhoven, "Single-shot read-out of an individual electron spin in a quantum dot," *Nature*, vol. 430, pp. 431–435, jul 2004.

[179] L. A. Williamson, Y.-H. Chen, and J. J. Longdell, "Magneto-Optic Modulator with Unit Quantum Efficiency," *Physical Review Letters*, vol. 113, p. 203601, nov 2014.

[180] C. Rigetti, J. M. Gambetta, S. Poletto, B. L. T. Plourde, J. M. Chow, A. D. Córcoles, J. A. Smolin, S. T. Merkel, J. R. Rozen, G. A. Keefe, M. B. Rothwell, M. B. Ketchen, and M. Steffen, "Superconducting qubit in a waveguide cavity with a coherence time approaching 0.1 ms," *Physical Review B*, vol. 86, p. 100506, sep 2012.

[181] W. F. Koehl, B. B. Buckley, F. J. Heremans, G. Calusine, and D. D. Awschalom, "Room temperature coherent control of defect spin qubits in silicon carbide," *Nature*, vol. 479, pp. 84–87, nov 2011.

[182] A. M. Tyryshkin, S. A. Lyon, A. V. Astashkin, and A. M. Raitsimring, "Electron spin relaxation times of phosphorus donors in silicon," *Physical Review B*, vol. 68, p. 193207, nov 2003.

[183] G. Balasubramanian, P. Neumann, D. Twitchen, M. Markham, R. Kolesov, N. Mizuochi, J. Isoya, J. Achard, J. Beck, J. Tissler, V. Jacques, P. R. Hemmer, F. Jelezko, and J. Wrachtrup, "Ultralong spin coherence time in isotopically engineered diamond," *Nature Materials*, vol. 8, no. 5, pp. 383–387, 2009.

[184] B. Naydenov, F. Dolde, L. T. Hall, C. Shin, H. Fedder, L. C. L. Hollenberg, F. Jelezko, and J. Wrachtrup, "Dynamical decoupling of a single-electron spin at room temperature," *Physical Review B*, vol. 83, no. 8, p. 81201, 2011.

[185] N. Bar-Gill, L. Pham, A. Jarmola, D. Budker, and R. Walsworth, "Solid-state electronic spin coherence time approaching one second," *Nature Communications*, vol. 4, p. 1743, apr 2013.

[186] B. L. Green, S. Mottishaw, B. G. Breeze, A. M. Edmonds, U. F. S. D'Haenens-Johansson, M. W. Doherty, S. D. Williams, D. J. Twitchen, and M. E. Newton, "The neutral silicon-vacancy center in diamond: spin polarization and lifetimes," *Arxiv:1705.10205*, may 2017.

[187] A. M. Edmonds, M. E. Newton, P. M. Martineau, D. J. Twitchen, and S. D. Williams, "Electron paramagnetic resonance studies of silicon-related defects in diamond," *Physical Review B*, vol. 77, no. 24, p. 245205, 2008.

[188] M. A. Bernstein, K. F. King, and X. J. Zhou, *Handbook of MRI pulse sequences*. Academic Press, 2004.

[189] L. Viola, E. Knill, and S. Lloyd, "Dynamical Decoupling of Open Quantum Systems," *Physical Review Letters*, vol. 82, pp. 2417–2421, mar 1999.

[190] G. de Lange, Z. H. Wang, D. Ristè, V. V. Dobrovitski, and R. Hanson, "Universal Dynamical Decoupling of a Single Solid-State Spin from a Spin Bath," *Science*, vol. 330, no. 6000, 2010.

[191] B. Myers, A. Das, M. Dartiailh, K. Ohno, D. Awschalom, and A. Bleszynski Jayich, "Probing Surface Noise with Depth-Calibrated Spins in Diamond," *Physical Review Letters*, vol. 113, p. 027602, jul 2014.

[192] Y. Romach, C. Müller, T. Unden, L. Rogers, T. Isoda, K. Itoh, M. Markham, A. Stacey, J. Meijer, S. Pezzagna, B. Naydenov, L. McGuinness, N. Bar-Gill, and F. Jelezko, "Spectroscopy of Surface-Induced Noise Using Shallow Spins in Diamond," *Physical Review Letters*, vol. 114, p. 017601, jan 2015.

[193] M. Kim, H. Mamin, M. Sherwood, K. Ohno, D. Awschalom, and D. Rugar, "Decoherence of Near-Surface Nitrogen-Vacancy Centers Due to Electric Field Noise," *Physical Review Letters*, vol. 115, p. 087602, aug 2015.

[194] A. E. Hughes and W. A. Runciman, "Uniaxial stress splitting of doubly degenerate states of tetragonal and trigonal centres in cubic crystals," *Proceedings of the Physical Society*, vol. 90, pp. 827–838, mar 1967.

[195] J. Tisler, G. Balasubramanian, B. Naydenov, R. Kolesov, B. Grotz, R. Reuter, J.-P. Boudou, P. A. Curmi, M. Sennour, A. Thorel, M. BoÌˆrsch, K. Aulenbacher, R. Erdmann, P. R. Hemmer, F. Jelezko, and J. Wrachtrup, "Fluorescence and Spin Properties of Defects in Single Digit Nanodiamonds," *ACS Nano*, vol. 3, pp. 1959–1965, jul 2009.

[196] A. Laraoui, J. S. Hodges, and C. A. Meriles, "Nitrogen-Vacancy-Assisted Magnetometry of Paramagnetic Centers in an Individual Diamond Nanocrystal," *Nano Letters*, vol. 12, pp. 3477–3482, jul 2012.

[197] C. Bradac, T. Gaebel, C. I. Pakes, J. M. Say, A. V. Zvyagin, and J. R. Rabeau, "Effect of the Nanodiamond Host on a Nitrogen-Vacancy Color-Centre Emission State," *Small*, vol. 9, p. 132ï¿½139, 2013.

[198] D. P. DiVincenzo, "Quantum Computation," *Science*, vol. 270, no. 5234, pp. 255–261, 1995.

[199] L. C. Bassett, F. J. Heremans, D. J. Christle, C. G. Yale, G. Burkard, B. B. Buckley, and D. D. Awschalom, "Ultrafast optical control of orbital and spin dynamics in a solid-state defect," *Science*, vol. 345, no. 6202, 2014.

[200] J. N. Becker, J. Görlitz, C. Arend, M. Markham, and C. Becher, "Ultrafast all-optical coherent control of single silicon vacancy colour centres in diamond," *Nature Communications*, vol. 7, p. 13512, nov 2016.

[201] P. Neumann, J. Beck, M. Steiner, F. Rempp, H. Fedder, P. R. Hemmer, J. Wrachtrup, and F. Jelezko, "Single-Shot Readout of a Single Nuclear Spin," *Science*, vol. 329, no. 5991, 2010.

[202] A. Dréau, P. Spinicelli, J. R. Maze, J.-F. Roch, and V. Jacques, "Single-Shot Readout of Multiple Nuclear Spin Qubits in Diamond under Ambient Conditions," *Physical Review Letters*, vol. 110, p. 060502, feb 2013.

[203] Y.-I. Sohn, M. J. Burek, V. Kara, R. Kearns, and M. Lončar, "Dynamic actuation of single-crystal diamond nanobeams," *Applied Physics Letters*, vol. 107, p. 243106, dec 2015.

[204] S. Meesala, Y.-I. Sohn, H. A. Atikian, S. Kim, M. J. Burek, J. T. Choy, and M. Lončar, "Enhanced Strain Coupling of Nitrogen-Vacancy Spins to Nanoscale Diamond Cantilevers," *Physical Review Applied*, vol. 5, p. 034010, mar 2016.

[205] O. Arcizet, V. Jacques, A. Siria, P. Poncharal, P. Vincent, and S. Seidelin, "A single nitrogen-vacancy defect coupled to a nanomechanical oscillator," *Nature Physics*, vol. 7, pp. 879–883, sep 2011.

[206] E. R. MacQuarrie, T. A. Gosavi, N. R. Jungwirth, S. A. Bhave, and G. D. Fuchs, "Mechanical Spin Control of Nitrogen-Vacancy Centers in Diamond," *Physical Review Letters*, vol. 111, p. 227602, nov 2013.

[207] P. Ovartchaiyapong, K. W. Lee, B. A. Myers, A. C. B. Jayich, and D. Budker, "Dynamic strain-mediated coupling of a single diamond spin to a mechanical resonator," *Nature Communications*, vol. 5, p. 147602, jul 2014.

[208] J. Teissier, A. Barfuss, P. Appel, E. Neu, and P. Maletinsky, "Strain Coupling of a Nitrogen-Vacancy Center Spin to a Diamond Mechanical Oscillator," *Physical Review Letters*, vol. 113, p. 020503, jul 2014.

[209] K. W. Lee, D. Lee, P. Ovartchaiyapong, J. Minguzzi, J. R. Maze, and A. C. Bleszynski Jayich, "Strain Coupling of a Mechanical Resonator to a Single Quantum Emitter in Diamond," *Physical Review Applied*, vol. 6, p. 034005, sep 2016.

[210] M. S. J. Barson, P. Peddibhotla, P. Ovartchaiyapong, K. Ganesan, R. L. Taylor, M. Gebert, Z. Mielens, B. Koslowski, D. A. Simpson, L. P. McGuinness, J. McCallum, S. Prawer, S. Onoda, T. Ohshima, A. C. Bleszynski Jayich, F. Jelezko, N. B. Manson, and M. W. Doherty, "Nanomechanical Sensing Using Spins in Diamond," *Nano Letters*, vol. 17, pp. 1496–1503, mar 2017.

[211] M. J. Burek, N. P. de Leon, B. J. Shields, B. J. M. Hausmann, Y. Chu, Q. Quan, A. S. Zibrov, H. Park, M. D. Lukin, and M. Lončar, "Free-Standing Mechanical and Photonic Nanostructures in Single-Crystal Diamond," *Nano Letters*, vol. 12, pp. 6084–6089, dec 2012.

[212] M. J. Burek, Y. Chu, M. S. Z. Liddy, P. Patel, J. Rochman, S. Meesala, W. Hong, Q. Quan, M. D. Lukin, and M. Lončar, "High quality-factor optical nanocavities in bulk single-crystal diamond," *Nature Communications*, vol. 5, p. 5718, dec 2014.

[213] M. Radulaski, Y.-K. Tzeng, J. L. Zhang, K. G. Lagoudakis, H. Ishiwata, C. Dory, P. C. Maurer, K. Alassaad, G. Ferro, Z.-X. Shen, N. Melosh, S. Chu, and J. Vučković, "Diamond Color Center Integration with Silicon Carbide Photonics Platform," *Arxiv:1610.03183*, oct 2016.

[214] J. L. Zhang, H. Ishiwata, T. M. Babinec, M. Radulaski, K. Müller, K. G. Lagoudakis, C. Dory, J. Dahl, R. Edgington, V. Soulière, G. Ferro, A. A. Fokin, P. R. Schreiner, Z.-X. Shen, N. A. Melosh, and J. Vučković, "Hybrid Group IV Nanophotonic Structures Incorporating Diamond Silicon-Vacancy Color Centers," *Nano Letters*, vol. 16, pp. 212–217, jan 2016.

[215] D. Englund, A. Faraon, I. Fushman, N. Stoltz, P. Petroff, and J. Vučković, "Controlling cavity reflectivity with a single quantum dot," *Nature*, vol. 450, pp. 857–861, dec 2007.

[216] B. Dayan, A. S. Parkins, T. Aoki, E. P. Ostby, K. J. Vahala, and H. J. Kimble, "A Photon Turnstile Dynamically Regulated by One Atom," *Science*, vol. 319, no. 5866, 2008.

[217] A. Faraon, I. Fushman, D. Englund, N. Stoltz, P. Petroff, and J. Vučković, "Coherent generation of non-classical light on a chip via photon-induced tunnelling and blockade," *Nature Physics*, vol. 4, pp. 859–863, nov 2008.

[218] M. Greiner, O. Mandel, T. Esslinger, T. W. Hänsch, and I. Bloch, "Quantum phase transition from a superfluid to a Mott insulator in a gas of ultracold atoms," *Nature*, vol. 415, pp. 39–44, jan 2002.

[219] W. S. Bakr, A. Peng, M. E. Tai, R. Ma, J. Simon, J. I. Gillen, S. Fölling, L. Pollet, and M. Greiner, "Probing the Superfluidâ€"toâ€"Mott Insulator Transition at the Single-Atom Level," *Science*, vol. 329, no. 5991, 2010.

[220] D. G. Angelakis, M. F. Santos, and S. Bose, "Photon-blockade-induced Mott transitions and X Y spin models in coupled cavity arrays," *Physical Review A*, vol. 76, p. 031805, sep 2007.

[221] M. J. Hartmann, F. G. S. L. Brandão, and M. B. Plenio, "Quantum many-body phenomena in coupled cavity arrays," *Laser & Photon. Rev*, vol. 2, no. 6, pp. 527–556, 2008.

[222] R. O. Umucalılar and I. Carusotto, "Fractional Quantum Hall States of Photons in an Array of Dissipative Coupled Cavities," *Physical Review Letters*, vol. 108, p. 206809, may 2012.

[223] M. K. Bhaskar, D. D. Sukachev, A. Sipahigil, R. E. Evans, M. J. Burek, C. T. Nguyen, L. J. Rogers, P. Siyushev, M. H. Metsch, H. Park, F. Jelezko, M. Lončar, and M. D. Lukin, "Quantum Nonlinear Optics with a Germanium-Vacancy Color Center in a Nanoscale Diamond Waveguide," *Arxiv:1612.03036*, dec 2016.